

# **Brane Craft**

**(A 2016-2017 NIAC Phase I Project)**

**Final Report  
Submitted to NASA on February 1, 2017**

***Siegfried W. Janson, Principal Investigator***

**The Aerospace Corporation  
Space Sciences and Applications Laboratory  
El Segundo, CA**

**Tel: 310-336-7420**

**e-mail:**

**[siegfried.w.janson@aero.org](mailto:siegfried.w.janson@aero.org)**

**Period Covered: May 1, 2016 – January 31, 2017**

## Table of Contents

<b>Table of Contents</b>	<b>1</b>
<b>1. Executive Summary</b>	<b>2</b>
<b>2. The Brane Craft Concept</b>	<b>3</b>
2.1 Starting Questions	4
<b>3. Mission Analysis</b>	<b>5</b>
3.1 The Orbital Debris Population	5
3.2 Starting Altitude and Inclination	11
3.3 Disposal Altitude	12
3.4 Maximum Debris Mass	15
3.5 Time to Reach Target and Dispose of Debris	18
3.6 The Radiation Environment	30
3.7 The Micrometeoroid and Particulate Debris Environment	39
<b>4. Improved Brane Craft Design</b>	<b>41</b>
4.1 Structure	41
4.2 Solar Array Design	48
4.3 Thin Film Electronics	51
4.4 Thruster System	58
4.5 Sensors	59
4.6 Actuators	62
4.7 Thermal Control	63
<b>5. Technology Roadmap</b>	<b>65</b>
<b>References</b>	<b>65</b>

## 1. Executive Summary

A Brane Craft is a membrane spacecraft with solar cells, command and control electronics, communications systems, antennas, propulsion systems, attitude and proximity sensors, and shape control actuators as thin film structures manufactured on ~10 micron thick plastic sheets. This revolutionary spacecraft design can have a thickness of tens of microns with a surface area of square meters to maximize area-to-mass ratios for exceptionally low-mass spacecraft. Communications satellites, solar power satellites, solar electric propulsion stages, and solar sails can benefit from Brane Craft design. It also enables new missions that require low-mass spacecraft with exceptionally high delta-V. Active removal of orbital debris from Earth orbit is the target application for this study.

I first studied where debris objects are located in low Earth orbit (LEO) by altitude and orbit inclination. Next, I calculated maximum debris orbit masses that could be removed from LEO orbits using an 81-gram mass, 1 meter square, Brane Craft with a delta-V capability of 16 km/s. A Brane Craft would start in an International Space Station (ISS) orbit, boost up to a debris object, wrap around the debris object, and thrust in the anti-flight direction to quickly bring the object and Brane Craft down to a 250-km altitude disposal orbit. Maximum debris object mass was 9 kg at a 500 km altitude with a 5° or less change in orbit inclination. This dropped to 0.9 kg at 2000 km altitude with a 50° change in orbit inclination. I calculated deorbit mission timelines and ran orbit simulations to verify those timelines. Two to three weeks is needed to retrieve a maximum-mass debris object anywhere in LEO, once the Right Ascension of the Ascending Nodes (RAANs) of the initial and target object orbits line up. I modeled the trapped radiation and micrometeoroid/small particle environment, and calculated radiation dose rates and number of particle penetrations per year. Worst-case radiation dose rate in LEO was 100 megarads/year at 2000-km at 0° inclination. Most debris objects are at inclinations in excess of 60° where the maximum dose rate is only 40 megarads/year. The particle flux and penetration results were surprising; the propellant storage structure in a Brane Craft could be penetrated up to 42 times over a one-month-long mission. Design changes in propellant storage are needed to prevent shorting of the electrically-conductive propellant to ground through a wall penetration.

An initial concern was that thin-film solar cells and electronics could not provide a radiation tolerance of up to 10 megarads total integrated dose (TID). Thin film Copper Indium Gallium Selenide (CIGS) solar cells and thin film carbon nanotube and ZnO transistors have the required TID radiation tolerance. The transistors are also fast enough to enable an 8 million instruction-per-second microprocessor using a 10-micron fabrication process. Concerns over small-particle penetration rates dropped the minimum feature size to 5 microns to reduce the impact probability of the 8 MIPS processor to below 10% per month. The solar cell strings are impact-tolerant.

Brane Craft rely on attitude control and control of surface curvature to thrust in any direction while maximizing solar input power. Concepts for spacecraft configurations, attitude sensors, shape sensors, and shape actuators are presented. The next steps are to fabricate simple digital electronics, solar cell strings, sensors, and actuators using radiation-tolerant designs and materials. They should be functionally tested, and subjected to increasing levels of radiation exposure up to 10 megarads. In addition, the communications system requires development of thin-film frequency sources with quartz crystal stability.

## 2. The Brane Craft Concept

A Brane Craft is a membrane spacecraft with solar cells, electronics, propulsion, sensors, antennas, actuators, etc., as thin film structures manufactured on plastic sheets. This essentially two-dimensional design can have a thickness of tens of microns with a surface area of square meters. This is a revolutionary spacecraft design that maximizes area-to-mass ratio to enable exceptionally low-mass spacecraft for aperture-driven applications such as communications satellites, solar power satellites, solar electric propulsion stages, and solar sails. It also enables new missions that require thousands of low-mass spacecraft that can significantly change trajectory or orbit. Active removal of orbital debris from Earth orbit is the target application for this study. The orbital debris population is increasing with time, and at least two debris-spacecraft collisions have occurred. Figure 1 shows an artist's concept of a 1 square meter Brane Craft about to envelop a piece of space debris in low Earth orbit (LEO).



*Figure 1. Original artist's conception of a Brane Craft in low Earth orbit about to envelop a piece of space debris. The spacecraft is a one meter square thin sheet of plastic, about one twentieth of a millimeter thick, with patches of dark blue solar cells, flat patch antennas in gold, interconnecting silver power and data lines, and red sensor patches. The sheet is starting to curl around a roughly 15-cm long piece of space debris. The Earth is in the background. Image courtesy of The Aerospace Corporation.*

The basic Brane Craft design has distributed arrays of nano-electrospray thrusters that use an ionic liquid propellant. About  $1 \text{ cm}^2$  of electrospray thruster area is required to process the 180 W of DC power for propulsion generated by thin film solar arrays deposited over most of the 1-square meter surface. Ionic liquids have essentially zero vapor pressure, and the propellant is stored in the  $\sim 10$ -micron gap between two sheets of Kapton<sup>®</sup>. Figure 2 shows a schematic cross section of the initial design at the start of this effort. This Brane Craft design could generate a total of 8.2 millinewtons of thrust at 4000 s specific impulse under full sunlight at 1 astronomical unit (A.U.) from the sun. At 45-grams mass Brane Craft could accelerate at  $0.18 \text{ m/s}^2$ ; at least 100 times faster than a conventional electrically-propelled spacecraft. The 1-square meter design held 12.8 grams

of propellant and generated a total delta-V of 15.8 km/s at 4000 s specific impulse over 18 hours of thrusting. This is more than enough delta-V to start in a 400-km altitude LEO orbit, maneuver out to a piece of space debris in Low Earth Orbit (LEO), and drag it down to a disposal orbit. If the debris mass was less than ~2 kg in LEO altitudes below 1000-km, the process could be repeated one or more times. If the debris mass were much larger, the object could be deorbited using multiple Brane Craft, sequentially.

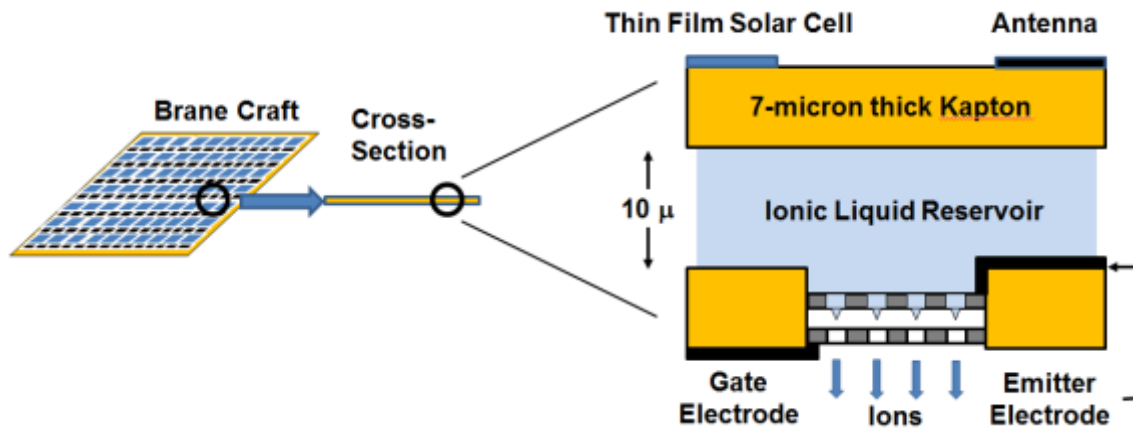


Figure 2. Schematic cross section of the original Brane Craft concept. A simplified drawing of a flat Brane Craft is shown on the left, a cross section from part of the spacecraft is illustrated in the middle, and a more detailed schematic cross section is shown on the right. The detailed cross section shows two 7-micron thick sheets of Kapton<sup>®</sup>, stacked horizontally, separated by a 10-micron high gap. This gap is filled with ionic liquid propellant, and is the propellant reservoir or tank. The top Kapton<sup>®</sup> sheet has thin film solar cells, antennas, etc, deposited on the top surface. The bottom sheet of Kapton<sup>®</sup> has a hole in it that is filled with a nano-electrospray thruster. The thruster is composed of a nano-patterned top flat plate emitter electrode with sharp emitter structures that point downward and fluid channels to allow the propellant to enter the thruster from above and cover the sharp tips. The emitter electrode is in electrical contact with the propellant reservoir. Surface tension and surface coatings keep the liquid propellant in contact with the top emitter electrode only. The bottom gate electrode is a thin metallic sheet with apertures that individually align with the sharp tips. The gate electrode is connected to the bottom surface of the bottom Kapton<sup>®</sup> sheet; this is essentially spacecraft ground. When a sufficient potential is applied between the emitter and gate electrode, the ionic liquid propellant will be ionized near the sharp tip, and the ions will be accelerated towards the gate electrode, and exit through the holes in this electrode. The net result is a stream of ions that progress downwards, thus generating an upwards thrust. More details on thruster operation will be given in a different section.

## 2.1 Starting Questions

A number of questions regarding the feasibility of the Brane Craft concept for removing space debris, and for other potential missions, were addressed during this Phase I effort. These are:

1. *Could most of the tracked debris objects in LEO with mass less than 2 kg be removed using Brane Craft? What are the time scales?*
2. *What are the radiation dose levels in LEO for electronics essentially on the outside of a spacecraft?*
3. *How often will Brane Craft in LEO be penetrated by a micrometeoroids or particulate debris objects?*
4. *Can terrestrial thin film solar cell technology be adapted for this application?*
5. *Can thin film electronics be fabricated on thin plastic sheets with sufficient computing speed to operate a spacecraft?*
6. *What thin film transistor technologies are required to provide a nominal one-month operating lifetime in the worst LEO radiation environment?*
7. *Can a Brane Craft operate through extreme thermal cycles in LEO?*
8. *Can attitude and navigation sensors be fabricated as thin film structures on plastic sheets?*
9. *Can thin-film attitude control systems be designed for this flat structure?*
10. *Can shape control be implemented as thin film structures?*

### **3. Mission Analysis**

Mission analysis is where space systems design starts. It generates mission requirements, which ultimately flow down to a concept of operations, spacecraft requirements, and spacecraft systems/subsystems requirements. In our case, we have a general requirement to actively deorbit space debris in a cost-effective manner. What does that mean in terms of required delta-V capability, maneuvering, navigation, etc.?

#### **3.1 The Orbital Debris Population**

“The simple definition of space debris is any human-made object in orbit that is not in active use.”

<sup>1</sup> The lower limit for reliable tracking of an object is 5 to 10 cm, and more than 17,000 objects are tracked by the Space Surveillance Network (SSN). Figure 3 shows the monthly number of all objects officially tracked by the SSN through February, 2016. Big spikes at the end of 2006 and the beginning of 2009 are due to the fragmentation debris from a Chinese anti-satellite test, and a collision between an Iridium satellite (number 33) and Cosmos 2251. Note that it could take a decade for the tracked fragmentation debris level to return to the pre-collision level, assuming no more inadvertent satellite collisions, explosions, or anti-satellite tests.

Monthly Number of Objects in Earth Orbit by Object Type

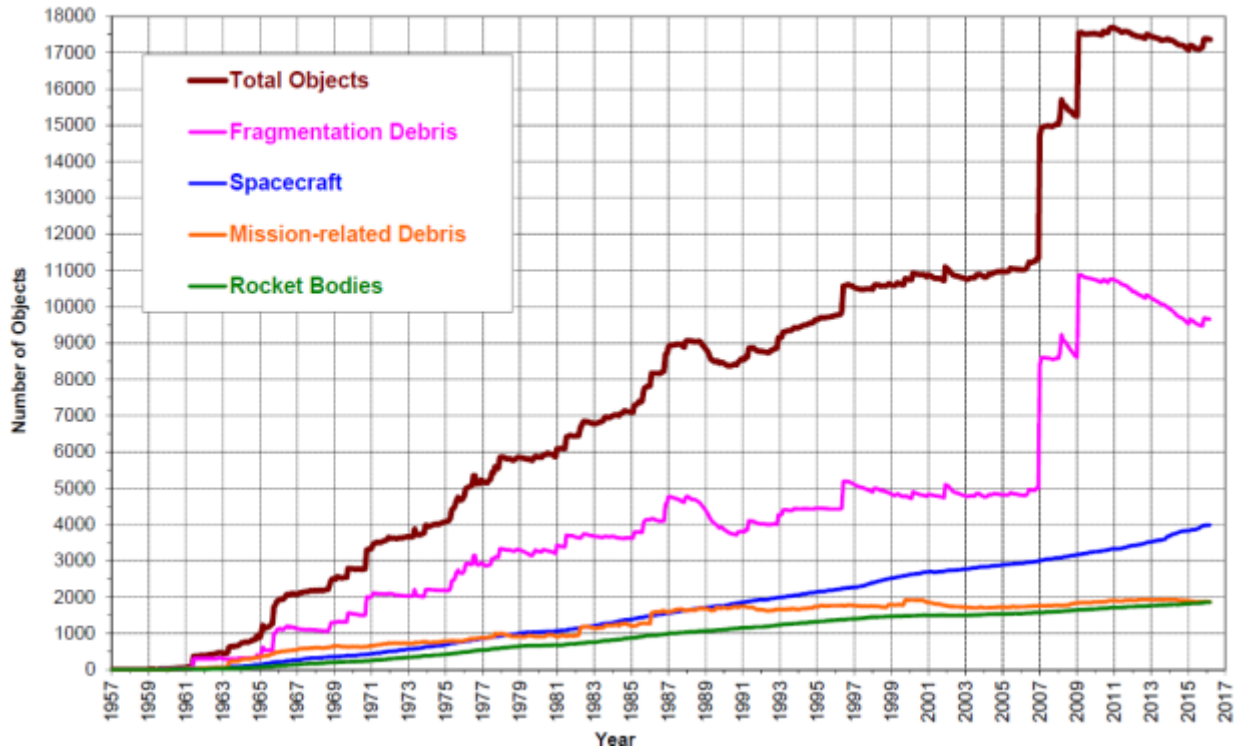


Figure 3. Monthly number of objects tracked by the U.S. Space Surveillance Network. The vertical scale is 0 on the bottom to 18,000 objects at the top, while the horizontal scale starts with the year 1957 on the left to the year 2017 on the right. The number of spacecraft was less than 100 through the year 1963, and increases fairly linearly with time through the year 2016. There were 3,000 tracked spacecraft in 2007, and 4,000 in 2016. The number of tracked rocket bodies is about half that of spacecraft, and mission-related debris were slightly higher over the same time period. The number of fragmentation debris increased fairly linearly from almost zero in 1961 to 5,000 in 1997. Fragmentation debris were fairly constant at 5,000 objects between 1997 and 2007, and then jumped to 8,500 due to a Chinese anti-satellite test. Another jump from 8,600 to 11,000 fragmentation debris objects occurred in 2009 due to a collision between an Iridium and a COSMOS 2251 satellite. The number of fragmentation debris objects has since declined to 9,700 objects due to orbital decay. The total number of tracked objects was fairly constant at about 17,500 objects from 2009 through 2016. The number of fragmentation objects was declining over this time period, but the number of spacecraft was increasing, so the total object population remained almost constant. Image, courtesy of NASA, from reference 2.

If ground tracking systems were improved to see down to 1 cm; approximately 500,000 debris objects would fill the catalog. The 2009 Cosmos-Iridium collision generated about 2000 tracked debris objects, over 8000 (estimated) debris objects of size between 3 and 10 cm, and over 150,000 debris objects (estimated) smaller than 3 cm in size.<sup>3</sup> While these may seem physically small, they are still large enough to cause catastrophic damage to an active satellite. Table 1 shows mass, kinetic energy, and equivalent TNT mass for ideal aluminum spheres colliding with an object at

10 km/s. A 1-cm diameter object has the explosive equivalent of a stick of dynamite, so ideally, we would like to remove all debris objects larger than 1 cm in size. However, we only track objects of 5-cm size and larger; about 10,000 debris objects that we can go after in the near future.

*Table 1. Mass, kinetic energy, and explosive equivalent for an ideal aluminum sphere colliding with a satellite at 10 km/s.*

Debris Diameter	Mass (grams)	Kinetic Energy	Explosive Equivalent
0.5 cm	0.177 grams	8.84 kJ	1 Cherry bomb
1 cm	1.41 grams	70.7 kJ	1 Stick of dynamite
3 cm	38.2 grams	1.91 MJ	27 Sticks of dynamite
5 cm	177 grams	8.84 MJ	125 Sticks of dynamite
10 cm	1.41 kg	70.7 MJ	1,000 Sticks of dynamite
20 cm	11.3 kg	565 MJ	8,000 Sticks of dynamite

Where are the majority of orbital debris objects? Figure 4 shows the density of tracked debris objects as a function of altitude in Earth orbit. Highest densities occur in LEO; altitudes between 300 and 2000 km. Note that the highest density is  $4 \times 10^{-8}$  objects per cubic kilometer, or one object for every 25 million cubic kilometers. That’s about 360 km between nearest neighbors, on average. The next largest density peak occurs in Medium Earth Orbit (MEO), and is primarily due to the U.S. Global Positioning Satellites (GPS) and their international cousins. A larger peak occurs at Geosynchronous Earth Orbit (GEO) where communications and high-altitude weather satellites are relatively stationary above a point on the equator. This is prime satellite real estate.

Figure 5 shows density vs. altitude in LEO altitude range using a linear vertical scale. These plots were made in 2007 after the Chinese anti-satellite test that caused the destruction of the Feng Yung 1C (FY1C) weather satellite. Several peaks occur for LEO communications and navigation satellite constellations; Iridium, Orbcomm, Globalstar, Parus, and Strela. The latter two were initiated by the former Soviet Union in the 1970’s. Satellite orbits at altitudes above 1000 km are more affected by solar radiation pressure than by atmospheric drag, and can stay in orbit for centuries. Figure 5 shows that orbital debris density (the “Non-satellites” curve) peaks in the 800 to 1000-km range, and drops off by 1800 km.

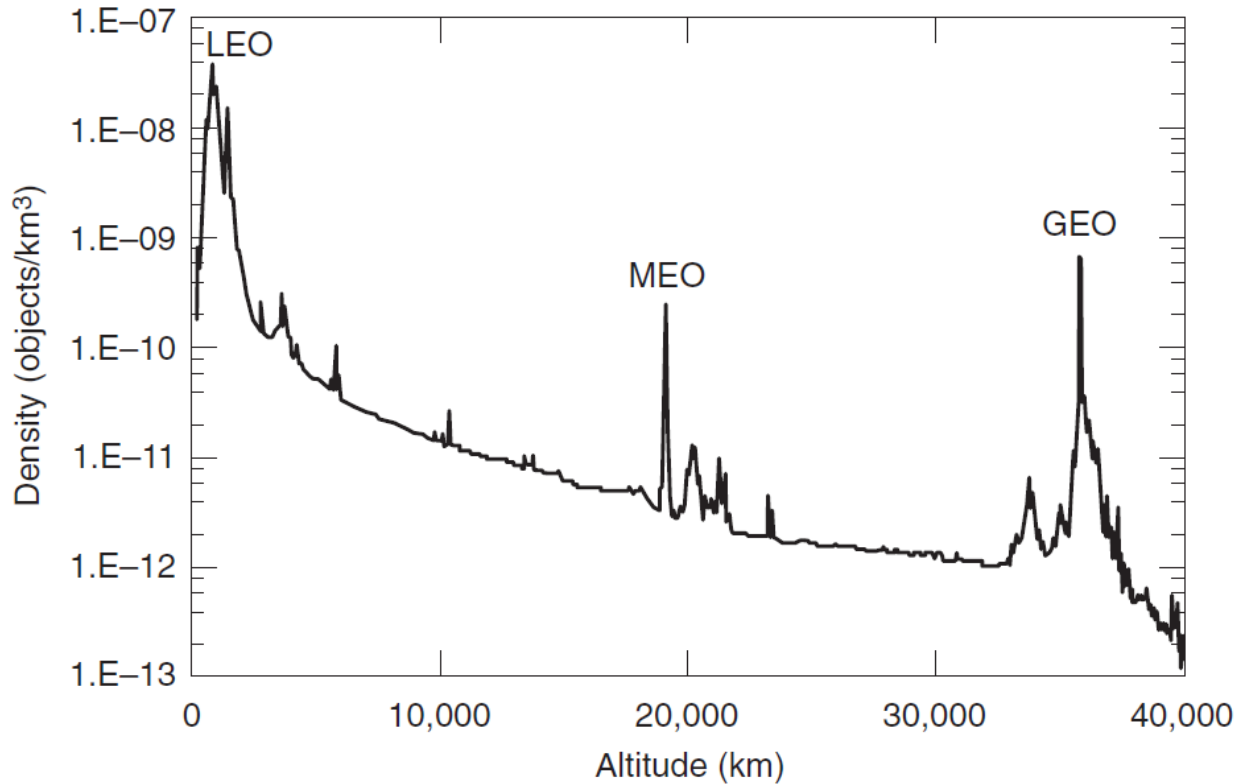


Figure 4. Altitude distribution of objects in the near-Earth region. The vertical scale is a logarithmic scale starting with an object density of  $10^{-13}$  per cubic km at the bottom, and reaching  $10^{-7}$  objects per cubic km at the top. The horizontal scale starts at 0 km altitude on the left, and goes up to 40,000 km altitude on the right. The density of tracked objects starts at about  $2 \times 10^{-10}$  objects per cubic kilometer at 300 km altitude, peaks at  $4 \times 10^{-8}$  objects per cubic kilometer at 850 km altitude, and drops rapidly to about  $10^{-10}$  at 3000 km altitude. The density of tracked objects decreases more slowly with altitude at higher altitudes, with a peak of  $2 \times 10^{-10}$  objects per cubic km at about 19,000 km altitude, and a more prominent peak of  $10^{-9}$  objects per cubic km at 35,600 km altitude. These peaks represent the U.S. GPS satellites and international navigation satellites in Medium Earth orbit, and geosynchronous communications and weather satellites, respectively. GEO satellites and their upper stages are disposed of at slightly higher altitudes, and these debris fill a roughly 2000-km wide belt above GEO with a density of  $\sim 10^{-11}$  objects per cubic km. Above that, the tracked object density decreases rapidly to  $10^{-13}$  objects per cubic km at 40,000 km altitude. Image, courtesy of The Aerospace Corporation, from reference 4.

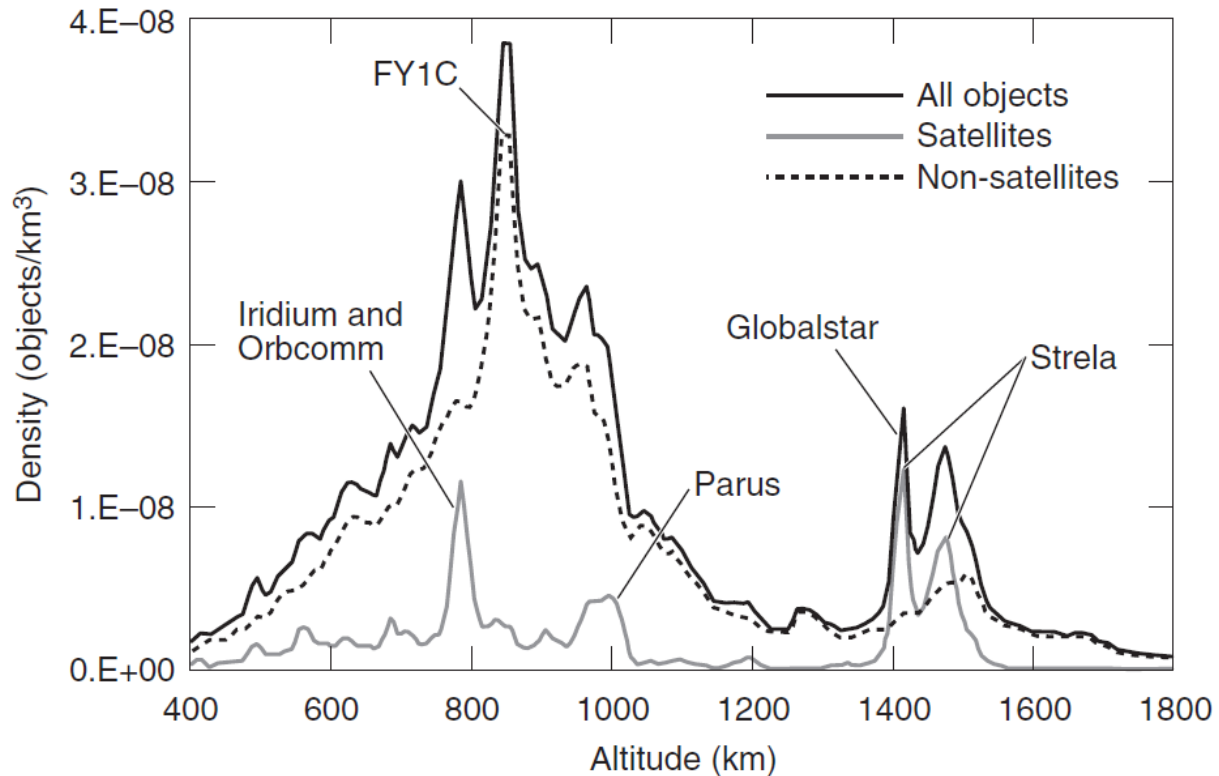


Figure 5. Altitude distribution of objects in low Earth orbit. The vertical scale is linear and ranges from 0 objects per cubic km at the bottom to  $4 \times 10^{-8}$  objects per cubic km at the top. The satellites curve is near the bottom with an average density of about  $2 \times 10^{-9}$  objects per cubic km. There is a sharp peak of  $10^{-8}$  objects per cubic km at 780-km altitude for the Iridium and Orbcomm constellations, an 80-km wide flat peak of  $4 \times 10^{-9}$  objects per cubic km at 990-km altitude for the Russian Parus constellation, a sharp peak of  $1.6 \times 10^{-8}$  objects per cubic km at 1410-km altitude for the Globalstar and Russian Strela constellations, and a broader peak of  $1.3 \times 10^{-8}$  objects per cubic km at 1480-km altitude for another Strela constellation. The non-satellites, or orbital debris, curve is significantly higher. It rises rapidly from about  $2 \times 10^{-9}$  objects per cubic km at 400 km altitude to  $3.3 \times 10^{-8}$  objects per cubic km at 850 km altitude. This peak is due to debris from the Chinese anti-satellite test that destroyed their Feng Yung 1C (FY1C) weather satellite. Debris object density drops down to about  $3 \times 10^{-9}$  objects per cubic km at 1200 km altitude, rises to  $5 \times 10^{-9}$  objects per cubic km at 1500 km altitude, and drops down to  $1 \times 10^{-9}$  objects per cubic km at 1800 km altitude. Image, courtesy of The Aerospace Corporation, from reference 4.

What is the distribution of orbit inclinations for objects in LEO? Figure 6 shows the distribution of tracked objects in LEO as a function of orbit inclination. The largest population occurs at sun-synchronous inclinations which can range from  $96.5^\circ$  to  $116^\circ$ , depending on altitude. The vast majority of objects are in inclinations greater than  $60^\circ$ .

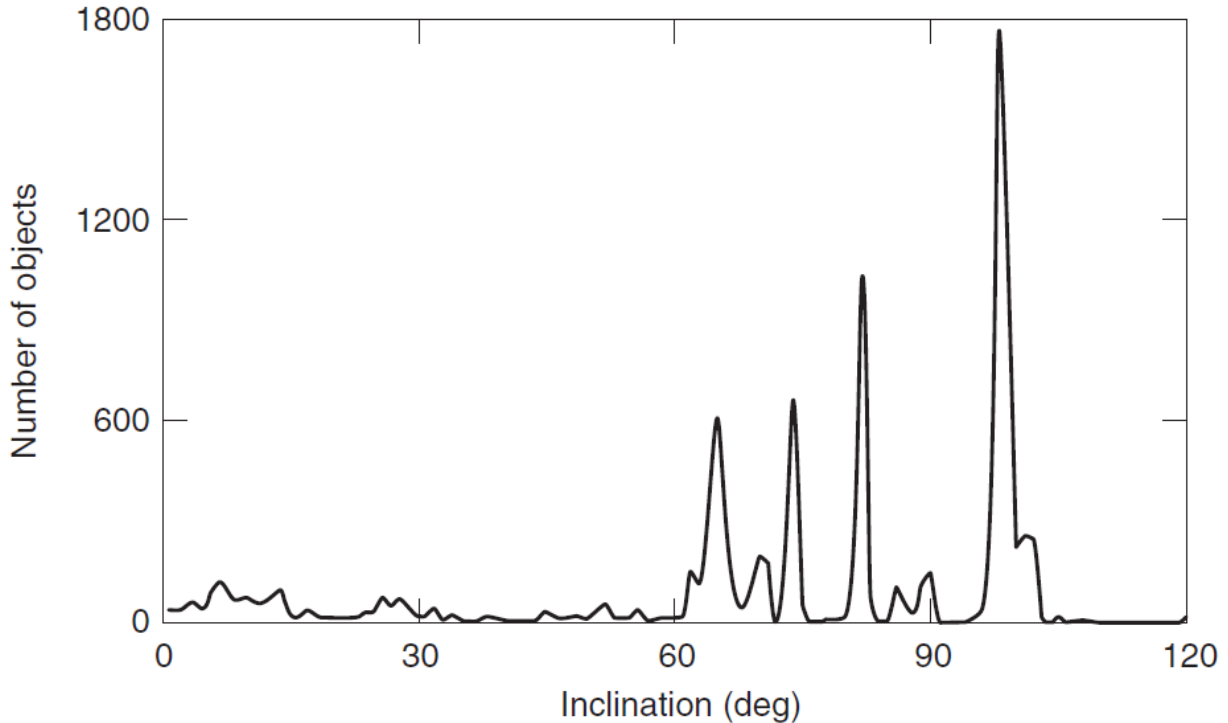


Figure 6. Inclination distribution of objects in low Earth orbit. The vertical scale is linear and ranges from 0 at the bottom to 1800 objects per degree at the top. The horizontal scale is linear and ranges from 0 degrees on the left to 120 degrees on the right. The number of objects per degree of inclination is less than 100, except for peaks at 65°, 71°, 75°, 82°, and from 96° to 105° degrees. The latter peak is for sun-synchronous orbits used by LEO Earth observation and weather spacecraft, like Feng Yung 1C, and reaches a peak value of almost 1800 objects per degree. The 65° inclination peak is at 600 objects per degree, the 71° peak is at 650 objects per degree, and the 82° peak is at 1050 objects per degree. The vast majority of objects in LEO are in inclinations greater than 60 degrees. Image, courtesy of The Aerospace Corporation, from reference 4.

### Findings for 3.1 The Orbital Debris Population:

1. There are over 9000 tracked debris objects larger than 5 cm in Earth orbit.
2. There are orders-of-magnitude more objects of smaller size, but are currently untracked.
3. Debris population peaks occur in LEO, MEO, and GEO.
4. Most debris objects in LEO are at inclinations greater than 60°, and fall into 4 main inclination bands.

### 3.2 Starting Altitude and Inclination

Brane Craft will most likely be launched as secondary payloads due to their inherently low mass. Table 2 lists U.S. non-classified launches during the year 2016, and their orbit destinations. The majority of launches (9 out of 18) were for geosynchronous satellites at an altitude of 35,786 km. The next most popular destination (4 out of 18) was the International Space Station (ISS) at ~400 km altitude with an orbit inclination of 51.6°. A Global Positioning System (GPS) satellite was launched to 20,189 km circular orbit at 55° inclination, the JASON-3 Earth observation satellite was launched to a 1,338 km altitude circular orbit at 66° inclination, a WorldView-4 Earth observation satellite was launched to a 600-km altitude, circular, 97.98° sun-synchronous inclination orbit, eight CYGNSS Earth/weather observation satellites were simultaneously launched into a 500-km circular, 35° inclination orbit, and one asteroid sample and return spacecraft, OSIRIS-Rex, was launched into an Earth escape trajectory. Based on these data, the ISS would make a good starting point for the deployment of Brane Craft, augmented by less frequent flight opportunities to sun-synchronous orbits. The nominal starting orbit is therefore 400 km circular with a 51.6° inclination.

*Table 2. Launch date, launch vehicle, orbit altitude, and orbit inclination for U.S., non-classified launches during the year 2016. Launch data from reference 5.*

Launch Date	Launch Vehicle	Orbit Altitude (km)	Orbit inclination (°)
1/17/16	Falcon 9	1,338	66.04
2/5/16	Atlas V	20,189	55.01
3/4/16	Falcon 9	35,786	0
3/23/16	Atlas V	404	51.6
4/8/16	Falcon 9	404	51.6
5/6/16	Falcon 9	35,786	0
5/27/16	Falcon 9	35,786	0
6/15/16	Falcon 9	35,786	0
6/24/16	Atlas V	35,786	
7/18/16	Falcon 9	403	51.6
8/14/16	Falcon 9	35,786	0
9/8/16	Atlas V	Earth Escape	
10/17/16	Antares 230	404	51.6
11/11/16	Atlas V	611	97.98
11/19/16	Atlas V	35,786	0
12/7/16	Atlas V	35,786	0
12/15/16	Pegasus-XL	500	35
12/18/16	Atlas V	35,786	0

### Findings for 3.2 Starting Altitude and Inclination:

1. There are multiple resupply flights to the ISS every year. This makes a good starting point for Brane Craft deployment: 400 km altitude, 51.6° inclination.
2. Another good starting point would be sun-synchronous orbit in LEO; many spacecraft go there at different altitudes.

### 3.3 Disposal Altitude

A Brane Craft will bring a debris object down to the disposal altitude, and if sufficient delta-V still exists, it can release the object and increase altitude to go after another object. At what altitude should an object be released? Figure 7 shows the time required to reach 200 km altitude, using aerodynamic drag only, as a function of starting altitude for a spacecraft with two different ballistic coefficients under solar maximum and solar minimum conditions. Solar maximum conditions occur roughly every 11 years when increased solar activity heats the Earth's upper atmosphere, resulting in increased atmospheric density at orbital altitudes and increased aerodynamic drag. Solar minimum conditions occur between solar maxima when the sun is quiet and atmospheric densities at orbital altitudes are below average. Ballistic coefficient is the ratio between inertial and drag forces. The higher coefficient, 50 kg/m<sup>2</sup>, corresponds to a 1.3 kg mass, tumbling, 1U CubeSat, while the lower coefficient, 10 kg/m<sup>2</sup>, corresponds to a 0.065 kg mass, tumbling, 5-cm cube. These ballistic coefficients bracket the expected range of ballistic coefficient for 5 to 10 cm size objects. Larger objects of equivalent density and shape will have higher ballistic coefficients due to mass/area ratio scaling, while smaller objects will have lower values. Note that the Brane Craft, wrapped about the debris object, will have an even lower ballistic coefficient. Orbit lifetime calculations in Fig. 7 were done using numerical integration of drag force over time, with atmospheric density determined by altitude under solar maximum and solar minimum conditions. Under worst-case conditions, solar minimum with a ballistic coefficient of 50 kg/m<sup>2</sup>, a disposal altitude of 250 km will ensure a 10-day or less orbital lifetime. Under best-case conditions, solar maximum with a ballistic coefficient of only 10 kg/m<sup>2</sup>, the disposal altitude increases to 380 km for a 10-day or less remaining orbital lifetime. The entire disposal altitude range is below the ISS and almost all operational spacecraft.

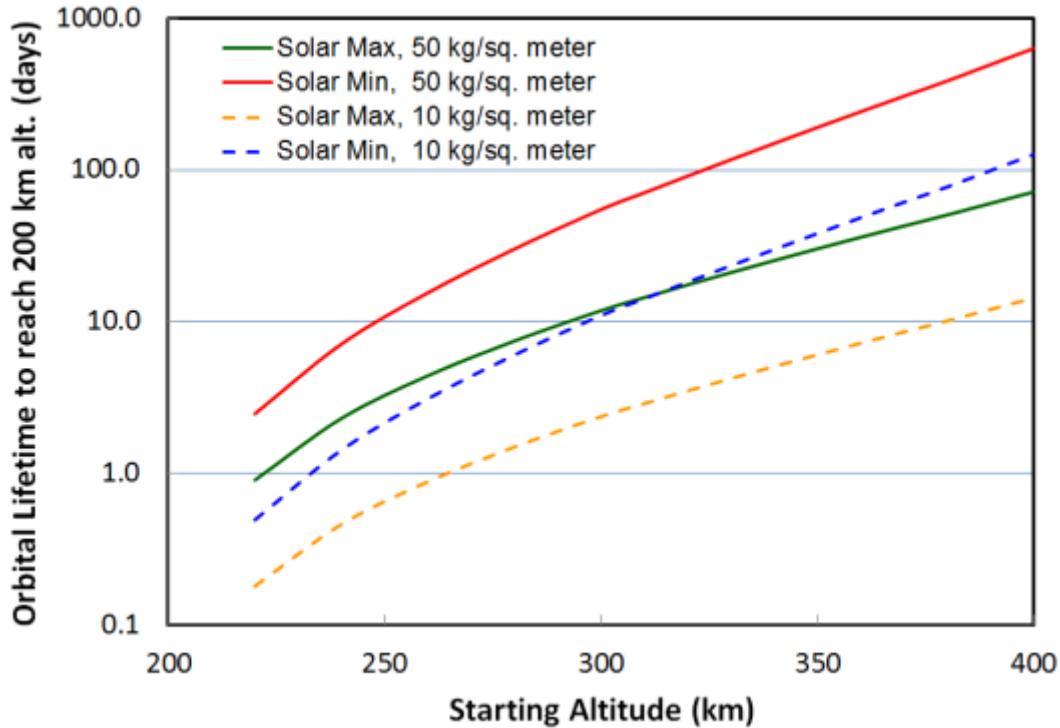


Figure 7. Time to reach 200-km altitude due to atmospheric drag as a function of starting altitude under solar maximum and solar minimum conditions for ballistic coefficients of 10 and 50 kg/m<sup>2</sup>. Orbital lifetime at 200-km is a day or less for these ballistic coefficients under solar maximum or minimum conditions. The vertical scale is logarithmic with 0.1 day at the bottom and 1000 days at the top. The horizontal scale is linear starting with 200 km at the left and reaching 400 km on the right. Under solar maximum conditions with a 50 kg/m<sup>2</sup> ballistic coefficient, the orbital lifetime to reach 200-km altitude ranges from 71 days starting at 400-km altitude to 0.9 days at 220-km altitude. Under solar maximum conditions with a 10 kg/m<sup>2</sup> ballistic coefficient, the orbital lifetime to reach 200-km altitude ranges from 14 days starting at 400-km altitude to 0.2 days at 220-km altitude. Under solar minimum conditions with a 50 kg/m<sup>2</sup> ballistic coefficient, the orbital lifetime to reach 200-km altitude ranges from 632 days at 400-km to 2.5 days at 220-km. Under solar minimum conditions with a 10 kg/m<sup>2</sup> ballistic coefficient, the orbital lifetime to reach 200-km altitude ranges from 126 days at 400-km to 5 days at 220-km.

### 3.3.1 Brane Craft Thrust at Disposal Altitude

To go after another debris object, a Brane Craft needs a net positive orbit-average acceleration after letting go of the first debris object. Maximum atmospheric drag occurs for a flat Brane Craft with surface normal parallel to the flight direction. Figure 8 shows the maximum drag on a Brane Craft as a function of altitude under solar maximum and solar minimum conditions, assuming a drag coefficient of 2. These calculations were done using:

$$F = \frac{1}{2} \rho U^2 S C_d \quad (1)$$

Where  $F$  is the drag force,  $\rho$  is the atmospheric density at a particular altitude and solar condition,  $U$  is the circular orbital velocity at that altitude,  $S$  is the cross-sectional area perpendicular to the flight direction ( $1 \text{ m}^2$ ), and  $C_d$  is the drag coefficient.

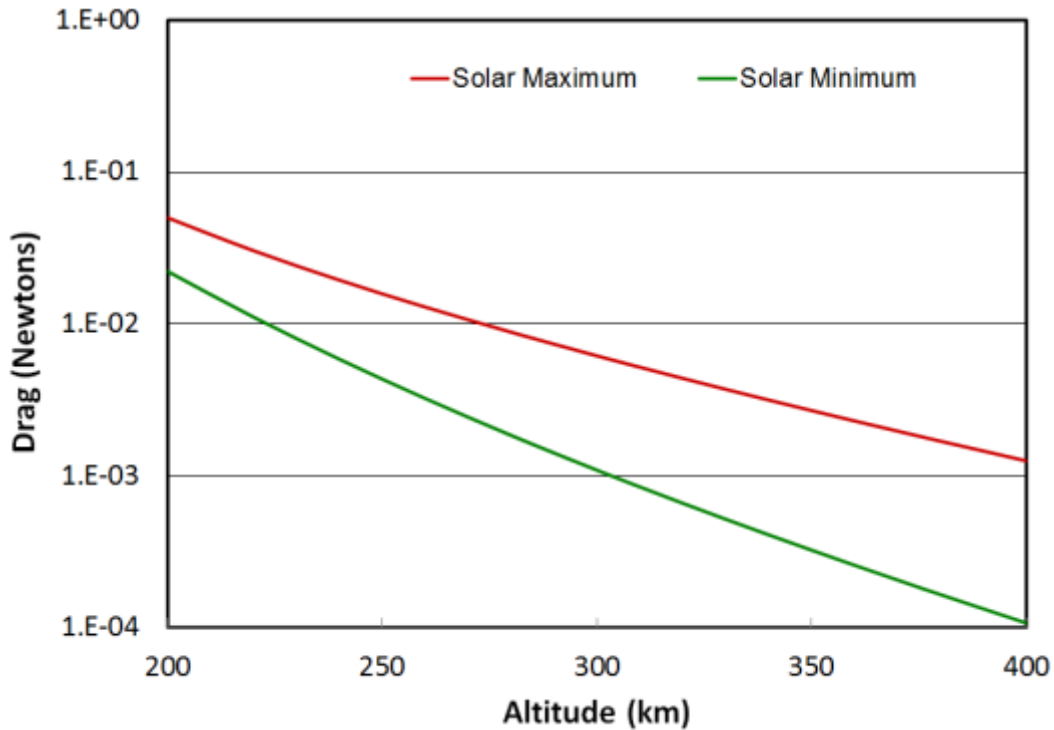


Figure 8. Maximum drag force on a 1 square meter Brane Craft as a function of altitude under solar maximum and solar minimum conditions. The vertical scale is logarithmic in drag force, and ranges from 0.1 mN at the bottom to 1 N at the top. The horizontal scale is linear in altitude, ranging from 200 km on the left to 400 km on the right. Maximum drag force under solar maximum conditions ranges from 50 mN at 200-km altitude to 1.25 mN at 400 km altitude. Maximum drag force under solar minimum conditions ranges from 22 mN at 200-km altitude to 0.1 mN at 400 km altitude.

A nominal 1-square-meter Brane Craft design can generate a maximum thrust of 8.2 mN. A maximum drag force of 2 mN will ensure positive acceleration and control authority over most orientations and Brane Craft configurations while in sunlight. Factoring in a typical 45% eclipse fraction for these altitudes drops this minimum drag level to 1.1 mN. To go after another debris object, the minimum disposal altitude for a Brane Craft is 300 km under solar minimum conditions, and 410 km under solar maximum conditions. Debris objects with ballistic coefficients of  $10 \text{ kg/m}^2$  and lower have sufficiently short post-release orbit lifetimes of 10 days or less (see Fig. 7). Debris objects with larger ballistic coefficients should not be released due their longer orbital lifetimes, and carried down as far as possible for timely burn-up.

### Findings for 3.3 Disposal Altitude:

- 1. The disposal altitude for a single-use Brane Craft can range from 250-km under solar minimum conditions to 380 km under solar maximum conditions.**
- 2. The disposal altitude for Brane Craft going after another piece of space debris can range from 300-km under solar minimum conditions to 410 km under solar maximum conditions. This should only be attempted when carrying a debris object with a ballistic coefficient of  $\sim 10 \text{ kg/m}^2$  or less.**

### 3.4 Maximum Debris Mass

The maximum debris mass that a single-use Brane Craft can capture and deorbit is a strong function of the velocity change, or delta-V, required to go from the starting orbit to the debris orbit for the outgoing leg, and the height of the debris orbit for the incoming leg. Delta-V for a particular maneuver is a function of the initial and end states, and how the maneuver is performed. Two-burn Hohmann transfers are typically the most efficient for orbit changes. They were designed for chemical rockets with moderate to high acceleration levels, hence the name “Two-burn transfer.” Typical accelerations are  $10^{-1} \text{ m/s}$  through  $10^2 \text{ m/s}^2$ . Hohmann transfers are based on instantaneous changes in spacecraft velocity; once to put a spacecraft on a new intermediate orbit that intercepts the initial orbit and the target orbit, and a second burn to put the spacecraft into the target orbit when the spacecraft crosses it. In practice, thrusting periods can be as long as a quarter orbit with little loss in efficiency; fifteen to twenty five minutes in LEO. Hohmann transfers about the Earth typically take less than 8 hours; going from LEO to GEO, for example, takes 5.3 hours; the transfer ellipse that connects a 400-km altitude orbit with a the 35,786-km altitude GEO orbit has a period of 10.6 hours, and the spacecraft is on that orbit for half an orbit period.

Low-thrust orbit transfers are typically calculated using numerical integration along the flight path, or estimated using the Edelbaum approximation. The transfer orbit is not the ellipse used in the Hohmann transfer, but a spiral. The Edelbaum approximation assumes that the spacecraft velocity as it is spiraling in or out is close to the local circular orbit velocity. It is typically used for spacecraft using electric thrusters for orbital maneuvering with acceleration levels of  $10^{-3} \text{ m/s}^2$  and less. An Edelbaum transfer from LEO to GEO can take from weeks to months.

The current Brane Craft design has a mass of 81 grams due to changes in overall layout to facilitate easier fabrication and size scalability. It has a nominal maximum acceleration of  $0.10 \text{ m/s}^2$ , enabling the use of Hohmann transfer estimates when it's not carrying a debris object. When wrapped about a debris object, the effective spacecraft mass can increase up to 100 times. In addition, the maximum solar input power and thrust are reduced. If the Brane Craft is curled in one dimension like a cylinder, the effective solar collection area becomes  $1/\pi$  of the maximum area; 64 W. Subtracting 20 W for spacecraft operating power reduces thruster power to 44 W and thrust to 2 mN. The increase in mass and reduction of maximum thrust can decrease the acceleration level down to the  $10^{-3} \text{ m/s}$  range where Edelbaum estimates would be required. Direct numerical integration of the orbit covers both cases.

Figure 9 shows the delta-V requirements to go from a starting orbit at 400 km to a higher LEO orbit with orbit inclination changes of 0°, 10°, 20°, 30° and 40°. These are based on Hohmann transfer calculations with an optimized split of inclination changes between the lower and upper burns. These calculations show that inclination changes dominate the outbound delta-V requirements in LEO. For inclination changes between 10° and 30°, it makes little difference what the target altitude is, and for inclinations in excess of 20°, the delta-V actually drops with increasing altitude. For a fresh Brane Craft starting at 400-km altitude with a 16-km/s delta-V capability, about 15.5 km/s, 14.6 km/s, 13.4 km/s, 12.2 km/s, and 11.0 km/s are available for the deorbit phase, or inbound trajectory, for a target altitude of 1000 km and target inclination changes of 0°, 10°, 20°, 30° and 40°, respectively. By comparison, the remaining delta-V capability for a fresh Brane Craft starting at ISS orbit (400-km altitude, 51.6° inclination) and going to geostationary orbit (35,786-km altitude, 0° inclination) is 11.2 km/s.

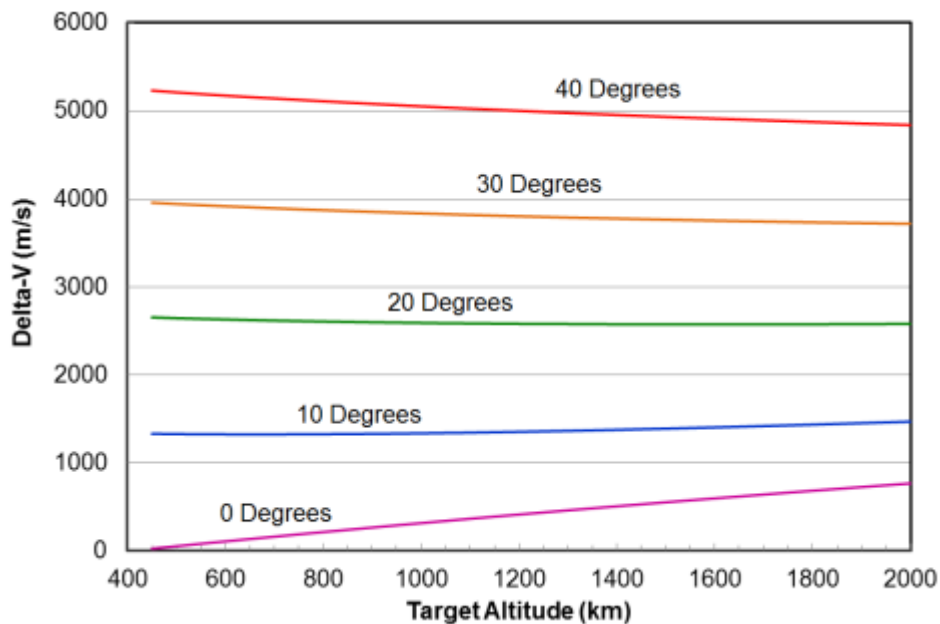


Figure 9. Delta-V required to go from a 400-km circular orbit to a higher circular orbit with inclination changes of 0°, 10°, 20°, 30°, and 40°. The vertical scale is linear, ranging from 0 m/s at the bottom to 6,000 m/s at the top. The horizontal scale is linear starting at 400-km altitude on the left, and ending with 2000-km altitude on the right. For no change in orbit inclination, the delta-V increases almost linearly from 0 at the starting altitude to 769 m/s at 2000-km altitude. For a 10° change in orbit inclination, the delta-V is essentially flat at 1330 m/s from 450 to 1000-km altitude, and then increases slowly to 1,500 m/s at 2000-km altitude. For a 20° change in orbit inclination, the delta-V slowly drops from 2,660 m/s at 450-km altitude to 2,570 m/s at 1600-km altitude, and then is essentially the same out to 2000-km altitude. For a 30° change in orbit inclination, the delta-V slowly drops from 3,960 m/s at 450-km altitude to 3,720 m/s at 2000-km altitude. For a 40° change in orbit inclination, the delta-V drops from 5,230 m/s at 450-km altitude to 4,840 m/s at 2000-km altitude.

The inbound trajectory does not require any inclination changes, but the combined mass of the Brane Craft plus debris object can be two orders-of-magnitude or more larger than the Brane Craft

alone. If the combined mass is 0.81 kg, ten times larger than the current Brane Craft mass, the effective remaining delta-V is one tenth of remaining delta-V in the Brane Craft. Figure 10 shows the calculated maximum mass that can be taken down to the worst-case 250-km altitude disposal orbit as a function of debris orbit altitude for remaining Brane Craft delta-Vs of 15, 13, and 11 km/s. Calculations were done using the Edelbaum approximation, which happens to match Hohmann transfer calculations very well for this case where there is no change in orbit inclination. The current 1-meter square Brane Craft can deorbit masses up to 6 kg at 600-km altitude, 4.8 kg at 700-km altitude, and about 2.9-kg mass at 1000-km altitude. The 700 to 1000-km altitude range covers the major population of debris objects in LEO (see Fig. 5).

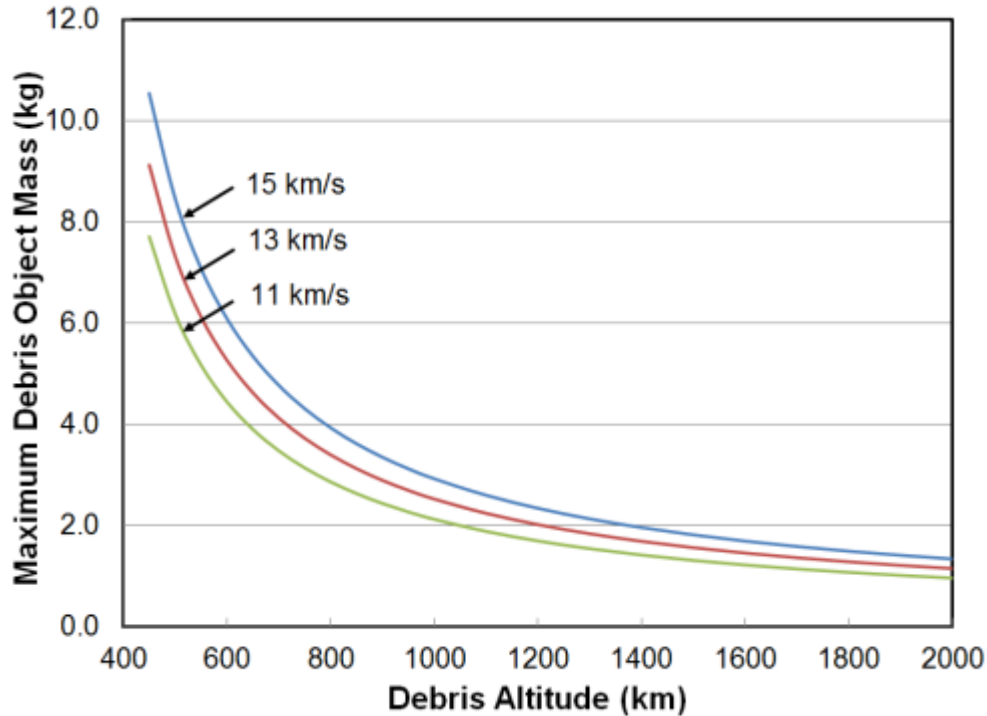


Figure 10. Maximum debris orbit mass that can be taken down to 250-km altitude as a function of initial debris altitude for remaining Brane Craft delta-V reserves of 15, 13, and 11 km/s using the current Brane Craft design. The vertical scale is linear, ranging from 0 kg at the bottom to 12 kg at the top. The horizontal scale is linear and ranges from 400 km altitude on the left to 2000 km on the right. The maximum debris object mass for a 15 km/s remaining delta-V reserve starts at 10.5 kg at 450-km altitude, drops rapidly to 4.8 kg at 700-km altitude, 3 kg mass at 980-km altitude, 2 kg mass at 1,390-km altitude, and ends at 1.3 kg at 2,000-km altitude. The maximum debris object mass for an 11 km/s remaining delta-V reserve starts at 7.7 kg at 450-km altitude, drops rapidly to 3.5 kg at 700-km altitude, 2.1 kg mass at 1000-km altitude, 1.3 kg mass at 1,500-km altitude, and ends at 1 kg at 2,000-km altitude. The curve for 13 km/s remaining delta-V reserve is between the previous two curves.

From an ISS starting orbit, all debris objects in LEO up to 1 kg in mass could be deorbited using the current Brane Craft design if the debris inclination is within 38° of the ISS inclination; 13.6° to 89.6°. All debris objects up to 2 kg in mass could be removed from altitudes up to 1000-km. Larger masses can be deorbited by increasing Brane Craft area, increasing the propellant mass

fraction and hence delta-V capability by increasing the propellant gap between the main structural sheets, or by using multiple Brane Craft in series. The latter approach requires leaving enough delta-V in each expended Brane Craft to leave the debris object and drop down to disposal altitude.

### **Findings for 3.4 Maximum Debris Mass:**

- 1. For an ISS starting orbit, the current Brane Craft design can remove objects up to 4.8 kg in mass at an altitude of 700 km, and up to 2.9 kg mass at 1000 km altitude.**
- 2. For an ISS starting orbit, the current Brane Craft design can remove objects up to 1.0 kg in mass throughout the LEO altitude range (400 to 2000 km altitude) if the target inclination is within 38° of the starting orbit inclination (13.6° to 89.6°) and 0.9 kg for orbit inclinations from 0 to 105°.**
- 3. For debris objects in sun-synchronous orbits, a starting orbit near 70° inclination is preferred.**
- 4. More massive objects can be deorbited by using Brane Craft in stages; e.g., one to take an object down 1/2 the way to disposal altitude, followed by another to take it the rest of the way. An entire 3U or 6U CubeSat could be deorbited from any LEO orbit using this technique.**

### **3.5 Time to Reach Target and Dispose of Debris**

The most time-consuming part of a deorbit mission is waiting in the starting orbit until the Right Ascension of the Ascending Node (RAAN) matches that of the target orbit. This can delay start of the outbound transfer by up a year. There is enough propellant in the current Brane Craft design to operate the thrusters at maximum power (180 W) for a total of 36 hours. During outbound thrusting without a debris object in tow, the average power collection is about 75% of maximum due to curvature of the membrane needed to supply structural strength, and the ability to thrust in directions away from the solar vector. In addition, thrusting can occur only during the sunlit parts of the orbit, typically about 60% of the orbit. Finally, thrusting occurs only during parts of the sunlit arc, and not the entire sunlit arc, in order to control growth of orbit eccentricity and efficiently change orbit inclination. All of these factors increase the outbound time from potentially a few hours to days.

When curled about a debris object, maximum power is reduced to 31% of maximum, and deorbit thrusting occurs over the entire sunlit portion of the orbit. Eccentricity growth during retrograde thrusting actually accelerates deorbit by dropping the perigee faster than the average orbit altitude. Acceleration levels are reduced due to the reduced thrust and increased mass of the debris object, but thrusting occurs over a larger fraction of the orbit. Inbound transfers can take hours to weeks.

#### **3.5.1 Matching RAAN**

Once a target debris object is identified for a particular Brane Craft, it must wait until the orbital mechanics for rendezvous are favorable. Rendezvous requires matching of the Brane Craft three-

component velocity vector and three-component position vector to the target object at a certain time; basically matching all six orbit elements at the correct time. Semi-major axis, eccentricity, and inclination are directly changed by active thrusting. RAAN is the direction of the vector from the center of the Earth to the point where the northern-heading part of the orbit crosses a projection of the Earth's equator. For a given orbit inclination, it determines the plane of an inclined orbit in inertial space, and has a range of 0° to 360°. While a spacecraft can change RAAN through direct thrusting, it can be extremely expensive. To change RAAN by 180° at 400-km altitude, for example, requires a delta-V of twice the orbital velocity:  $2 \times 7.67 \text{ km/s} = 15.4 \text{ km/s}$ . This would exhaust almost all of the Brane Craft propellant. Fortunately, orbital mechanics provides a more propellant-efficient solution.

Orbit planes rotate about the Earth's spin axis at a rate determined by orbit altitude, inclination, and orbit eccentricity. Figure 11 shows the westerly RAAN rotation rate, or nodal regression rate, in degrees per day as a function of altitude for circular orbits for multiple orbit inclinations. Orbits with inclinations between 0° and 90° rotate westward while those at inclinations greater than 90° rotate eastward. Sun-synchronous orbits rotate eastward at a rate of  $360^\circ/365.24 \text{ days} = 0.9856^\circ/\text{day}$ , irrespective of orbit altitude. Data points for the ISS and 700-km sun-synchronous orbits are shown, and the difference in nodal regression rate between these two orbits is  $6.00^\circ/\text{day}$ . A Brane Craft at the ISS would have to wait between 0 and 60 days before starting an up leg trajectory in order to properly match the RAAN of a debris orbit in a sun-synchronous orbit of any altitude. Target objects at lower orbit inclinations could require a year or more of waiting. Fortunately, ISS orbit is a fairly benign place to wait.

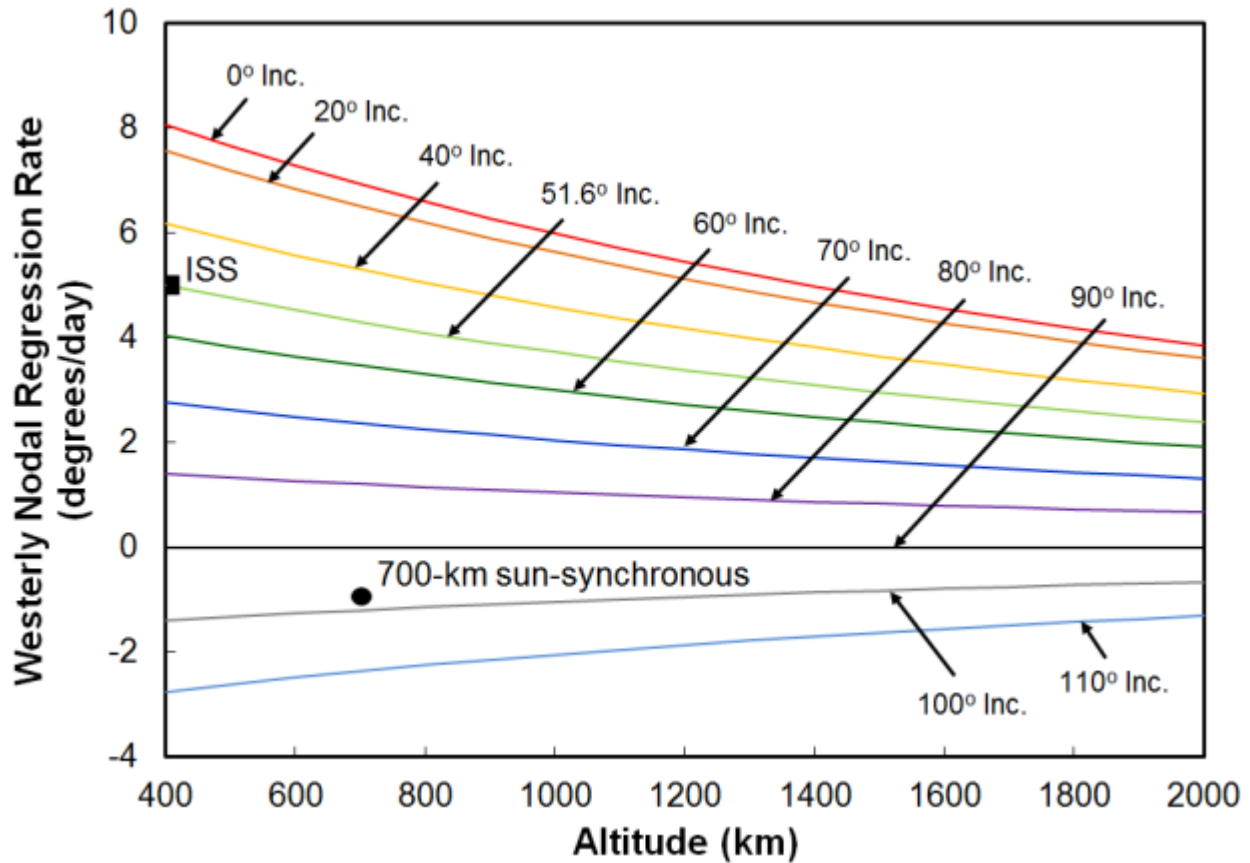


Figure 11. Westery nodal regression rate in degrees per day as a function of altitude for circular orbit inclinations of  $0^\circ$ ,  $20^\circ$ ,  $40^\circ$ ,  $51.6^\circ$ ,  $60^\circ$ ,  $70^\circ$ ,  $80^\circ$ ,  $90^\circ$ ,  $100^\circ$ , and  $110^\circ$ . The vertical scale is westery nodal regression rate in degrees per day, and it ranges linearly from  $-4$  at the bottom to  $+10$  degrees per day at the top. The horizontal scale is altitude in kilometers, and ranges linearly from  $400$  km on the left to  $2000$  km on the right. Multiple curves, starting with  $0^\circ$  inclination at the top, and ending with  $110^\circ$  inclination at the bottom span from left to right across the figure. The  $0^\circ$  inclination curve starts at  $8.05^\circ/\text{day}$  at  $400$  km, and drops down to  $3.85^\circ/\text{day}$  on the right. The curve is slightly concave upward. The  $51.6^\circ$  curve, for the ISS orbit, starts at  $5.00^\circ/\text{day}$  at  $400$ -km and ends at  $2.38^\circ/\text{day}$  at  $2000$ -km. This curve is also slightly concave upward. There is no nodal regression for  $90^\circ$  inclination orbits, so this curve is flat at  $0^\circ/\text{day}$  at all altitudes. Orbits with inclinations higher than  $90^\circ$  have easterly nodal regression rates, and have negative rates for this plot. The  $110^\circ$  inclination curve starts at  $-2.75^\circ/\text{day}$  at  $400$ -km altitude, and ends at  $-1.31^\circ/\text{day}$  at  $2000$  km. The curve is slightly concave upward.

### 3.5.2 The Outbound Trajectory

Figure 9 shows that the outbound trajectory can consume up to  $5.2$  km/s of delta-V for a  $40^\circ$  change in inclination. The Brane Craft will be in a curved, open configuration with an effective solar collection area normal to the incoming light, of  $0.75$  square meters. This provides maximum sunlight collection while still being able to point the thrusters along the flight direction (see section 4.1). Average power generation will be  $150$  W, with  $130$  W available for thrusting. Maximum thrust will be  $5.9$  mN during sunlit parts of the orbit.

The typical eclipse fraction in low Earth orbit is ~40%, but can reach 0% for a small fraction of orbits, especially at the high altitude end of LEO. Prograde thrusting, or thrusting along the velocity vector, adds energy to the orbit and normally results in a continuous increase in altitude along a spiral trajectory. Prograde thrusting while only in sunlight, however, will result in larger and larger elliptical orbits with increasing orbit eccentricity. Significant eccentricity growth will occur, and cannot be easily corrected until the orbit RAAN or argument of the perigee changes by 180°. This can take months. To minimize growth of orbit eccentricity, prograde thrusting should occur over orbit arcs that are approximately 180° apart in the orbit plane. Figure 12 shows that the best locations are near the points where the spacecraft either leaves or enters sunlight. Each thrusting period occurs over  $\alpha^\circ$  of the orbit, where  $\alpha$  is a function of orbit altitude and inclination for circular orbits. Figure 12 shows the worst-case (smallest  $\alpha$ ) geometry where the orbit plane is edge-on to sunlight, and Figure 13 shows the orbit fraction over which thrusting can occur for this worst-case condition. For a 400-km circular orbit,  $\alpha = 39.6^\circ$  and thrusting occurs over 22% of the orbit.

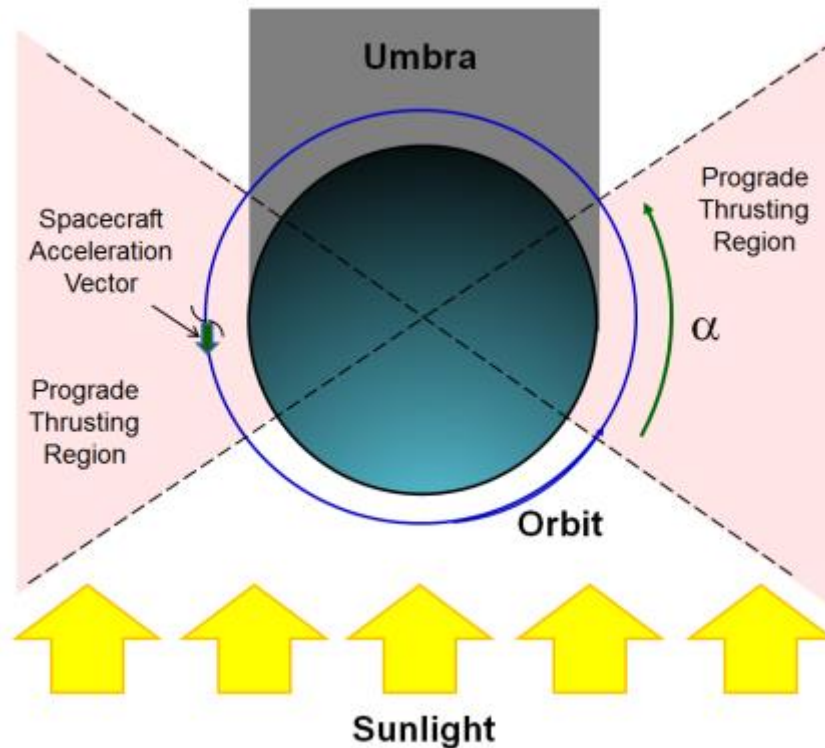


Figure 12. Schematic diagram of the eclipse geometry in LEO and optimum thrusting regions to provide balanced orbit raising using electric thrusters that only operate in sunlight. This situation, where the orbit is edge-on to sunlight, provides the shortest thrusting arcs. Sunlight starts at the bottom and flows upward. The Earth is in the middle, with a circular orbit in the plane of the page that has a radius 20% larger than the Earth's radius of 6378 km. The shadow region, or umbra, starts at the leftmost edge of the Earth, ends at the rightmost edge, and proceeds upward. There are two triangular thrusting regions defined by lines that start where the orbit crosses the umbra, one on the left and one on the right, that proceed through the center

of the Earth and continue through until they cross the orbit on the other side of the Earth. The regions look like a horizontal bow tie centered on the Earth's center. The angular width of the bow tie is labeled  $\alpha$ .

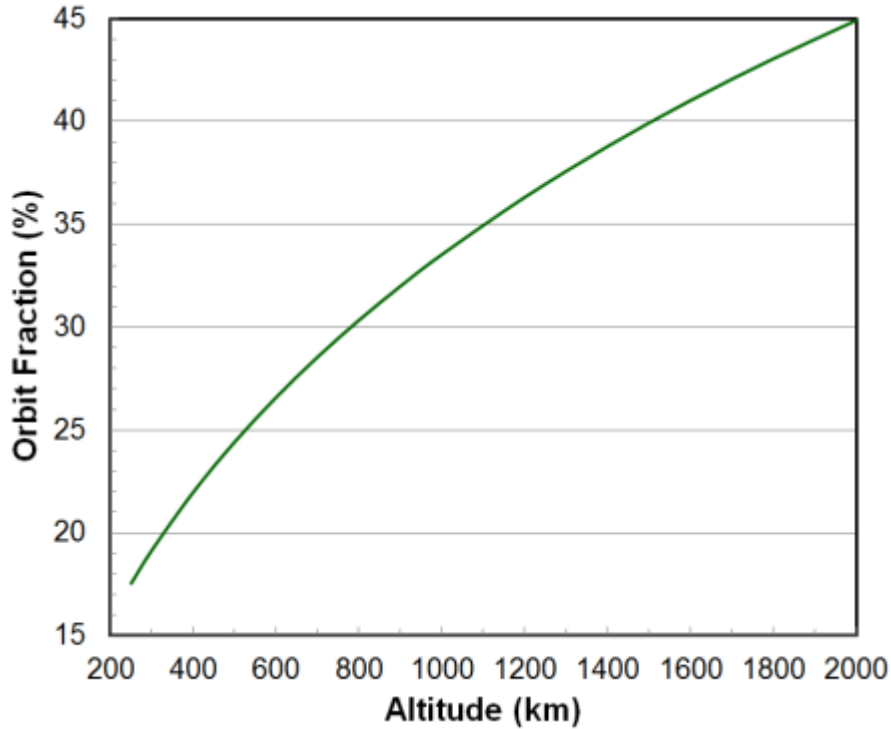


Figure 13. Orbit fraction during which prograde thrusting for symmetric orbit-raising can occur, under worst-case orbit orientation. The vertical scale is labeled orbit fraction in percent, and ranges from 15% to 45% in a linear fashion. The horizontal scale is labeled altitude in km, and ranges linearly from 200 km on the left to 2000 km on the right. Orbit fractions range from 17.5% at 250-km altitude, to 22.0% at 400-km, to 33.5% at 1000-km, and 44.9% at 2000-km.

The major propulsion challenge during the outbound transfer, as shown in Fig. 9, is to change orbit inclination. This maneuver is most efficiently done within  $\sim 30^\circ$  of where the orbit crosses the Earth's equatorial plane. Figure 14 shows a schematic drawing of the orbit geometry as viewed from the sun. The line of apsides connects these points, and one side of the line starting at the center of the Earth is the RAAN vector, and the other half is the anti-RAAN vector. The orbit and equatorial plane cross at two points separated by  $180^\circ$ , so there are two regions of favorable thrusting. The RAAN and anti-RAAN vectors are not usually parallel or anti-parallel to the sun-earth vector, so part of one is typically in shadow. This is illustrated in Fig. 14. At least one region will be in full sunlight, so a minimum orbit fraction of  $60^\circ / 360^\circ = 16.7\%$  can be used for inclination-change maneuvers. Note that inclination change thrusting is directed mostly perpendicular to the orbit plane as shown in the figure.

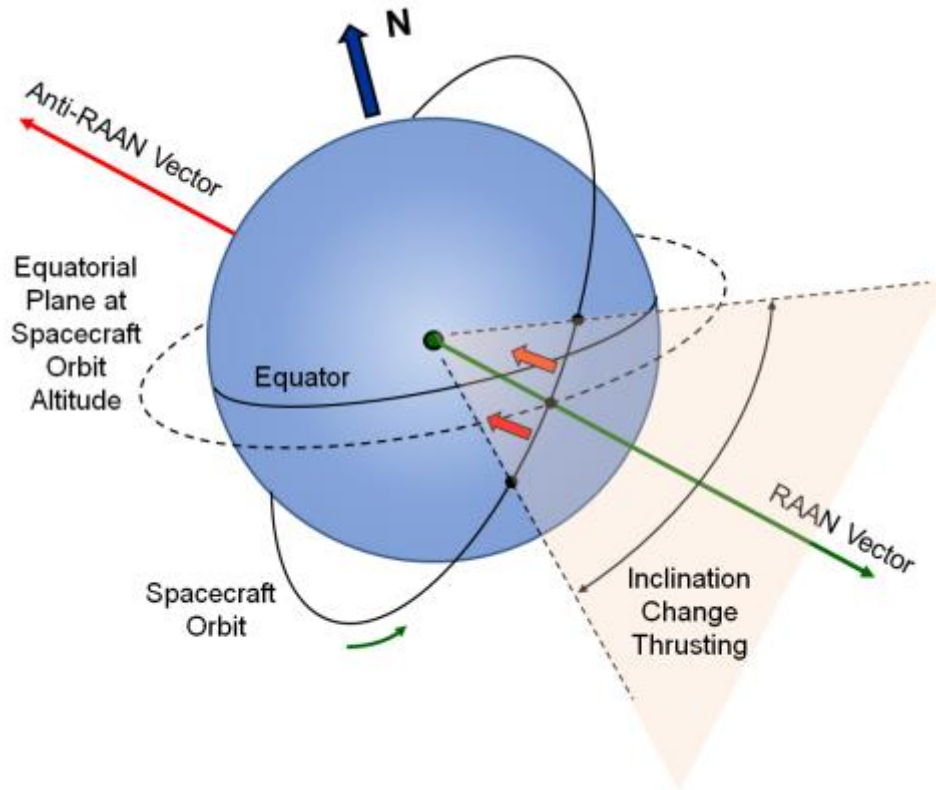


Figure 14. Orbit geometry for inclination change thrusting, as seen from the sun. Spacecraft hidden by the Earth will be in eclipse and not able to thrust. This diagram shows the Earth with the equator and spin axis, a representative inclined orbit, and the projection of the equatorial plane at orbit altitude. The RAAN vector connects the center of the Earth with the crossing point of the northern-going part of the orbit with the projection of the equatorial plane. The anti-RAAN vector starts at the center of the Earth and connects to the crossing point of the southern-going part of the orbit and the projection of the equatorial plane. That point is hidden behind the Earth in this view. Inclination change thrusting therefore occurs only about the RAAN vector for this configuration, with a half-angle of  $\sim 30^\circ$  about the RAAN vector. Red thrust vectors on this orbit arc point upwards and to the left. Acceleration in this direction will cause an increase in orbit inclination.

The longest orbit transfer times will occur for high delta-V transfers that are dominated by inclination change. In this case, the orbit average thrust is 16.7% of the 5.9 mN maximum thrust in the outbound configuration. Figure 15 shows calculated maximum orbit transfer time as a function of outbound delta-V up to 6500 m/s under these constraints. The longest outbound trajectory of 5 days at 6500 m/s is more than adequate to go from the ISS to any sun-synchronous orbit up to 2000 km in altitude.

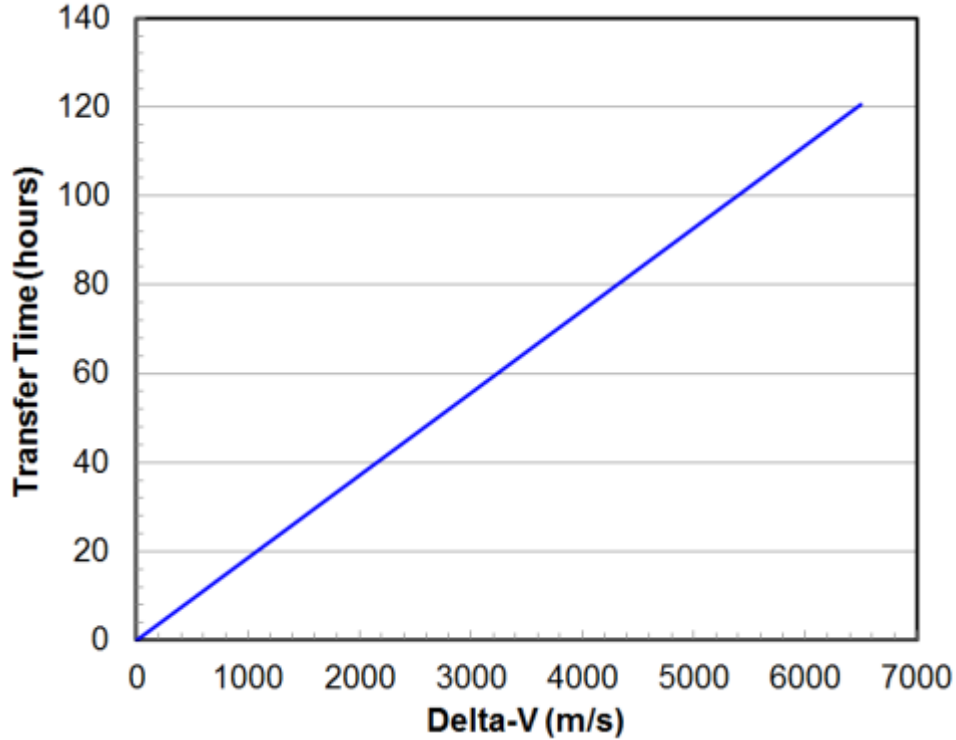


Figure 15. Maximum transfer time to reach debris object orbit as a function of outbound transfer delta-V. The transfer time is proportional to delta-V. For a 6,500 m/s delta-V, the maximum transfer time for the outbound leg is 120.6 hours. The proportionality constant is 18.55 hours per 1000 m/s delta-V.

### 3.5.3 Matching Orbit Phase

The other orbit matching maneuver that can require time is rephasing, or matching the true anomaly of a target object after entering the target orbit. The true anomaly of an individual satellite in circular orbit can be changed by temporarily moving to a different altitude, remaining at that altitude until the appropriate phase change has accumulated due to the different orbital period, followed by a return to the original altitude. The orbital period  $\tau$  is given by:

$$\tau = 2\pi (a^3/\mu)^{1/2} \quad (2)$$

where  $a$  is the semi-major axis and  $\mu$  is the gravitational constant  $G$  times the mass of the Earth  $M_E$  which is numerically equal to  $398600.44 \text{ km}^2/\text{s}^2$ . The phase (true anomaly) change  $\Delta v_d$  that occurs while occupying a different altitude drift orbit is given by:

$$\Delta v_d = 2\pi t_d (\tau_o - \tau_l) / \tau_o \tau_l \quad (3)$$

where  $t_d$  is the time at new altitude,  $\tau_o$  is the original orbit period and  $\tau_l$  is the orbit period at the new altitude. Increasing altitude results in an *increased* orbit period and a *decreased* rate of change in true anomaly, compared to the target orbit.

Additional changes in true anomaly occur while changing orbit; once while going to the drift orbit and once again while returning to the original orbit. Electric thrusters usually provide accelerations of  $10^{-3}$  m/s<sup>2</sup> or less, so changes in orbit altitude are accomplished using low-thrust spiral trajectories. Reference 6 gives derivations for phase changes and the velocity increment for low-thrust spiral transfers.

Maneuver velocity increment as a function of maneuver time was calculated using the approach outlined above and detailed in Reference 7. Figure 16 shows velocity increment as a function of maneuver time for a 180° phase change in a circular orbit at 600, 1000, and 2000-km altitude. This is the largest possible phase change. A Brane Craft can perform this maneuver in a day, but the delta-V is significant at about 500 m/s. Practical rephasing times are 3 to 8 days.

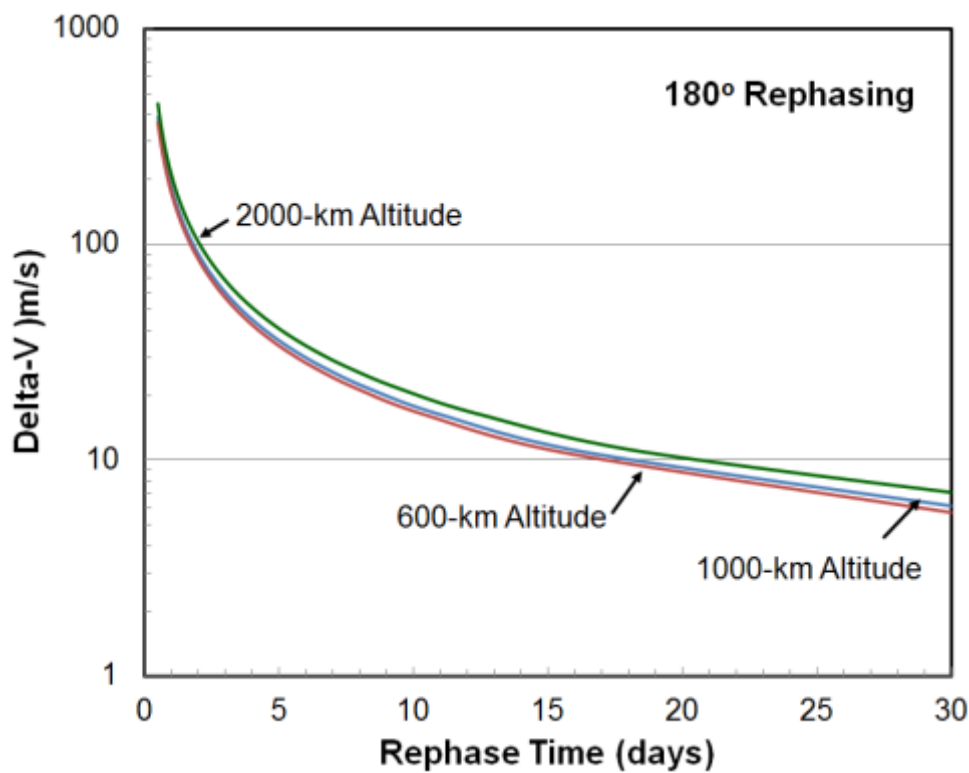
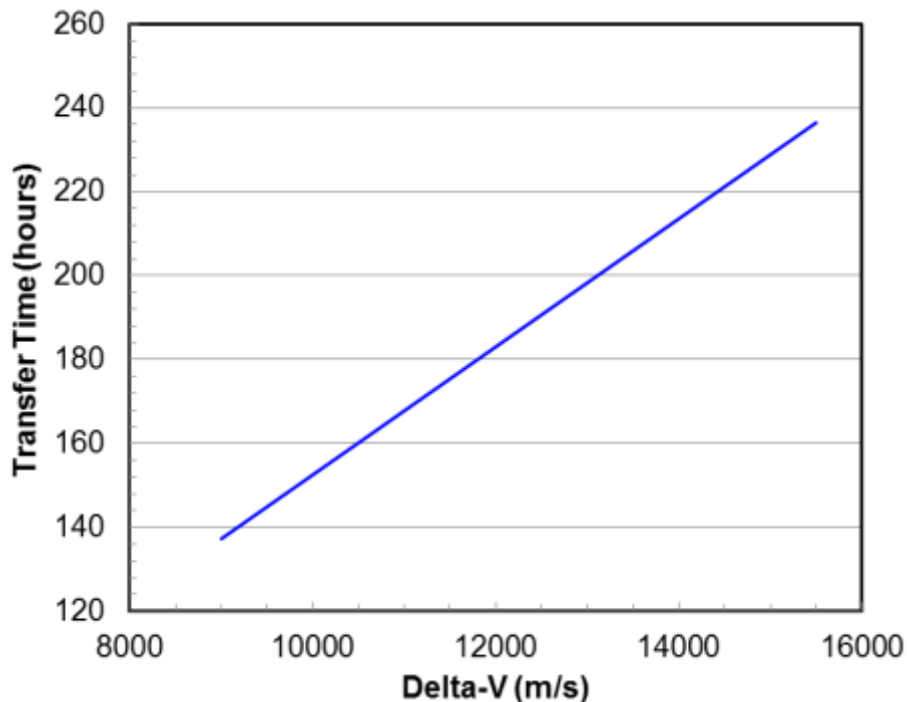


Figure 16. Delta-V required to change true anomaly by 180° as a function of time for 600 km, 1000 km, and 2000 km circular orbits. The vertical scale is logarithmic, ranging from 1 m/s at the bottom to 1000 m/s at the top. The horizontal axis is linear, ranging from 0 days on the left to 30 days on the right. All three curves are close together; the delta-V difference between the 600-km altitude and 2000 km-altitude delta-V is at most 15%, with the higher altitude having the higher value. At 1000-km altitude, the delta-V drops sharply from 200 m/s at 0.92 days to 100 m/s at 1.8 days, to 50 m/s at 3.6 days, and to 25 m/s at 7.2 days. This continues to 10 m/s at 17.9 days and out to 5 m/s at 36 days.

### The Inbound Trajectory

The inbound trajectory is the final or disposal trajectory. The Brane Craft has cylindrically wrapped itself about the target object, and thrusts in the anti-flight direction while in sunlight. No

changes in orbit inclination or RAAN are required. Since the combined mass of Brane Craft plus target object is larger than Brane Craft, and the thrust levels are lower due to the change in geometry, the inbound trajectory can take longer than the outbound trajectory. Figure 17 shows calculated inbound orbit transfer time as a function of remaining delta-V for a Brane Craft carrying the maximum debris object mass. The longest transfer time is almost 10 days. Refer to Fig. 10 to see maximum masses for three different remaining delta-V reserves as a function of orbit altitude.



*Figure 17. Inbound transfer time to a 250-km disposal orbit for a Brane Craft carrying the maximum debris object mass as a function of remaining delta-V at the beginning of the inbound transfer. The vertical axis is transfer time in hours and varies linearly from 120 hours at the bottom to 260 hours at the top. The horizontal scale is delta-V in meters per second, and varies linearly from 8,000 m/s on the left to 16,000 m/s on the right. The data curve is a straight line starting at 137 hours for a 9,000 m/s remaining delta-V to 236 hours for a 15,500 m/s remaining delta-V.*

Figure 18 shows snapshots of an inbound orbit transfer simulation run using The Aerospace Corporation's Satellite Orbital Analysis Program (SOAP). This simulation started at a 900-km altitude, 99.0° inclination, circular, sun-synchronous orbit and fired thrusters at a 2.0 mN thrust level, anti-parallel to the flight direction, while the spacecraft was in sunlight. Initial mass at 900-km altitude was 2.27 kg; 70-grams for the Brane Craft after reaching the debris orbit, plus 2.2 kg of debris object mass. The Brane Craft consumed 6 km/s of delta-V getting there from the ISS orbit, leaving 10 km/s for the inbound leg. Atmospheric drag was included, with an average cross section of 0.1 m<sup>2</sup>; minimum area for a curled up Brane Craft carrying a debris object is 0.07 m<sup>2</sup>. Figure 18 shows the buildup of orbit eccentricity due to thrusting while only in sunlight, and Figure

19 shows the apogee and perigee over time. Re-entry occurred 143.9 hours after the start of the deorbit maneuver, with less than 1% propellant remaining. The estimate from Fig. 17, which did not include eccentricity buildup, was 152.6 hours; only 6% longer. The perigee drops linearly from 900 km to 130 km, while the apogee drops at a slower rate, until the perigee reaches 200-km altitude where atmospheric drag brings down the apogee more rapidly.

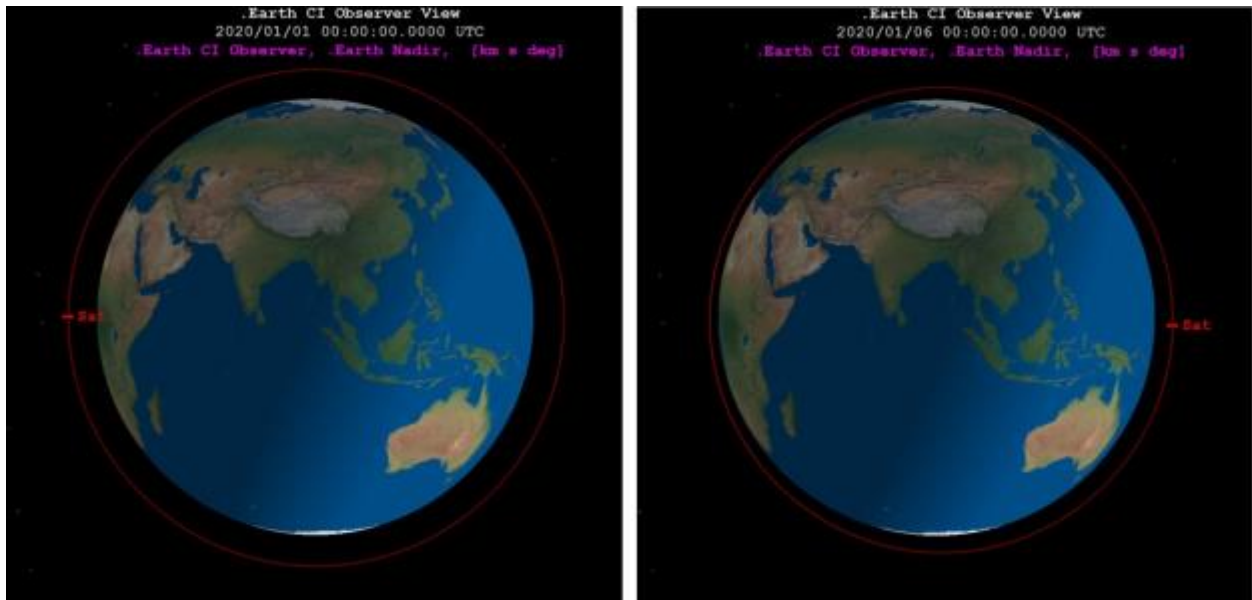


*Figure 18. Starting orbit (left) and orbit after 5 days (right) for a Brane Craft starting in a 900-km, sun-synchronous, circular orbit carrying a 2.2 kg mass debris object. The orbit normal is normal to the Earth-sun vector, and these images view the Earth from above the terminator. The starting orbit is a circle centered on the Earth with a radius that is 14% larger than the Earth's radius. After 5 days, the orbit is smaller and slightly elliptical. The closest part of the orbit (perigee) occurs on the anti-sun part of the Earth, and the farthest point (apogee) is near the Earth-sun line.*

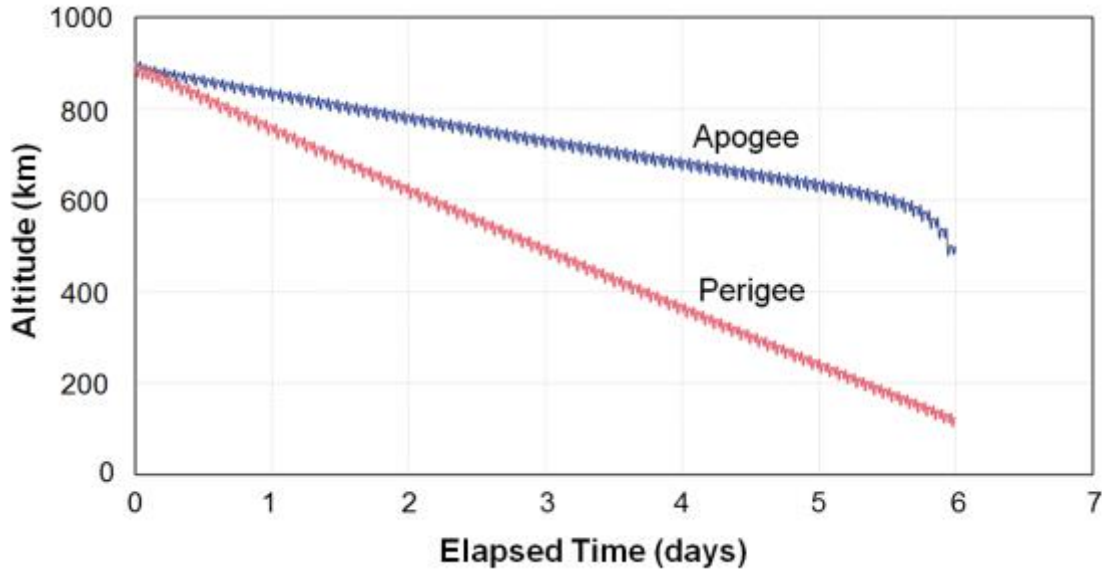


Figure 19. Apogee and perigee evolution during an inbound transfer of a 2.2-kg mass debris object in an initial 900-km, sun-synchronous, circular orbit. The perigee curve is basically a straight line going from 900 km at 0 elapsed days to 110 km at 6 days. A roughly 15-km peak-to-peak ripple with a period of about 100 minutes is on this line. The apogee line starts at 900 km altitude and is straight through 600 km altitude at 5.5 days. It curves downward after that, terminating at 430 km altitude at 6 days. A ripple is also present on this curve.

Another SOAP deorbit simulation was performed for a 2.13 kg mass Brane Craft with debris object in a 1,400-km altitude, 52° inclination, circular orbit. In this case, the delta-V required to reach this orbit from the ISS is only 550 m/s, leaving a delta-V reserve of 15,450 m/s. The maximum mass debris object is 2.13 kg for this orbit. Figure 20 shows the starting orbit and the orbit 7 days later, while Figure 21 shows the evolution of apogee and perigee over time. Re-entry occurred 212.8 hours after the start of the deorbit maneuver, with less than 1% propellant remaining. The estimate from Fig. 17 was 235.7 hours; 11% longer. The perigee drops linearly from 1400 km to 110 km, while the apogee once again drops at a slower rate, until the perigee reaches 200-km altitude where atmospheric drag brings down the apogee more rapidly.

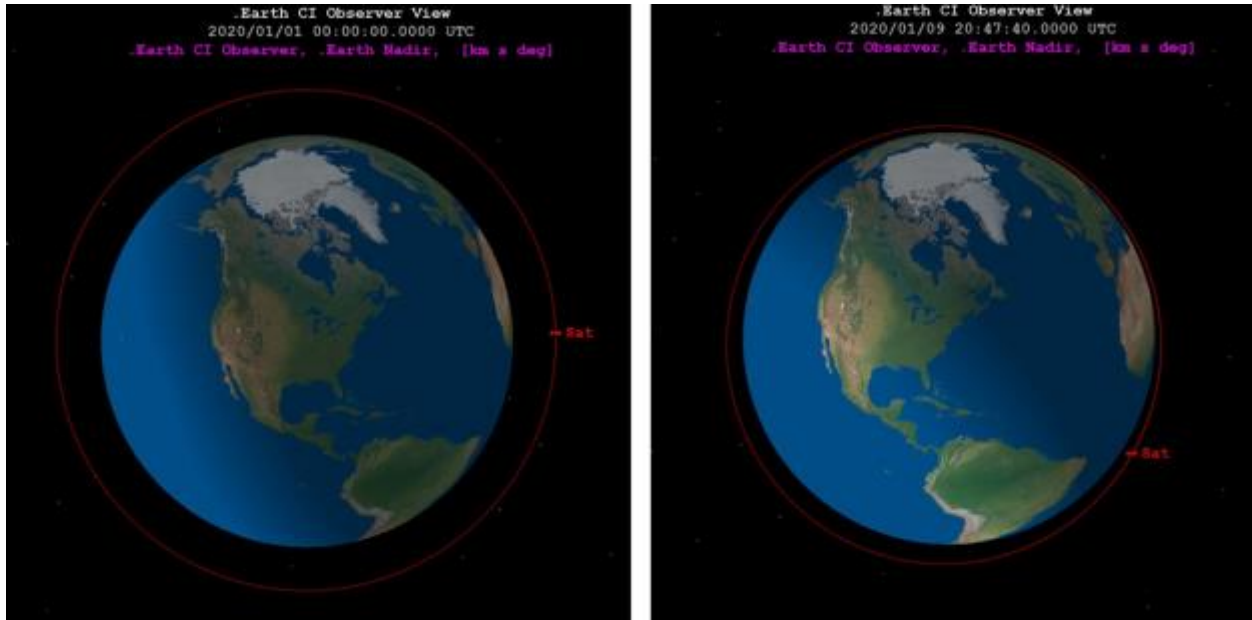


Figure 20. Starting orbit (left) and orbit after 8.8 days (right) for a Brane Craft starting in a 1,400-km, 52° inclination, circular orbit carrying a 2.13 kg mass debris object. Both views are normal to the orbit plane. The starting orbit is a circle centered on the Earth with a radius that is 22% larger than the Earth's radius. After 8.8 days, the orbit is smaller, slightly elliptical, and the closest part of the orbit (perigee) is only 150 km high..

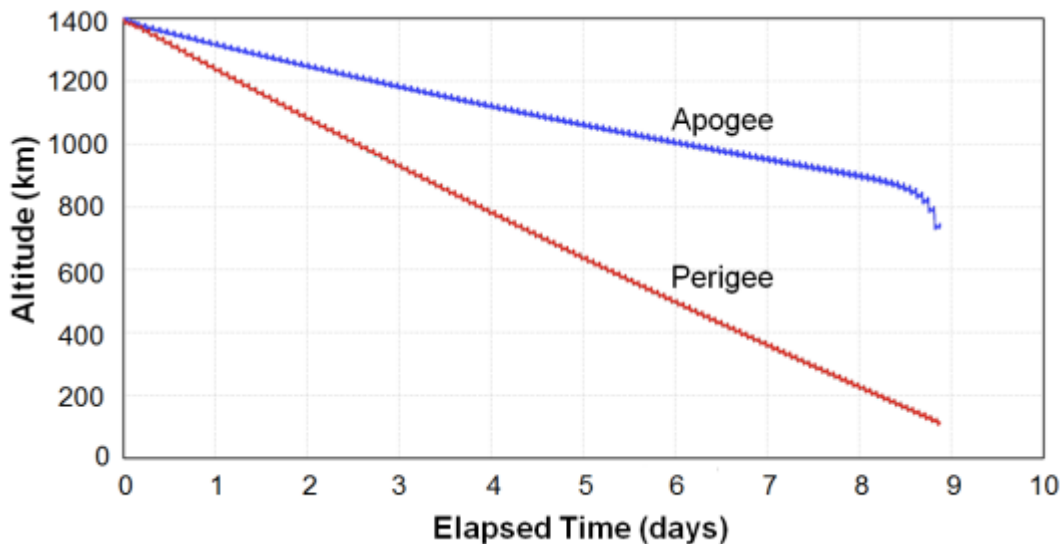


Figure 21. Apogee and perigee evolution during an inbound transfer of a 2.13-kg mass debris object in an initial 1,400-km, 52° inclination, circular orbit. The perigee curve is basically a straight line going from 1,400 km at 0 elapsed days to 110 km at 8.8 days. A roughly 15-km peak-to-peak ripple with a period of about 100 minutes is on this line. The apogee line starts at

*1,400 km altitude and is straight through 900 km altitude at 8.2 days. It curves downward after that, terminating at 720 km altitude at 8.87 days. A ripple is also present on this curve.*

### **Findings for 3.5 Time to Reach Target and Dispose of Debris:**

- 1. Waiting in the starting orbit for the starting and debris object orbital planes to line up using nodal regression can take up to year when orbit inclinations are similar.**
- 2. The ISS orbit makes a good starting orbit due to its low altitude and significant difference in nodal rotation rate compared to higher-altitude, higher inclination orbits where most tracked objects orbit.**
- 3. Time to go from an ISS orbit to anywhere in LEO is 5 days or less.**
- 4. Time to rendezvous with a tracked object can take 4 or 5 days while using minimal propellant.**
- 5. Time to go from the debris object orbit down to a disposal orbit can take up to 9 days if dragging down the maximum possible mass. Deorbit times will be faster for lower mass debris objects.**

### **3.6 The Radiation Environment**

The LEO environment, and outer space in general, is filled with energetic subatomic particles that can degrade and disrupt the proper operation of electronics and living organisms. The major particle populations are electrons and protons trapped by the Earth's magnetic field, and Galactic Cosmic Rays (GCRs) consisting of relativistic protons and heavier atomic nuclei. These high-energy particles deposit energy in the host material, leading to ionization and dislocation of host nuclei. Energy deposition is expressed in rads, where a rad is the ionizing particle dose that deposits 100 ergs of energy per gram of target matter, typically silicon. The SI unit is the gray, where 1 gray = 100 rads.

Electronics are degraded by particle radiation, and this damage accumulates over time. The time integral of the energy deposition is called the Total Ionizing Dose (TID), and the maximum TID that a particular type of electronics can withstand is a function of device materials and construction. Typical values are 1 to 10 kilorads for commercial electronics. Figure 22 shows the dose rate in rads/year in silicon, as a function of aluminum shielding thickness, in a 700-km sun-synchronous (98.19° inclination) circular orbit due to trapped particles. Data for this plot was generated by the SPace ENVIRONMENT Information System (SPENVIS) supported by the European Space Agency (ESA).<sup>8</sup> Trapped proton and electron fluxes and energy distributions were calculated using the AP-8 trapped proton and the AE-8 trapped electron models for January 1, 2020 through December 31, 2020. Total ionizing dose was calculated in silicon using the SHIELDOSE-2 model for a semi-infinite geometry.

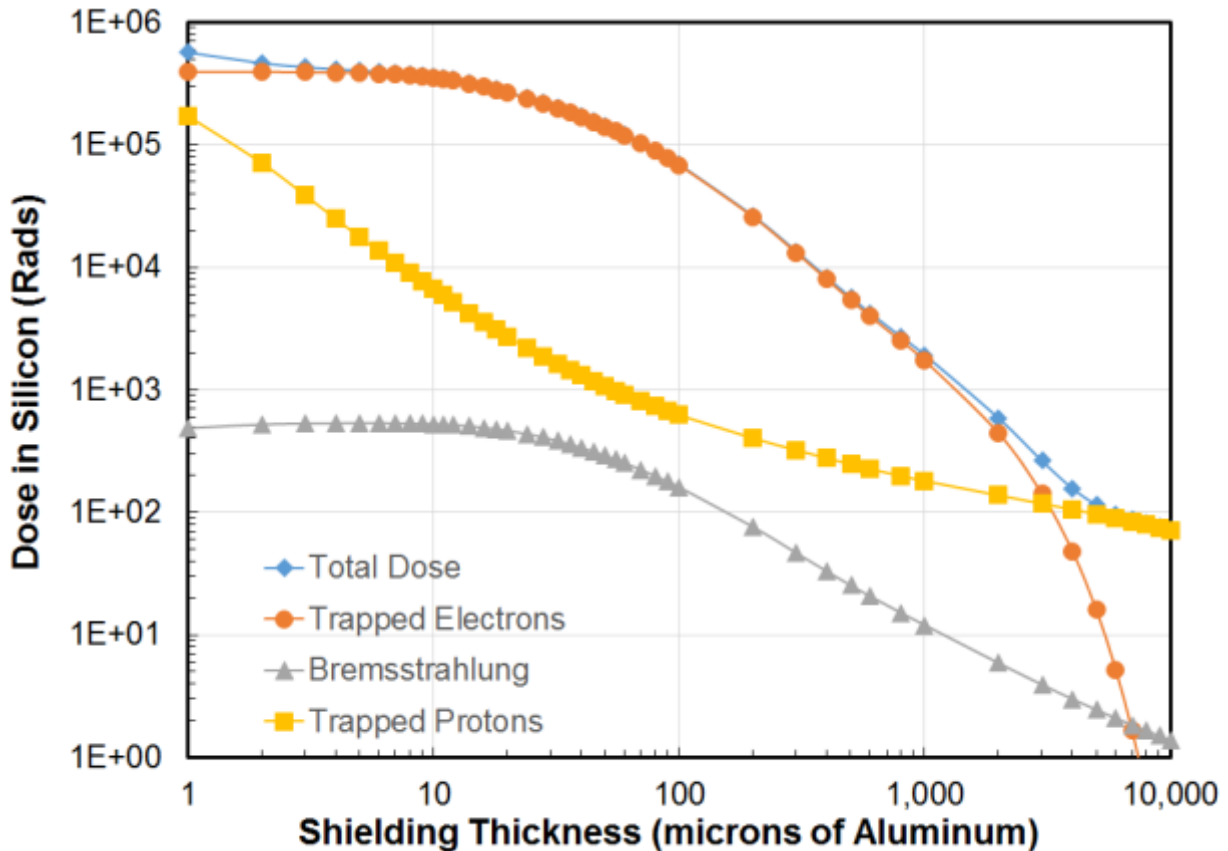
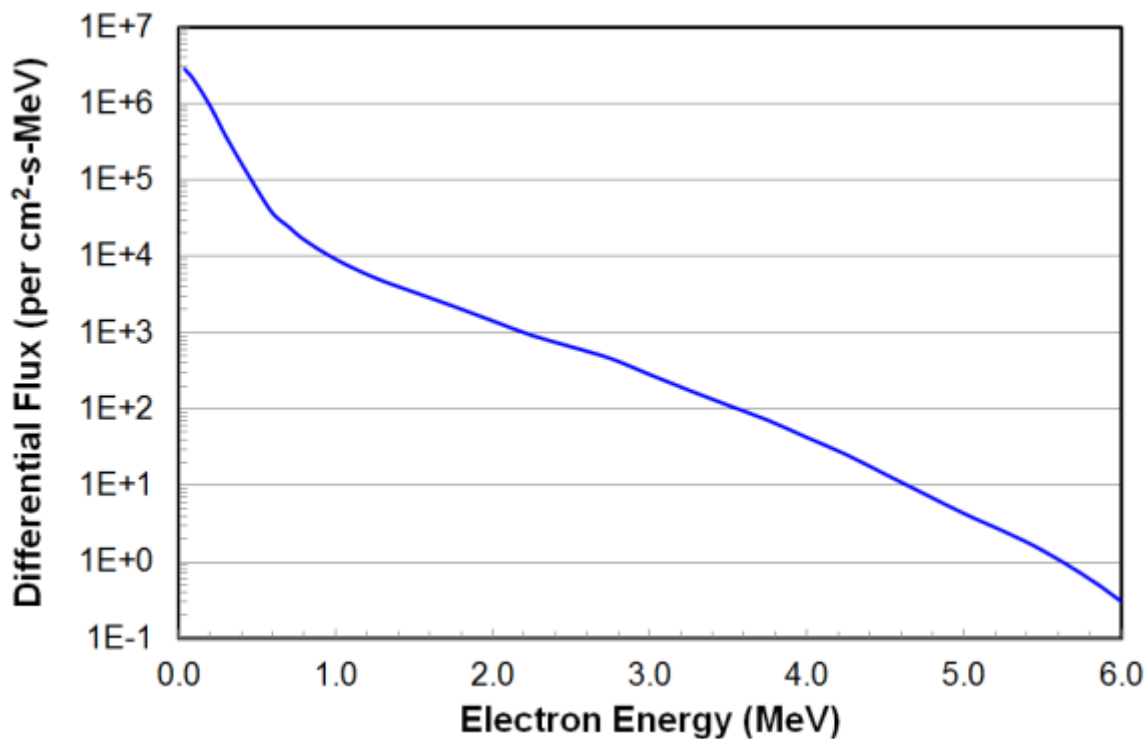


Figure 22. Yearly dose rate in rads/year in silicon as a function of aluminum shielding thickness for a 700-km circular, sun-synchronous (98.19° inclination) orbit. The AE-8 and AP-8 models generated the ambient particle distribution, and SHIELDOSE-2 used these inputs to generate the dos as a function of shield thickness for a semi-infinite slab. The vertical scale is dose in silicon in rads, and is logarithmic ranging from 1 at the bottom to a megarad at the top. The horizontal scale is shielding thickness of aluminum and is logarithmic ranging from 1 micron on the left to 10,000 microns on the right. The dose rate due to electrons starts at 390,000 rads/year at 1 micron, is flat at this level through 10 microns, and then curves down to 68,600 rads/year at 100-microns thickness. The electron dose drops further to 1,700 rads/year at 1-mm thickness, and then drops more rapidly to hit 1 rad/year at 7.5-mm thickness. Dose due to protons is the next largest component, starting at 170,000 rads/year at 1 micron, dropping down to 6,700 rads/year at 10 microns, 620 rads/year at 100 microns, 180 rads/year at 1 mm, and 71 rads/year at 1-cm thickness. Bremsstrahlung starts at 490 rads/year at 1 micron, rises slightly to 530 rads/year at 7 microns, remains fairly flat to 460 rads/year at 20 microns, and then drops to 1.4 rads/year at 10-mm thickness.

The radiation dose has three components: electrons, protons, and “braking radiation” (bremsstrahlung); photons generated by the slowing down of protons and electrons. For this orbit, trapped electrons dominate the dose for shielding thicknesses less than 3 mm. Most spacecraft have from 1 to 5 mm (1,000 to 5,000 microns) of aluminum shielding, so electronics with a maximum 5 kilorad TID could function from 2.5 through 43 years in this orbit. Brane Craft have significantly less shielding; about 10 microns of Kapton® above the electronics and 30 microns

below. If the shielding were aluminum, and the “bottom” shielding thickness was large enough to approach semi-infinite shielding, the total dose rate using 10 microns of top shielding would be 360,000 rads/year and a 5 kilorad TID limit would be reached after 5 days in this orbit.

How effective is Kapton® as a radiation shield? Ions and electrons are slowed by interactions with electrons and atomic nuclei as they traverse a shield material, semiconductor, etc. This slowing is characterized by the stopping power which has units of MeV/micron. Stopping powers for electrons and protons are radically different, and they are a function of particle energy. Figure 23 shows the average electron differential energy distribution from the AE-8 model for this orbit as calculated by SPENVIS, and Figure 24 shows the average proton differential energy distribution from the AP-8 model. Figure 25 shows both energy distributions plotted using linear scales from 0 to 2 MeV.



*Figure 23. Average differential electron energy distribution in a 700-km, sun-synchronous orbit. The vertical scale is differential electron flux per square cm, per second, per MeV. It is a logarithmic scale ranging from 0.1 at the bottom to 10 million electrons per square cm, per second, per MeV at the top. The horizontal scale is electron energy in MeV. It is a linear scale ranging from 0 on the left to 6 MeV on the right. The differential flux curve starts at 2.8 million at 40 keV and decreases rapidly to 37,000 electrons per square cm, per second, per MeV at 600 keV. From there, it decreases at a much slower rate to reach 0.3 electrons per square cm, per second, per MeV at 6 MeV.*

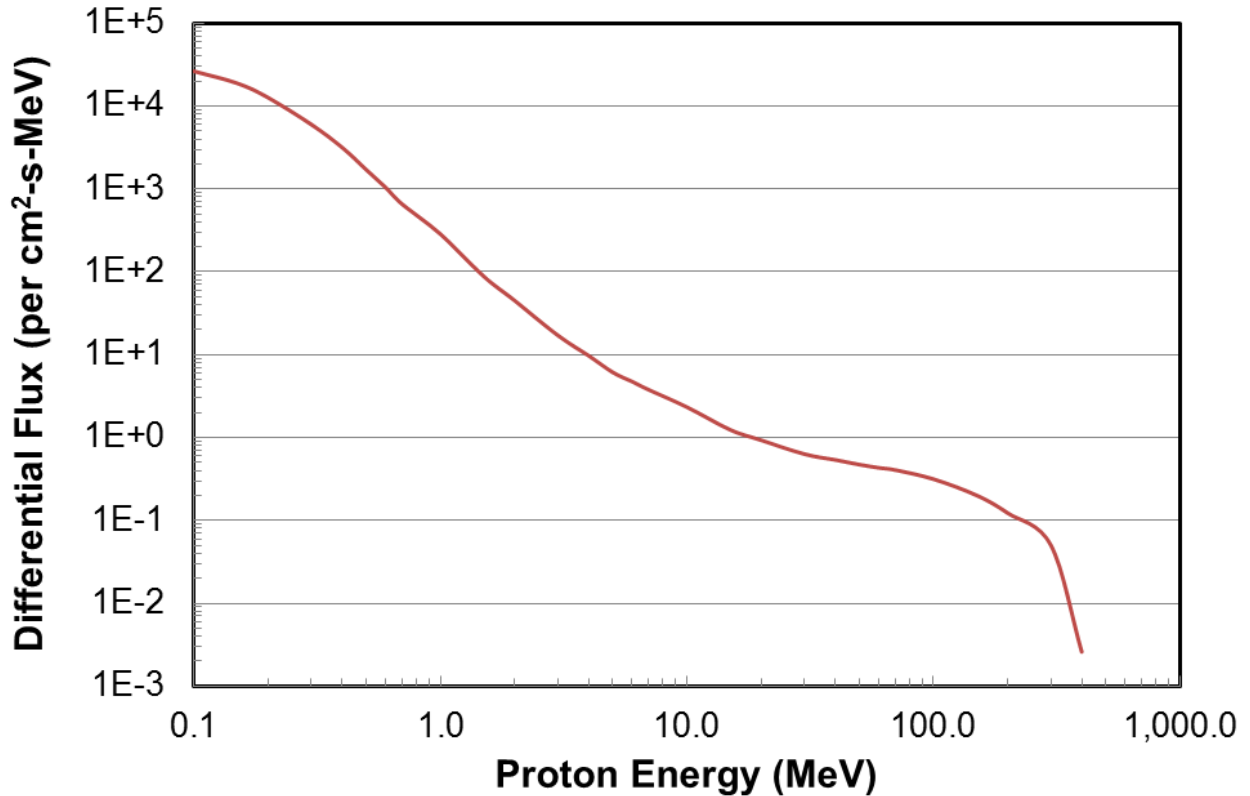


Figure 24. Average differential proton energy distribution in a 700-km, sun-synchronous orbit. The vertical scale is differential proton flux per square cm, per second, per MeV. It is a logarithmic scale ranging from 0.001 at the bottom to 100,000 protons per square cm, per second, per MeV at the top. The horizontal scale is proton energy in MeV. It is a logarithmic scale ranging from 0.1 on the left to 1 GeV on the right. The differential proton flux curve starts at 26 thousand at 0.1 MeV and decreases to 1,000 protons per square cm, per second, per MeV at 0.6 MeV. From there, it decreases in a fairly straight line to 0.3 protons per square cm, per second, per MeV at 10 MeV. It further decreases to 0.05 protons per square cm, per second, per MeV at 300 MeV and 0.0026 protons per square cm, per second, per MeV at 400 MeV.

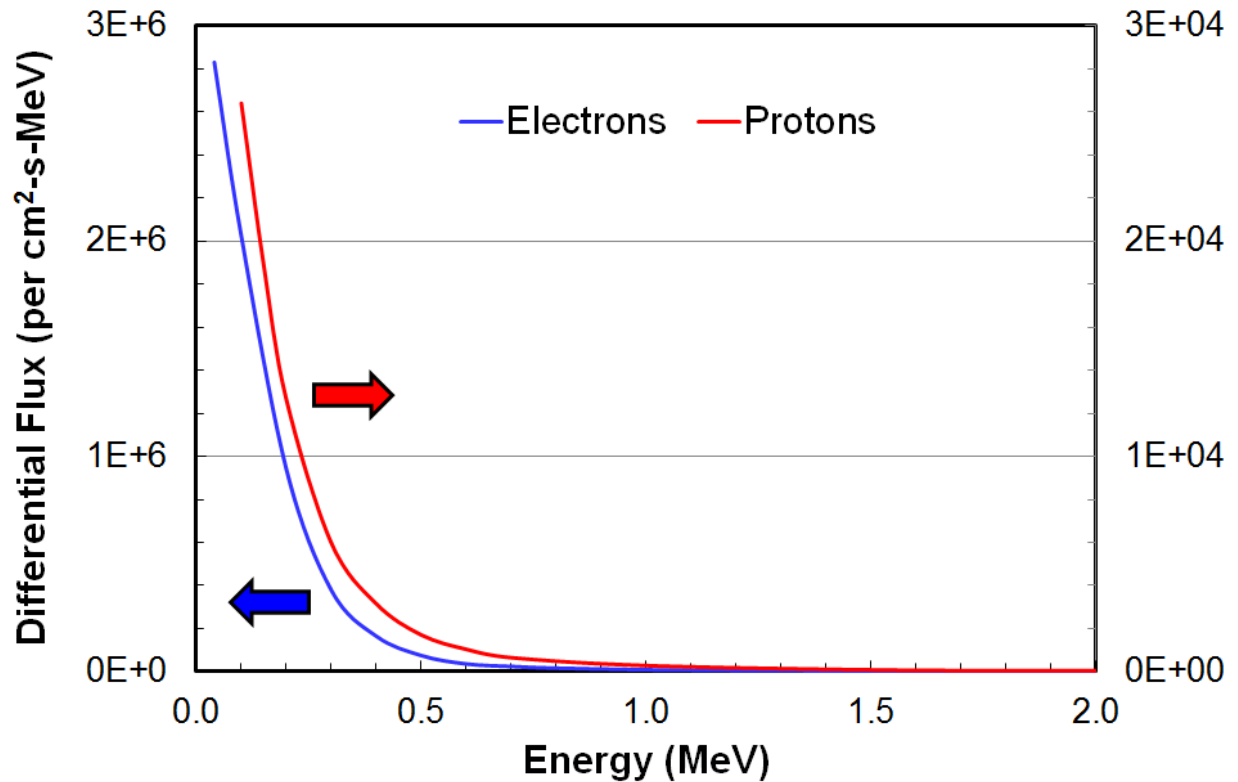


Figure 25. Average differential proton and electron energy distributions in a 700-km, sun-synchronous orbit. The left vertical scale is differential electron flux per square cm, per second, per MeV. It is a linear scale ranging from 0 at the bottom to 3 million per square cm, per second, per MeV at the top. The right vertical scale is differential proton flux per square cm, per second, per MeV. It is a linear scale ranging from 0 at the bottom to 30,000 per square cm, per second, per MeV at the top. The horizontal scale is energy in MeV. It is linear, ranging from 0 on the left to 2 MeV on the right. The electron differential flux starts at 2.8 million electrons per square cm, per second, per MeV and drops linearly to 380,000 electrons per square cm, per second, per MeV at 0.3 MeV. From there, it drops to essentially zero at this linear scale, but is really 25,000 electrons per square cm, per second, per MeV at 0.7 MeV. The proton differential flux starts at 26 thousand protons per square cm, per second, per MeV and drops linearly to 6,000 protons per square cm, per second, per MeV at 0.3 MeV. From there, it drops to essentially zero at this linear scale, but is really 200 protons per square cm, per second, per MeV at 1.2 MeV.

Based on Figure 25, over 99% of the electron flux and proton flux has energies below 1 MeV. As these particles traverse aluminum or Kapton<sup>®</sup>, they lose energy. The stopping power of electrons in Kapton<sup>®</sup> and aluminum as a function of energy is shown in Figure 26, and the stopping power of protons in Kapton<sup>®</sup> and aluminum as a function of energy is shown in Figure 27. These data were generated using the ESTAR stopping-power and range tables program for electrons provided by the National Institute for Standards and Technology (NIST), and the PSTAR equivalent for protons.<sup>9,10</sup> Figure 26 shows that the electron stopping power of Kapton<sup>®</sup> is 65% of the aluminum stopping power from 0.01 to 0.1 MeV, and decreases to 50% by 2 MeV. Figure 27 shows that the

proton stopping power of Kapton<sup>®</sup> is 78% to 93% of the aluminum stopping power from 0.01 to 0.13 MeV, and 93% to 69% of the aluminum stopping power from 0.13 to 2 MeV, and from 69% to 62% from 2 MeV to 100 MeV.

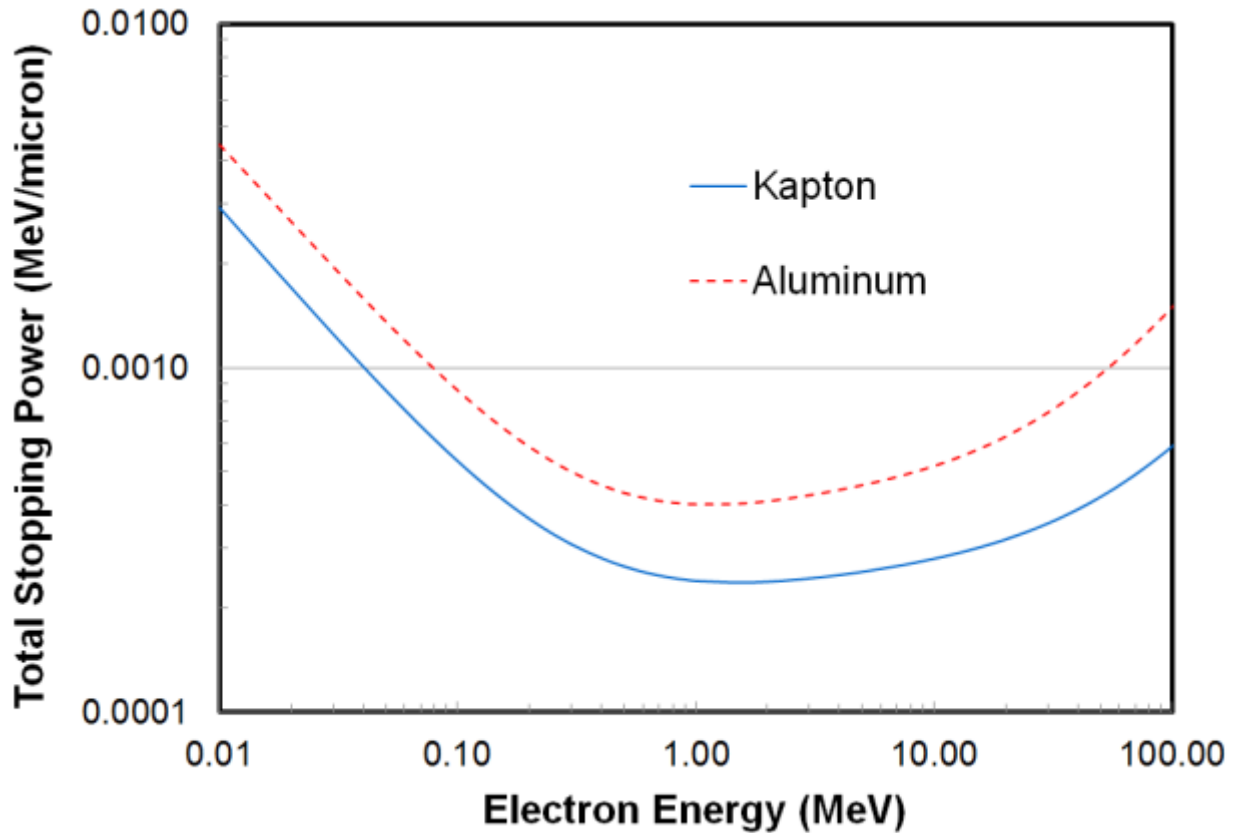


Figure 26. Total stopping power in MeV per micron as a function of electron energy in Kapton<sup>®</sup> and aluminum. The vertical scale is logarithmic starting at 0.0001 MeV per micron at the bottom and ending at 0.01 MeV per micron at the top. The horizontal scale is logarithmic starting at 0.01 MeV on the left and ending at 100 MeV at the right. The Kapton<sup>®</sup> curve starts at 0.0029 MeV per micron at 0.01 MeV energy, flattens out at ~0.00025 MeV per micron between 0.4 and 4 MeV. It then rises to 0.00059 MeV per micron at 100 MeV. The aluminum curve starts at 0.0045 MeV per micron at 0.01 MeV energy, flattens out at ~0.0004 MeV per micron between 0.7 and 2 MeV. It then rises to 0.0015 MeV per micron at 100 MeV.

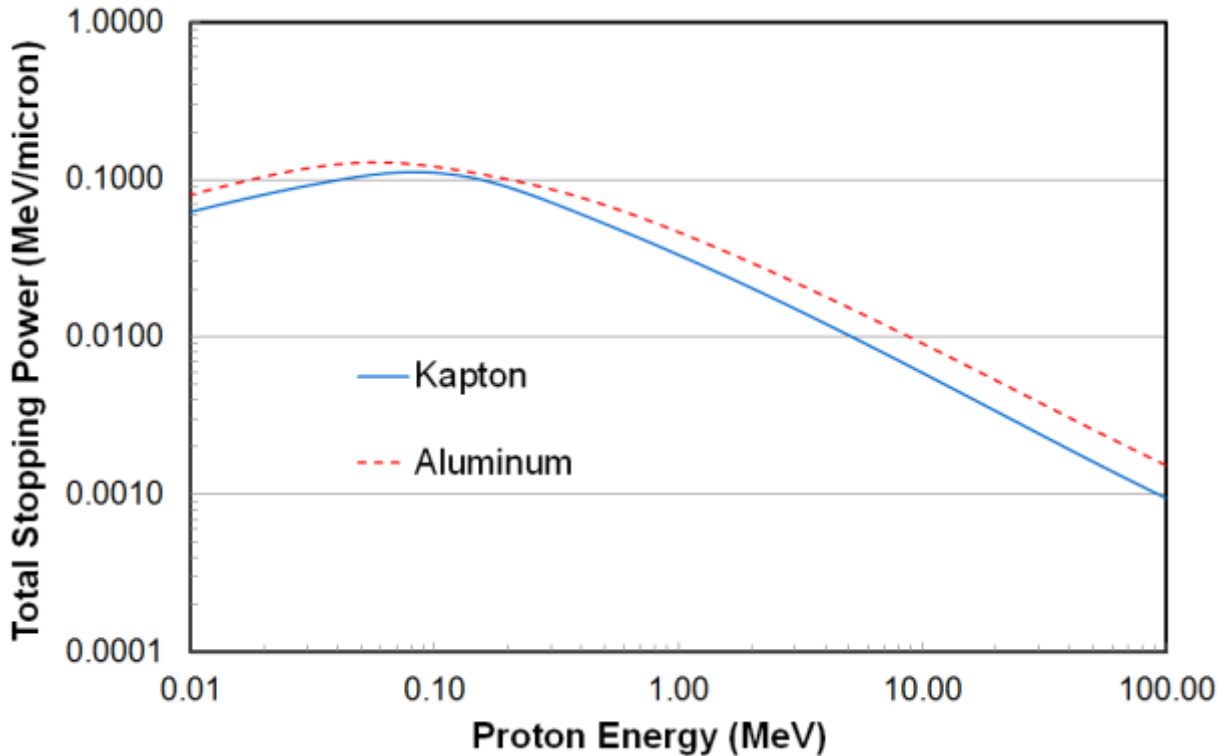


Figure 27. Total stopping power in MeV per micron as a function of proton energy in Kapton<sup>®</sup> and aluminum. The vertical scale is logarithmic starting at 0.0001 MeV per micron at the bottom and ending at 1 MeV per micron at the top. The horizontal scale is logarithmic starting at 0.01 MeV on the left and ending at 100 MeV at the right. The Kapton<sup>®</sup> curve starts at 0.063 MeV per micron at 0.01 MeV energy and rises to 0.11 MeV per micron at 0.8 MeV. It then drops to 0.001 MeV per micron at 100 MeV. The aluminum curve starts at 0.08 MeV per micron at 0.01 MeV energy and rises to 0.13 MeV per micron at 0.6 MeV. It then drops to 0.0015 MeV per micron at 100 MeV.

Since electrons dominate the dose curves for thin radiation shielding in LEO, and since the differential electron energy distribution is negligible above 0.7 MeV, the equivalent aluminum thickness is ~60% of the Kapton<sup>®</sup> thickness; 10 microns of Kapton<sup>®</sup> is roughly equal to 6 microns of aluminum and 30 microns of Kapton<sup>®</sup> is roughly equal to 18 microns of aluminum. Figure 28 shows the yearly total dose in silicon for a Brane Craft as a function of altitude for 0°, 30°, 60°, and 90° inclination orbits. These dose rates were obtained by adding the semi-infinite slab dose rates for 6 microns and 18 microns of aluminum shielding, at each altitude and inclination. Figure 28 shows maximum yearly total dose values of 190,000 rads at 400-km altitude to 92 megarads at 2000-km altitude. The vast majority of orbital debris lie between 60° and 90° inclination, so the upper limit can be relaxed to 43 megarads per year. For a maximum of 3-weeks at this 2000-km altitude, the maximum total dose is 830,000 kilorads; well beyond the limit of conventional silicon electronics. For an ISS orbit, similar calculations yield a yearly total dose of 180,000 rads. Standard COTS Brane Craft electronics with a 5 kilorad TID limit would operate for up to 10 days in an ISS orbit.

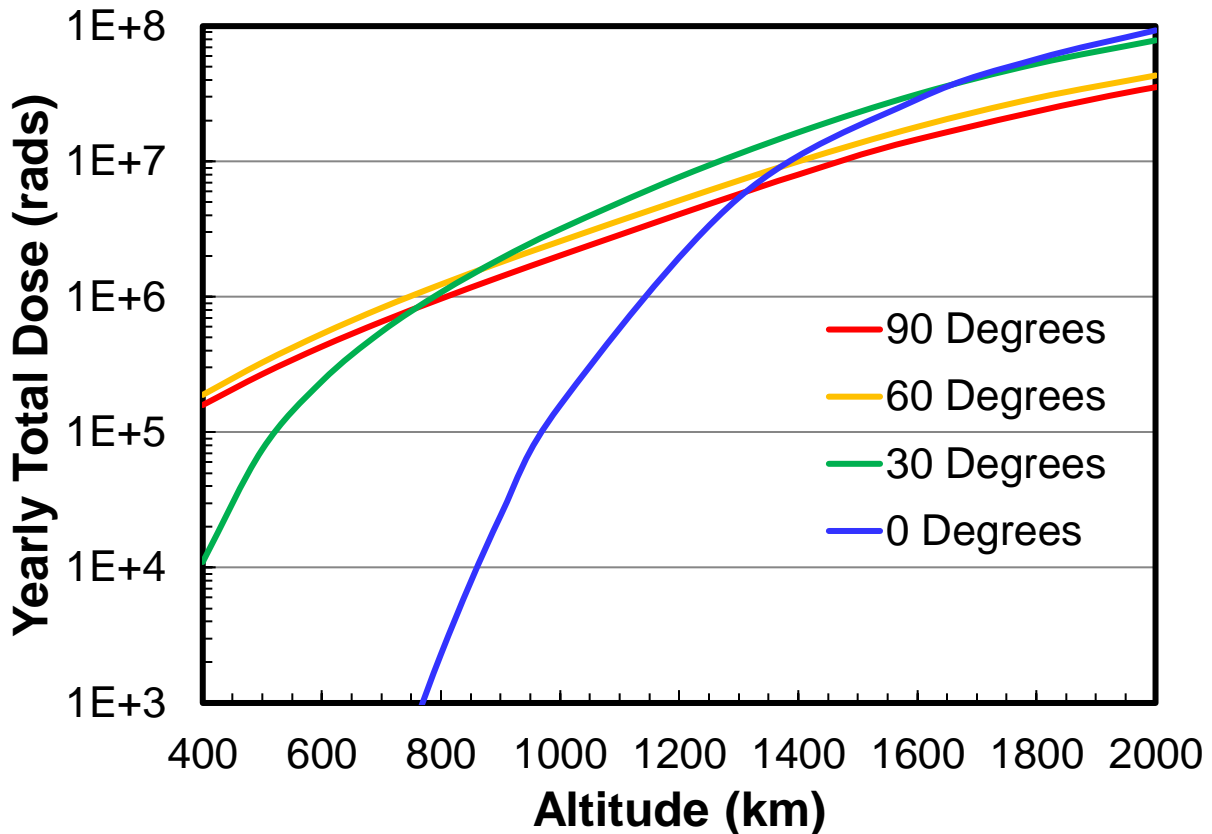


Figure 28. Yearly total dose rates as a function of altitude for 0°, 30°, 60°, and 90° inclinations for a Brane Craft with 10 microns of Kapton® shielding on one side, and 30 microns of Kapton® shielding on the other side. The vertical scale is logarithmic ranging from 1000 rads at the bottom to 100 megarads at the top. The horizontal scale is linear ranging from 400 km altitude on the left to 2000 km altitude on the right. The 0° inclination curve starts at 1 kilorad at 770 km and rises rapidly to 5.4 megarads at 1300 km, to 93 megarads at 2000 km altitude. The 30° inclination curve starts at 11 kilorads at 400 km and rises to 7.7 megarads at 1200 km, to 78.5 megarads at 2000 km altitude. The 60° inclination curve starts at 190 kilorads at 400 km and rises to 5.2 megarads at 1200 km, to 43 megarads at 2000 km altitude. The 90° inclination curve starts is slightly lower at 160 kilorads at 400 km and rises to 4.1 megarads at 1200 km, to 35 megarads at 2000 km altitude.

Figure 29 shows yearly total dose results for a more conventional spacecraft, such as a CubeSat, with 1 mm of aluminum shielding. This is representative of some CubeSats with skeletal aluminum frames and circuit boards as shielding, and for sun and Earth sensor electronics behind a thin optical window. Overall, the dose rates are about 1000 times lower than for a Brane Craft. Conventional COTS electronics with a 5 kilorad TID limit would work for about a year at altitudes up to 1000 km. To go higher, thicker shielding is required.

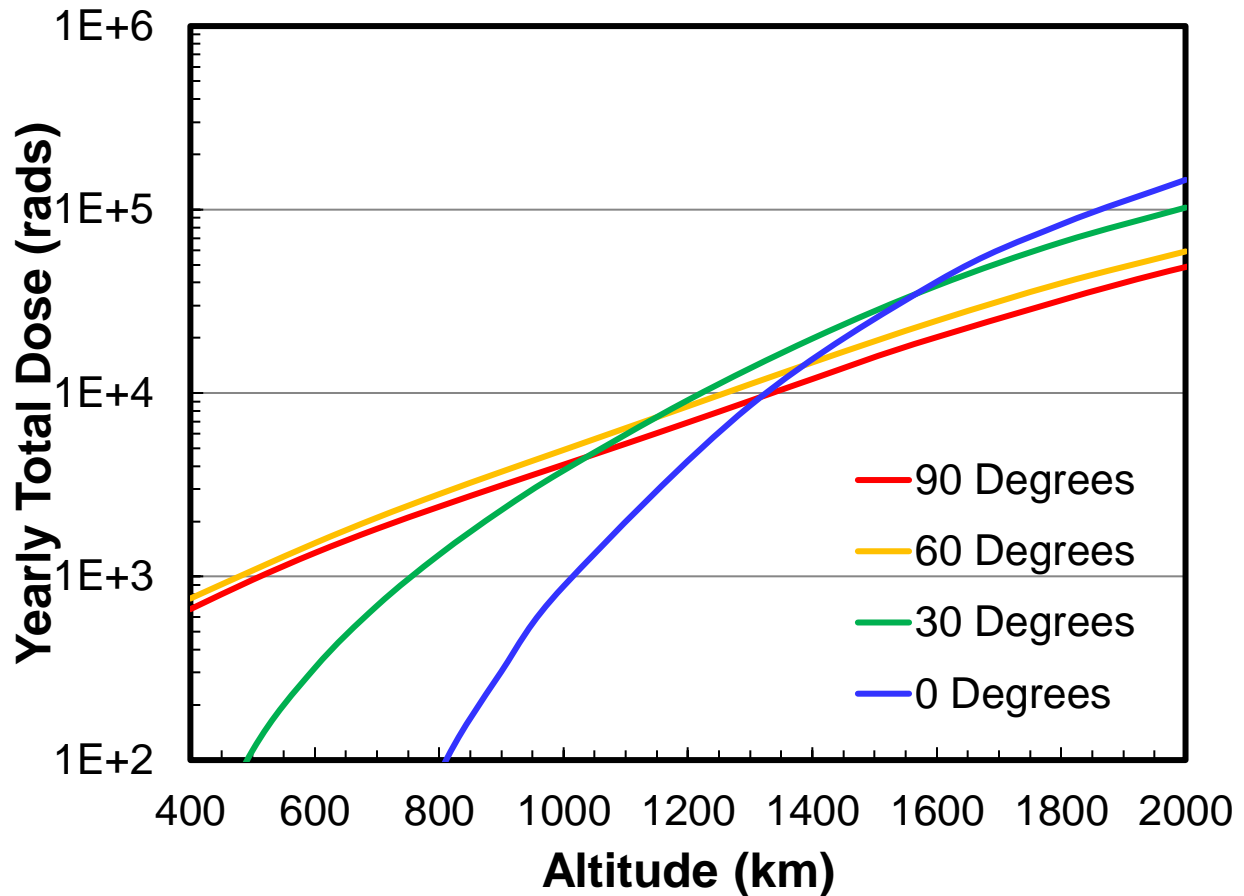


Figure 29. Yearly total dose rates as a function of altitude for 0°, 30°, 60°, and 90° inclinations for a conventional spacecraft with 1 mm of aluminum shielding. The vertical scale is logarithmic ranging from 100 rads at the bottom to 1 megarad at the top. The horizontal scale is linear ranging from 400 km altitude on the left to 2000 km altitude on the right. The 0° inclination curve starts at 100 rads at 810 km and rises rapidly to 8.5 kilorads at 1300 km, to 145 kilorads at 2000 km altitude. The 30° inclination curve starts at 100 rads at 500 km and rises to 9.2 kilorads at 1200 km, to 103 kilorads at 2000 km altitude. The 60° inclination curve starts at 760 rads at 400 km and rises to 8.5 kilorads at 1200 km, to 59 kilorads at 2000 km altitude. The 90° inclination curve starts is slightly lower at 660 rads at 400 km and rises to 6.9 kilorads at 1200 km, to 49 kilorads at 2000 km altitude.

### Findings for 3.6 The Radiation Environment:

1. The maximum dose rate for a Brane Craft in LEO is 92 megarads/year.
2. The maximum dose rate for a Brane Craft in LEO at inclinations greater than 60° is 43 megarads/year.
3. The Brane Craft dose rate in an ISS orbit is 0.18 megarads/year.

### 3.7 The Micrometeoroid and Particulate Debris Environment

The LEO environment is also full of micrometeoroids and micron-scale debris objects that can sever space tethers and perforate membrane spacecraft. Figure 30 shows the size distribution of micrometeoroids in a 1,200 km altitude circular orbit according to the Grün interplanetary flux and MASTER micrometeoroid and debris models available on SPENVIS.<sup>11,12</sup> The Micrometeoroid And Space debris Terrestrial Environment Reference (MASTER) model by ESA is the 2009 version that includes natural micrometeoroids plus man-made objects such as explosion fragments, collision fragments, paint flakes, solid rocket aluminum oxide particulates, etc., assuming “business as usual”; no anti-satellite tests or improved debris prevention measures. Note that the micrometeoroid flux for 10-micron diameter particles is 132 particles per year for a 1-square meter Brane Craft, 2 particles per year at 100-micron diameter, and 0.3/year at 200-micron diameter. Adding in man-made debris increases these numbers to 380/year for 10-micron diameter objects, 23/year for 100-micron diameter objects, and 2/year for 200-micron diameter objects.

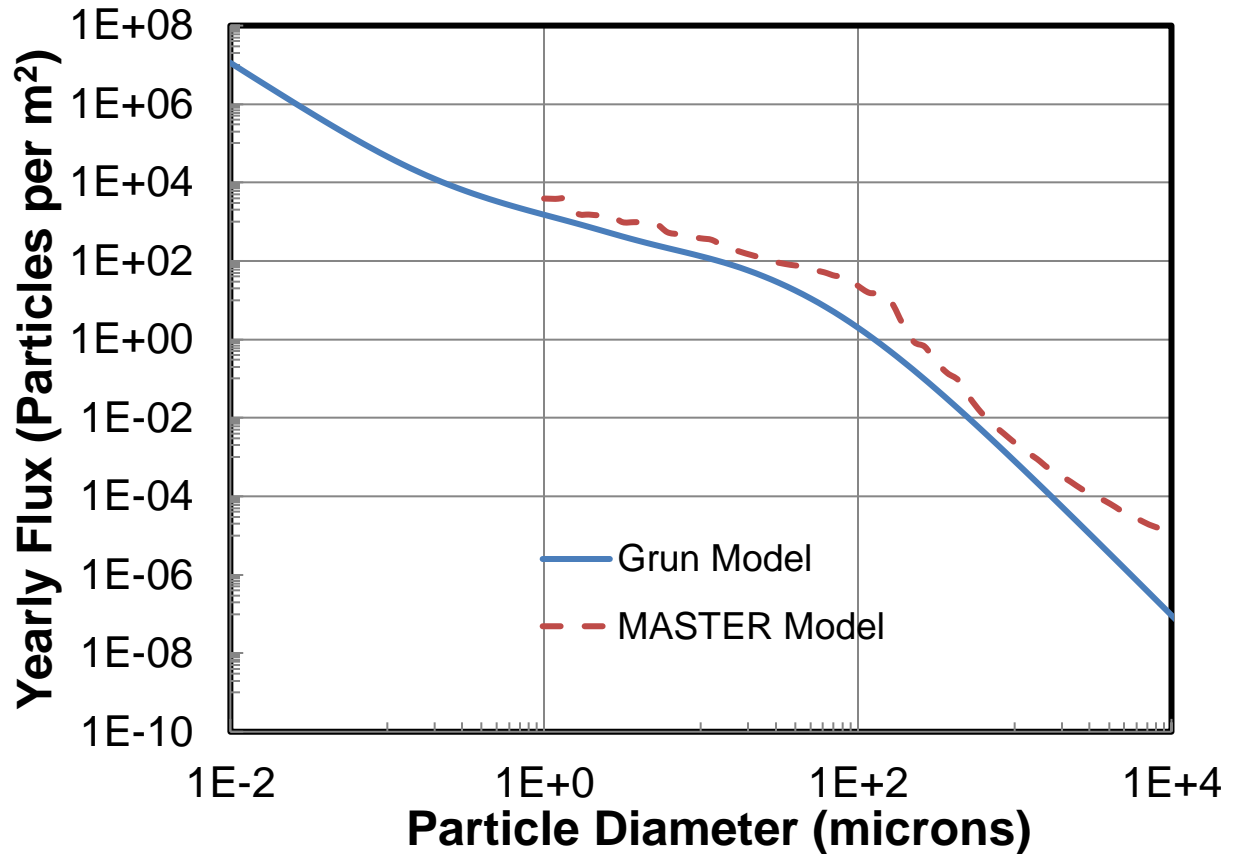


Figure 30. Yearly particle flux vs particle diameter in a 1,200-km altitude circular orbit according to the Grün and MASTER 2009 models. The vertical scale is yearly flux in particles per square meter, ranging logarithmically from  $10^{-10}$  at the bottom to  $10^8$  at the top. The horizontal scale is particle diameter in microns and ranges from 0.01 on the left to 10,000 on the right. The Grün curve starts at  $1.1 \times 10^7$  particles per square meter per year at 0.01 micron diameter, drops to 1500 particles per square meter per year at 1 micron diameter, to 132

particles per square meter per year at 10 micron diameter, to 2 particles per square meter per year at 100 micron diameter, to  $9.3 \times 10^{-8}$  particles per square meter per year at 10 mm diameter. The Master 2009 curve starts at 3900 particles per square meter per year at 1 micron diameter, drops to 380 particles per square meter per year at 10 micron diameter, to 23 particles per square meter per year at 100 micron diameter, to 3 particles per square meter per year at 200 micron diameter.

What size particle can penetrate 10 and 20 microns of Kapton®? Gas gun experiments have shown that a hole diameter to thickness ratio of 2, indicative of penetration through a single wall or sheet, occurs at a particle diameter/thickness ratio of 0.7 for a 5 km/s soda-lime glass spherical particle impacting Kapton® at normal incidence.<sup>13</sup> At 5-km/s incident velocity, a 7-micron diameter particle would penetrate a 10 micron thick Kapton® sheet, and a 14 micron diameter particle would penetrate 20 microns of Kapton®. The critical mass  $m_c$  in grams, needed to penetrate a wall, for a particle with density  $\rho$  in g/cm<sup>3</sup> impacting at velocity  $V$  in km/s is given by:

$$m_c = [ 2.54 t / (K_t \rho^{1/6} V^{7/8}) ]^{1/0.352} \quad (4)$$

where  $t$  is wall thickness in inches and  $K_t$  is a material constant, typically 5.4 for aluminum alloys.<sup>14</sup> Entering the velocity, thickness, density, and calculated mass based on particle diameter yields  $K_t = 0.89$  for Kapton®. At  $V = 10$  km/s, the critical particle diameters drop to 4 and 8 microns. Table 3 shows the critical diameters calculated using Eq. 4 to penetrate 10 and 20 microns of Kapton®, and the yearly rate of those penetrations, for impacting velocities of 5, 10, 14, and 20 km/s. The number of yearly impacts is lower at 20 km/s than the others because only micrometeoroids have these impact velocities. These numbers are for impacts normal to the surface of a one square meter sheet, and actual values will be lower; 50% lower is a good first estimate based on the average of the cosine over all impacting angles. Using this estimate, Table 3 shows that for a one-month long mission, a 10-micron thick Kapton® layer will be breached ~42 times. A 20-micron thick Kapton® layer will be breached ~21 times. The number of breaches can be reduced by a factor of 3 by leaving the Brane Craft curled up whenever possible.

Table 3. Critical particle diameters, and yearly impact rates per square meter for those diameters and larger, to penetrate 10 and 20-micron thick Kapton® sheets for normal incident velocities of 5, 10, 14, and 20 km/s.

Velocity (km/s)	D <sub>c</sub> for 10 μ Kapton® (μ)	D <sub>c</sub> for 20 μ Kapton® (μ)	Penetrating Yearly Impacts for 10 μ Kapton®	Penetrating Yearly Impacts for 20 μ Kapton®
5	7	14	480	230
10	4.1	8.2	970	400
14	3.1	6.2	1000	500
20	2.4	4.8	600	270

### Findings for 3.7 The Micrometeoroid and Particulate Debris Environment:

1. About 11 micrometeoroids of ~10-micron diameter and larger can hit a Brane Craft over a one-month long mission.
2. The odds of getting hit by a ~100-micron diameter micrometeoroid is 1 in 6 over a one-month long mission.
3. The population of man-made debris objects over the 1 to 100 micron diameter range in LEO is larger than the micrometeoroid population.
4. A 1 square meter flat Brane Craft in LEO will be hit by ~42 particles per month, micrometeoroids plus man-made objects, that will penetrate 10-micron thick Kapton® walls.
5. Brane Craft should be curled into a cylinder whenever possible to minimize the number of penetrating impacts.

## 4. Improved Brane Craft Design

### 4.1 Structure

The pre-phase I Brane Craft was designed with a 16 km/s delta-V capability to enable removal of orbital debris objects up to 2-kg in mass from low earth orbit, to enable removal of multiple items with smaller mass, and to explore thousands of asteroids and other objects within the solar system. The pre-phase I design was composed of two 7-micron thick Kapton® sheets, plus deposited electronics and solar cells, with a propellant cavity sandwiched in between. The initial *equivalent* Kapton® thickness at the start of this effort was 16 microns; 14 microns of Kapton® plus an assumed 2 microns of deposited dielectrics. After analysis of the solar cell and electronics layer thicknesses that coated one side of each structural layer, the total *equivalent* Kapton® thickness was increased to 24 microns to account for multi-micron thick layers of semiconductors, dielectrics, and metals. Wet mass increased to 47 grams, and thruster operating time at full power increased to 22.6 hours.

Orbital analysis of Brane Craft with a 16-km/s total delta-V capability in low Earth orbit showed astoundingly responsive behavior. They could increase altitude by 700-km within 30 minutes while in direct sunlight, and go from an initial 400-km altitude circular orbit to Earth escape within 6 hours, including eclipses by the Earth. Typical electric thruster systems are designed for operating lifetimes of thousands of hours, but a Brane Craft needed only tens of hours.

Mission times were on the order of one month due to orbital mechanics and eclipse periods, and the need to wrap the Brane Craft around a piece of space debris that significantly decreased the available power to the thrusters. Based on the number of impacts that would breach a 10-micron thick Kapton® sheet over a potential one-month long mission, the logical option was to increase the structure thickness to lower the breach rates. In addition, spacecraft electronics could now be put behind a layer of Kapton® to provide extra radiation shielding.

Figure 31 shows thruster operating time as a function of total Kapton® thickness for 4 different specific impulses for a 1 square meter Brane Craft using 180 W of power for propulsion into 90%

thrust efficient engines with a propellant load to generate a 16 km/s delta-V. Figure 32 shows the initial “wet” mass (fully loaded with propellant) as a function of total Kapton® thickness for the same conditions.

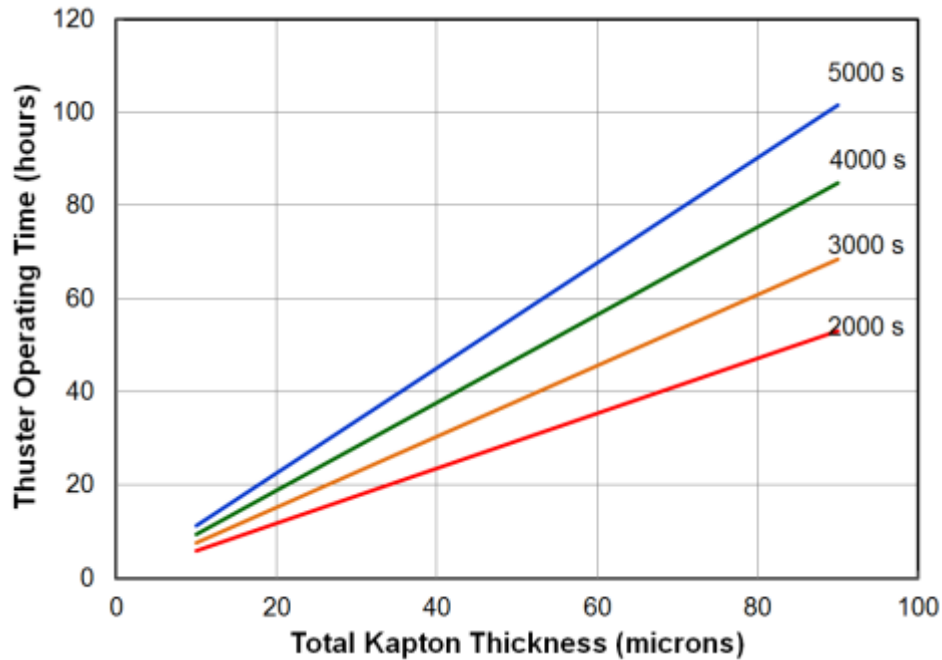


Figure 31. Thruster operating time as a function of total Kapton® thickness for a 1-square meter Brane Craft with 16 km/s delta-V, and specific impulses of 2000 s, 3000 s, 4000 s, and 5000 s. Engine input power is 180 W, and the thrust efficiency is 90%. The vertical scale is thruster operating time in hours and ranges linearly from 0 at the bottom to 120 at the top. The horizontal scale is total Kapton® thickness in microns and ranges linearly from 0 on the left to 100 on the right. The 2000 s specific impulse curve is a straight line starts at 5.9 hours at 10 micron thickness and ends at 51 hours at 90 micron thickness. The 3000 s specific impulse curve is a straight line starts at 7.6 hours at 10 micron thickness and ends at 68 hours at 90 micron thickness. The 4000 s specific impulse curve is a straight line starts at 9.4 hours at 10 micron thickness and ends at 85 hours at 90 micron thickness. The 5000 s specific impulse curve is a straight line starts at 11.3 hours at 10 micron thickness and ends at 102 hours at 90 micron thickness.

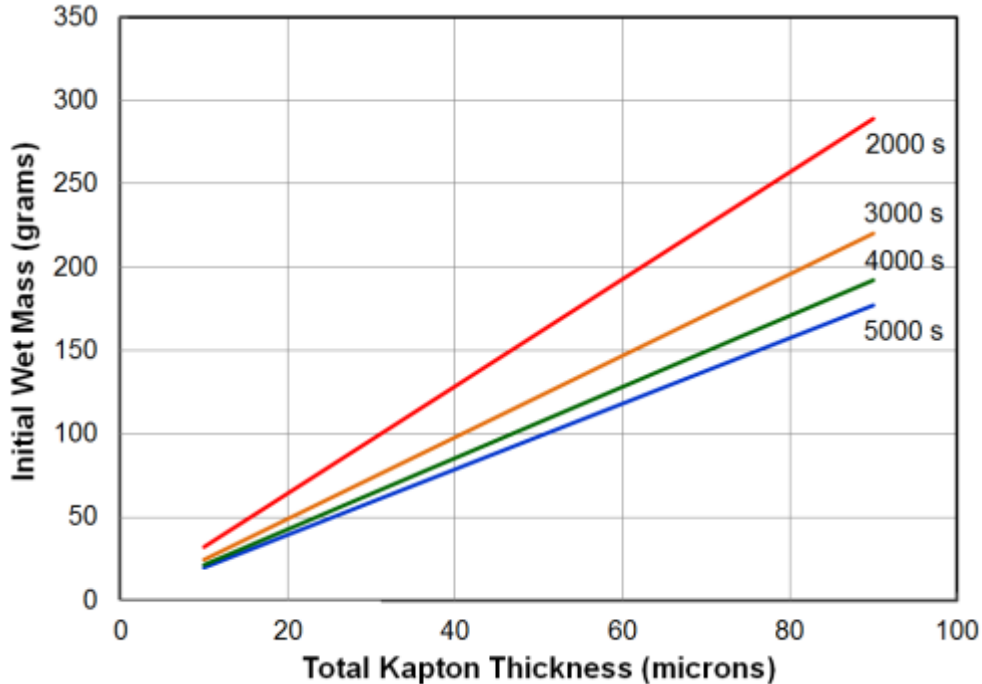


Figure 32. Initial wet mass as a function of total Kapton® thickness for a 1-square meter Brane Craft with 16 km/s delta-V, and specific impulses of 2000 s, 3000 s, 4000 s, and 5000 s. Engine input power is 180 W, and the thrust efficiency is 90%. The vertical scale is initial wet mass in grams and ranges linearly from 0 at the bottom to 350 grams at the top. The horizontal scale is total Kapton® thickness in microns and ranges linearly from 0 on the left to 100 on the right. The 2000 s specific impulse curve is a straight line that starts at 32.1 grams at 10 micron thickness and ends at 289 grams at 90 micron thickness. The 3000 s specific impulse curve is a straight line that starts at 24.5 grams at 10 micron thickness and ends at 220 grams at 90 micron thickness. The 4000 s specific impulse curve is a straight line that starts at 21.4 grams at 10 micron thickness and ends at 192 grams at 90 micron thickness. The 5000 s specific impulse curve is a straight line that starts at 19.7 grams at 10 micron thickness and ends at 177 grams at 90 micron thickness.

The manufacture of thin film solar cells, electronics, sensors, and actuators require different processing steps, some of which occur in vacuum. After studying the types of equipment needed to produce 1 to 10-micron resolution features for Brane Craft electronics, it seemed prudent to print or deposit electronics on 30 cm x 30 cm or smaller substrates rather than 100 cm by 100 cm substrates. The 1 square meter sheets were still needed to hold the propellant, but they could also act as a circuit board to electrically connect smaller Kapton® sheets with specific functions. Figure 33 shows a schematic cross section of the new design. Total effective Kapton® thickness increases to 38 microns, with an initial wet mass of 81 grams and a maximum thruster operating time of 36 hours. Propellant mass is 27 grams. This design provides 7 microns of additional radiation shielding for the thin film electronics, extra particulate shielding, and makes the electronics, solar cells, sensors and actuators easier to fabricate. It also allows replacement and upgradeability of specific spacecraft functions over time.

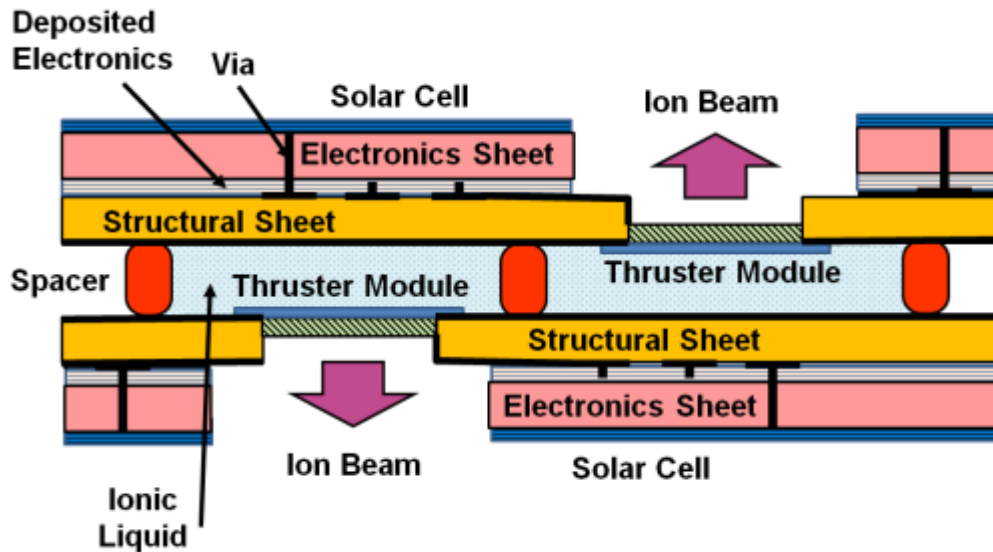
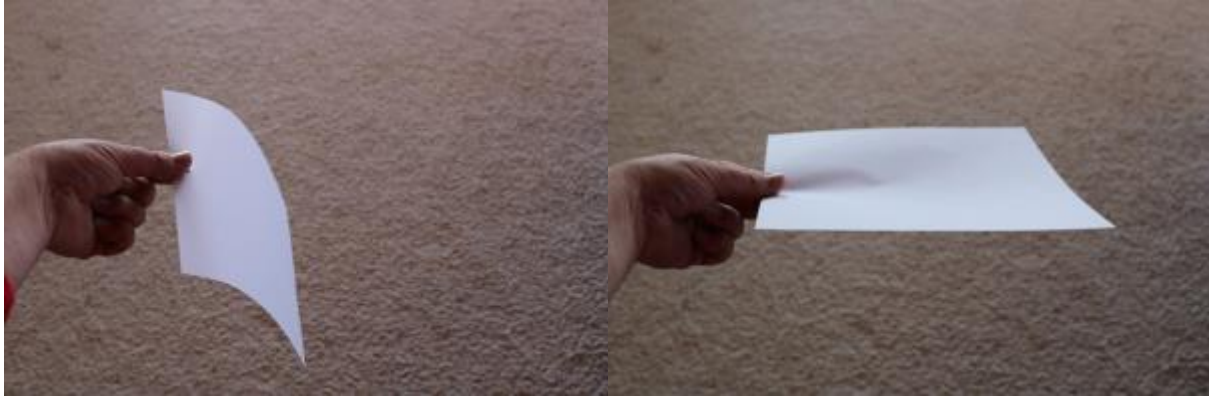


Figure 33. Schematic cross section of the new Brane Craft structural design. The basic structure is composed of two 7-micron thick Kapton® sheets separated by 21 microns to hold 27 grams of ionic liquid propellant with a density of 1.3 grams/cm<sup>3</sup>. Distributed spacers separate the sheets, and electrically isolate propellant storage regions from thruster module regions. Thruster modules sit in holes in the structural sheets to be in contact with the propellant. The main structural sheets have deposited traces to interconnect solar cell, electronic, sensor, and actuator sheets that are bonded to the outer surfaces.

### Real Brane Craft Have Curves

Brane Craft have to wrap around a debris object, but they also need curvature to maintain some degree of structural rigidity. Figure 34 shows two photos of a hand holding an 8.5" x 11" sheet of 24-pound paper; 119-microns thick with an areal density of 90 grams per square meter. The left image shows a limp piece of paper hanging straight down while the right image shows a piece that withstands the bending moment applied by gravity. The difference between the two photos is the way the fingers hold the paper. The left image had the paper held between the thumb and index finger while the right image had the paper held between the thumb on top, and the index and middle fingers on the bottom. No curvature was applied to the paper in the left image, but a concave-up curvature was applied in the right image. Curvature applied along one edge of the Brane Craft can mechanically stabilize it against bending moments due to thrusting. Curvature can be applied throughout the square-meter structure to make an effectively rigid spacecraft.

Sheet curvature is also essential to collect sunlight while thrusting in any direction. Electrically-propelled spacecraft use gimbals on solar arrays and sometimes on thrusters to maximize power collection while thrusting. Brane Craft don't have gimbals, but they can warp their geometry to accomplish the same thing. Figure 35 shows the Brane Craft configuration when thrusting and not holding a debris object; the outbound configuration while thrusting. In this case, it is thrusting normal to the incident solar radiation. The whole spacecraft can rotate about the



*Figure 34. Example of curvature applied to a sheet of paper to stabilize it against gravity-induced bending. The left image shows a piece of paper held in the middle of the short side using a thumb and index finger. The paper curves downward due to gravity. The right image shows the same piece of paper held at the same spot, but this time using the thumb against the index and middle fingers. The piece of paper curves upward at the holding point, and more gradually upwards across the entire side. The paper is almost flat, and horizontal.*

spacecraft-sun line, so this configuration can thrust in any direction that is perpendicular to the incident solar radiation. Figure 36 shows options for thrusting towards, against, and at right angles to incident solar radiation. Since Brane Craft can rotate about a vertical axis in this figure while maintaining the same solar collection, thrusting in any direction while maintaining 80% or more solar collection is possible.

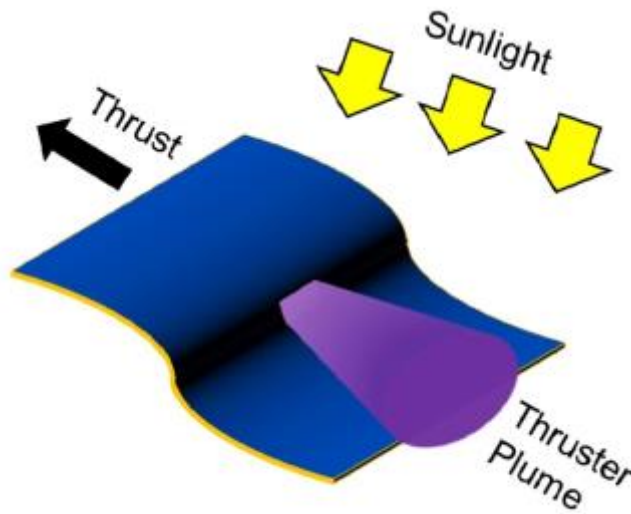


*Figure 35. Schematic drawing of a Brane Craft thrusting normal to the direction of sunlight. The drawing shows a Brane Craft curled into an “S” shape where the left side is almost horizontal, the sheet curves down more rapidly as it approaches the center, is vertical for 10% of the left-right length, curves upward past the center, and comes horizontal once again at the right edge. Sunlight illuminates one side of the Brane Craft from above, and the projected area of the Brane Craft is about 80%. The middle of the vertical section contains the primary thruster*

array, and an ion plume is shown exiting perpendicular to this surface. The thrust vector is in the opposite direction. The Brane Craft is uncurled in the other sheet direction.

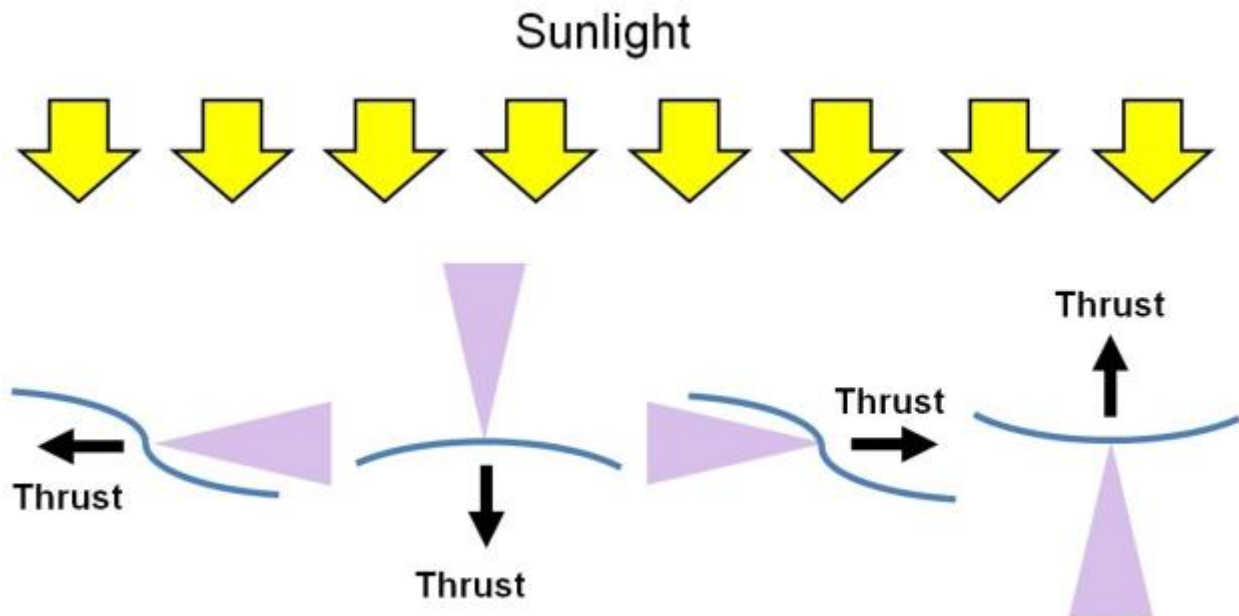
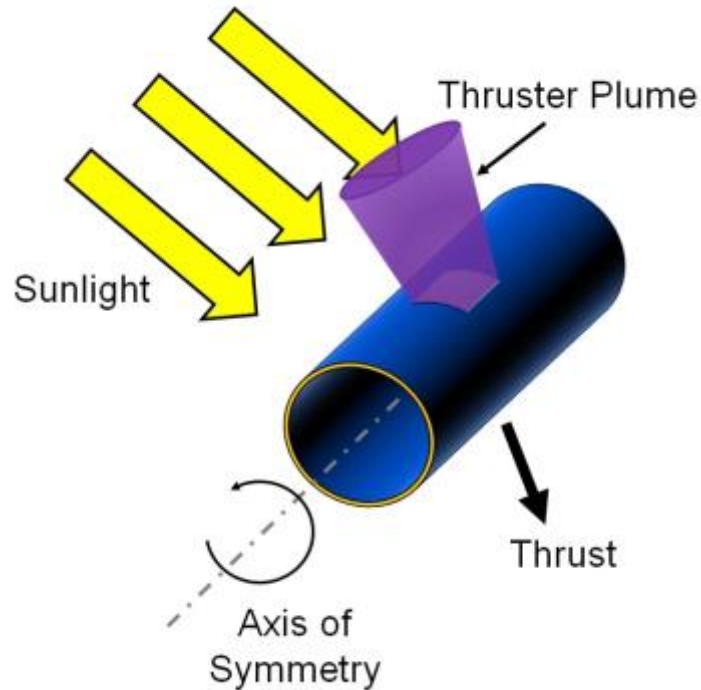


Figure 36. Four Brane Craft shapes and orientations to maximize solar collection while thrusting in four different perpendicular directions. Sunlight comes straight down from the top and each Brane Craft extends 1 meter into the page; there is no curvature in this direction. The leftmost drawing shows an “S” shaped Brane Craft cross section, like that in the previous figure, with a thrust vector to the left. The second drawing from the left shows a convex-up Brane Craft with a height of about 10% of the total horizontal width. Thrusters are in the middle horizontally, and the plume points straight upwards. The thrust vector is down. The third drawing from the left shows another “S” shaped cross section in the same orientation, but this time the thrust vector is horizontal to the right. This is indicative of the leftmost Brane Craft being rotated by 180° about an axis that comes straight out of the page, or firing of thrusters on the opposite side of the Brane Craft. The rightmost image shows a concave-up Brane Craft with a height of about 10% of the total horizontal width. Thrusters are in the middle horizontally, and the plume points straight downwards. The thrust vector is up. This is the same as the second from the left drawing, but rotated 180° about an axis that comes straight out of the page.

Brane Craft must also be able to thrust while curled around a debris object. In this case, the Brane Craft becomes a tube as shown in Figure 37. The axis of symmetry is perpendicular to the incoming solar radiation to maximize power. In this case, maximum power generation is  $(1/\pi) * 200 \text{ W} = 64 \text{ W}$ . The Brane Craft can rotate about the sunlight vector, and about the axis of symmetry. Since these are two orthogonal axes, the primary thruster array can generate thrust in any direction.



*Figure 37. Rendering of a Brane Craft curled about a debris object (not seen in this image) while thrusting. The Brane Craft is curled into a cylinder and the primary thruster array is generating a plume that is heading upwards and a little to the left. The thrust vector points mostly downward and a little to the right. Sunlight enters from the top left corner. The Brane Craft cylinder has an axis of symmetry that is perpendicular to the incident sun vector, and the thrusters can generate thrust in any direction about this axis.*

#### **Findings for 4.1 Structure:**

1. The Brane Craft design was changed to use two, 1 meter square large sheets to contain propellant and to act as a circuit board for other Kapton® sheets with deposited electronics, sensors, actuators, etc.
2. These sheets should be 12.5-microns thick to provide breakdown voltage resistance of at least 2400 V; twice the propellant potential.
3. The thicker sheets help reduce the number of small particle penetrations per month of operation in LEO.
4. The Brane Craft needs to be curved along at least one axis to provide some structural strength.
5. Curved geometries that allow thrusting in any direction, while maximizing solar power, have been found.

## 4.2 Solar Array Design

Last year, thin film solar cells represented about 7% of global solar cell production in terms of power generation capability (4.2 GW out of 63 GW).<sup>15</sup> Thin film solar cells can have a thickness less than 10 microns, and are thus extremely suitable for integration into active membrane spacecraft. Thin film Cadmium Telluride (CdTe) and Copper Indium Gallium Selenide (CIGS) solar cells on flexible substrates for terrestrial applications are commercially-available from Global Solar, SoloPower Systems, and MiaSolé. Flexible Cadmium Telluride (CdTe) and Copper Indium Gallium Selenide (CIGS) thin film cells have achieved sunlight-to-DC electric power conversion efficiencies of more than 21% at the cell level, and can provide 16% efficiency at the array level to generate desired power densities of up to 216 W/m<sup>2</sup> at 1 A.U. from the sun. Thin film amorphous silicon cells, by contrast, have efficiencies below 10% at the array level.

CIGS technology was chosen for the current Brane Craft design due to the thinner stack height of a CIGS cell (~5 microns) compared to a CdTe cell (8-10 microns). Figure 38 shows a schematic cross section of a 7-layer, ~5-micron thick, CIGS solar cell deposited on Kapton<sup>®</sup>. This cell has a patterned aluminum top contact with a nickel adhesion layer onto a Magnesium Fluoride (MgF) anti-reflection coating over a transparent Zinc Oxide (ZnO) or Indium Tin Oxide (ITO) conductor for distributed current collection. The photovoltaic generator is composed of a thin Cadmium Sulfide (CdS) layer deposited on the CIGS layer. The bottom contact is molybdenum, which also reflects unabsorbed photons back through the CIGS layer for improved absorption and efficiency. Although the stack height deposited on Kapton<sup>®</sup> is 5.1-microns high, about 90% of the top aluminum layer is missing to allow sunlight through. An additional advantage of CIGS solar cell technology is that CIGS cells have been shown to tolerate a TID of 100 kilograys (10 megarads).<sup>16</sup>

Individual CIGS solar cells have band gaps between 1.16 eV and 1.3 eV, depending on the gallium/indium ratio, and generate peak power voltages between 0.5 V and 0.6 V. The major power load is the electrospray thruster system at 180 W peak power; a maximum current of 150 mA at 1200 V. Spacecraft bus power is estimated at 20 W, 1,000 mA at 20V. Power conditioning and peak power tracking will be done using thousands of individual cells connected in various serial/parallel combinations to match the instantaneous output voltage requirements under current lighting conditions. The direct drive approach requires that ~36 cells be connected in series for generating 20 V, and ~2200 cells be connected in series to generate 1,200 V. This approach eliminates the need for inductors and large capacitors, but it does require thin film transistors and associated logic to perform power switching. Fortunately, thousands of cells, plus diodes, transistors, and connecting “wires” can be fabricated in parallel on a single substrate. Thin film bypass and blocking diodes are required to handle shaded or open cells. Figure 39 shows a schematic circuit for a solar array string and includes a description of how it works. Each string is resilient to shading and particle-induced cell shorts and open circuits.

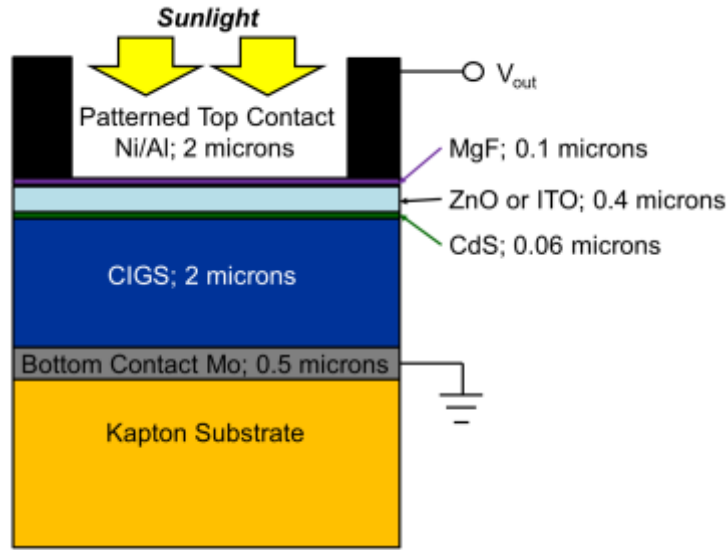


Figure 38. Schematic cross section of a CIGS solar cell on Kapton<sup>®</sup>. Listed dimensions are layer thicknesses. A 0.5-micron thick molybdenum layer is deposited on the Kapton<sup>®</sup> substrate. This base layer forms the negative electrode for the cell and reflects any photons that were able to traverse the semiconductor layer back through it to improve absorption. A 2-micron thick CIGS semiconductor layer is deposited on top of the molybdenum negative electrode. A 60-nm thick cadmium sulfide layer on top of the CIGS layer completes the semiconductor stack. A 0.4-micron thick zinc oxide or indium tin oxide layer on top of the semiconductor stack is used as the positive electrode, and 2-micron thick patterned layer of aluminum with a thin nickel adhesion layer on the bottom is used to collect the photocurrent. Most of this patterned layer is open so that light gets through, and the open regions have a 100-nm thick magnesium fluoride anti-reflection layer.

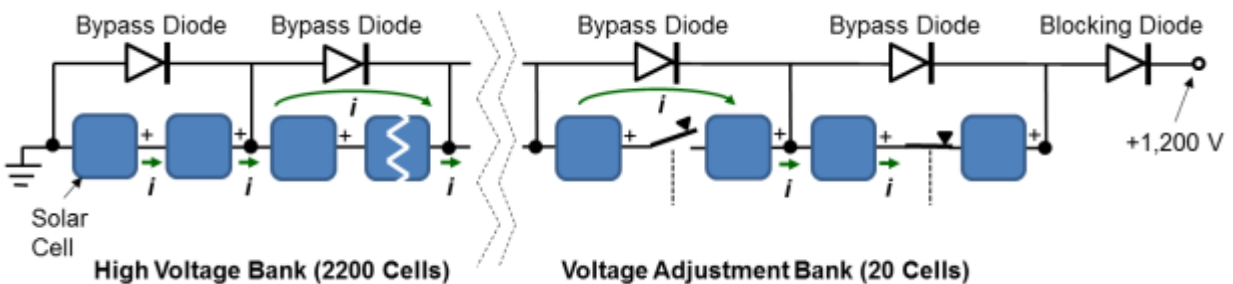


Figure 39. Circuit diagram for a high-voltage solar array string. Multiple solar cells connected in series, in this case two, form a sub-string. Each sub-string has a bypass diode connected to it to let current flow around the sub-string in case one of the cells is shadowed or open. The fourth cell from the left is shown as an open cell. If a cell is shorted in a sub-string, that sub-string produces half the voltage, and if both are shorted, no voltage is added. Under normal operation, current flows through each cell. The main power bank consists of 1100 substrings. A smaller, 10 sub-string voltage adjustment section is connected in series with the main power bank. The voltage adjustment bank has a switching transistor connected between each pair of solar cells in these substrings. The transistor is shown in this diagram as an electrically-controlled switch. If the switch is open, current flows through the bypass diode and no voltage is added. If the switch

is closed, the cells are connected in series and about 1 V is added to the total string voltage. A blocking diode is put between the end of the string and the high-voltage bus to prevent reverse current flow from the bus if the string voltage is low.

Individual strings span the Brane Craft in a direction parallel to the curling axis, with a width of 1/9 of the edge length; 11 cm. A high-voltage string is 85 cm x 11 cm in size, while the 20 V string is 10 x 11 cm in size. This allows all cells in a string to receive equal fluxes of sunlight when curled about a debris object. Figure 40 shows a flat Brane Craft with solar cell strings and other systems bonded to the surface. Curling axes are vertical. Each high-voltage string runs up and down across the Brane Craft surface, nine times, while each low voltage string runs up and down 3 times. Figure 40 shows only four columns of cells per string, corresponding to two up/down paths, in order to see individual cells at this image resolution. The high and low voltage bus lines are in close proximity to the ground busses to minimize current loops. Current loops can react with the Earth's magnetic field and generate a torque on the Brane Craft. Individual cells for the high-voltage string are 7 x 6 mm in size, and individual cells for the low-voltage string are 16.7 x 18 mm in size. Both sides of a Brane Craft are covered in solar cells, sensors, thrusters, and actuators for redundancy and increased robustness.

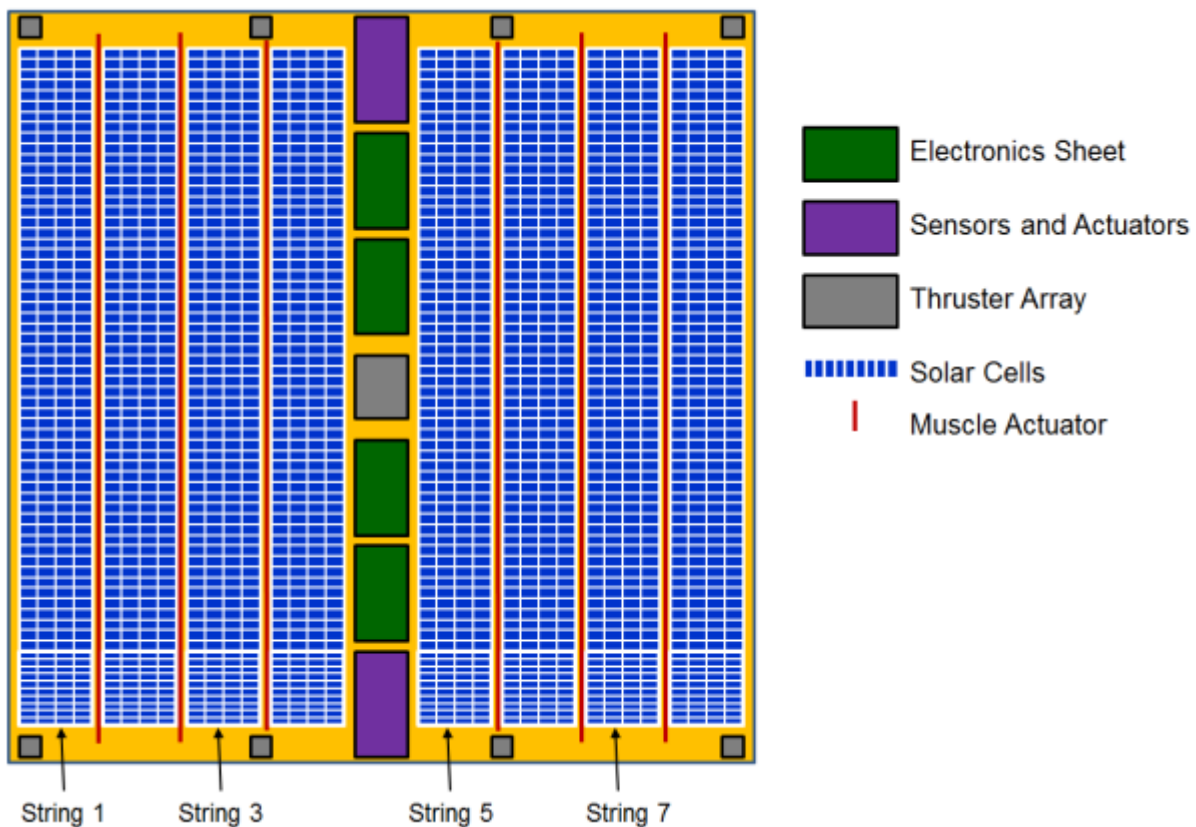


Figure 40. Schematic view of a flat Brane Craft surface. The 1 square meter Kapton® structural sheet is shown in gold, and various system sheets are bonded to it. The 8 solar cell strings are 95 cm high and 11 cm wide, and the high voltage section occupies the top 85 cm of each string. Six vertical muscle actuators are shown, and seven horizontal actuators are hidden behind the solar cells and other spacecraft systems. Thruster modules are shown oversize in gray, with the

primary 2 x 2 cm thruster module in the middle of the Brane Craft. Smaller, 1 cm x 1 cm attitude control thruster arrays are located near each corner of the Brane Craft, with two more added along the top and bottom edges to provide equal spacing between thruster modules in the horizontal direction. Spacecraft electronics are on four sheets, two above the thruster module and two below, aligned with the vertical centerline of the Brane Craft. A sensors and actuators sheet is mounted near the top edge, and near the bottom edge, again centered on the vertical Brane Craft centerline.

### Findings for 4.2 Solar Array Design:

1. Thin film CIGS solar cells provide the thinnest solar arrays.
2. CIGS solar cells can withstand 10 megrads TID without a cover glass.
3. The direct-drive approach for generating 1,200 V for the thrusters is possible, but requires 2,200 individual cells per string.
4. Bypass diodes, and extra switching transistors, enable solar string operation with many shorted and open cells.

### 4.3 Thin Film Electronics

Modern electronics depends on how currents flow in semiconductors under the response of electric fields created by different potentials applied to electrodes in contact with the semiconductor. Figure 41 shows a cross section of an n-type Metal Oxide Semiconductor (MOS) transistor, the basis of most modern electronics. Current can flow between the source and drain electrodes, separated by the gate width  $L$ , if the source potential is more positive than the drain. The gate electrode acts as a valve; current flows from source to drain only if the gate is at or less positive than the source, and the drain is even lower in potential. This is analogous to water flow over the top of a dam down to a river below as controlled by a variable-height gate at the top of the dam. The gate insulator is typically 10 nanometers or more in thickness, while the gate length  $L$  can range from tens of nanometers to tens of microns. The minimum feature size that can be produced by a given semiconductor fabrication process determines the minimum length  $L$  in a transistor. This sets current-voltage characteristics and switching time. The distance out of the page, called the gate width, determines current-carrying capability.

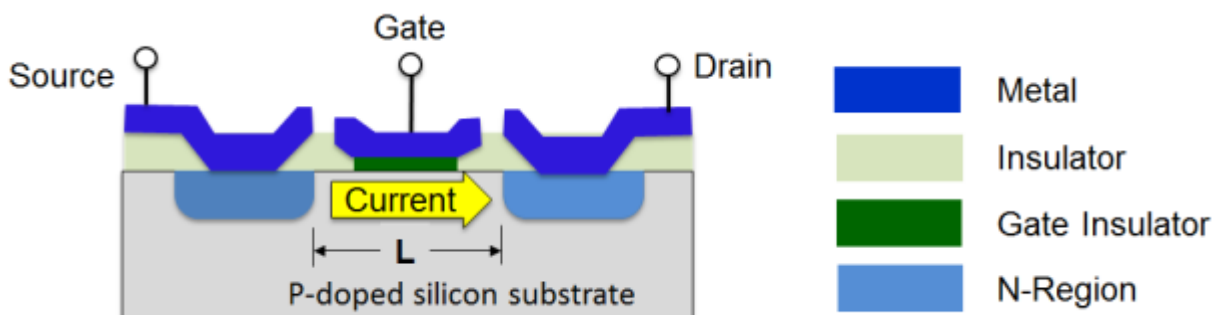


Figure 41. Cross-sectional view of an n-MOS transistor. This schematic shows source, drain and gate electrodes deposited on top of a dielectric, or insulator, that covers the top surface of a

*P-doped silicon substrate. The source electrode is on the left, the gate in the middle, and the drain on the right. The electrodes do not touch each other, and the dielectric layer below the gate is much thinner than the dielectrics under the source and drain electrodes. Regions below the source and drain electrodes have been heavily doped to be N-type. Current can flow between the source and drain electrodes, separated by the gate width  $L$ , if the source potential is more positive than the drain. The gate electrode acts as a valve; current flows from source to drain only if the gate is at or less positive than the source, and the drain is even lower in potential.*

Thin film transistors (TFTs) are a key enabler of Brane Craft electronics. TFT arrays were developed primarily for flat panel display applications with size ranging from about 1 cm (eyepiece displays used in digital cameras) to over 3 meters (110” televisions). Fabrication of mass-market displays occurs primarily in South Korea, China, Taiwan, and Japan. Table 4 shows generation number, year of introduction, and size of the glass panels used to manufacture flat panel displays. Note that current generation fabrication creates multiple displays (6 to greater than 30) on pieces on glass with an area of about 9 square meters. Next generation (Gen 11) fabrication centers, or foundries, cost about \$7 billion USD and are expected to process 90,000 multi-display panels per month.<sup>17</sup> Fortunately, this level of investment is not required for 1 square meter and smaller Brane Craft; used equipment from circa 2002 would be adequate.

*Table 4. LCD display panel size and year of introduction for different generations. Data from reference 18.*

Generation	Year	Glass Panel Size (meters)
2	1987	0.27 x 0.36
3	1994	0.36 x 0.465
4	1997	0.55 x 0.65
5	2000	0.68 x 0.88
6	2002	1.1 x 1.25
7	2004	1.5 x 1.8
8	2005	1.87 x 2.20
9	2006	2.16 x 2.46
10	2009	2.85 x 3.05
11	2019	2.94 x 3.37

Figure 42 shows a schematic cross section through a modern Liquid Crystal Display (LCD) with white light coming from the bottom and the viewer looking down from the top. White light is generated by a cold cathode fluorescent tubes or Light Emitting Diodes (LEDs). The main structural elements are glass panels, typically a half to few millimeters thick, separated by about 10 microns, with a liquid crystal material filling the gap. Note the similarity of this basic design with that of a Brane Craft. The bottom and top polarizers are cross-polarized, so in the off state, no light gets through the display. With an electric field applied between the glass plates, the liquid crystal molecules rotate smoothly from one orientation to another, and the light polarization follows this rotation. The field is applied using a potential difference between optically transparent ITO layers; one uniformly covers the bottom surface of the top glass panel, while the other covers

the top surface of the bottom panel immediately under a colored sub-pixel. When the TFT is fully “on”, the polarization vector of the light transiting the liquid crystal from bottom to top rotates by 90°, and light that gets through the color filter easily passes through the top polarizer. A user would see a blue dot at this location. Most displays are color displays, so at least three different color subpixels combine to form a single image pixel.

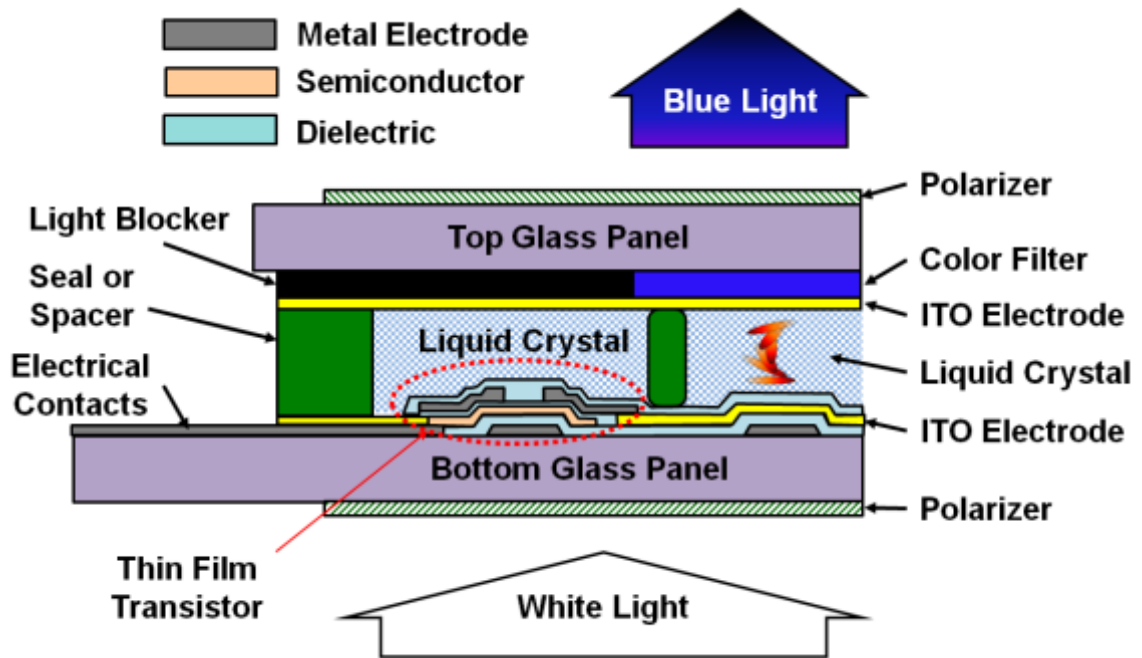


Figure 42. Schematic cross section of a blue pixel of a current-generation LCD panel display. This cross section shows a top and bottom glass panel with a polarizer layer on top of the top panel, and one on the bottom of the bottom panel. The bottom surface of the top glass panel has an opaque layer above the switching transistor deposited on the top surface of the bottom glass layer, and a blue filter layer above a transparent indium tin oxide conductor deposited on the top surface of the bottom layer. The potential of this electrode is controlled by the adjacent transistor. There is a final indium tin oxide layer deposited on the bottom surfaces of the opaque and blue filters. A liquid crystal fills the region above the bottom glass sheet with deposited transistors and transparent electrode, and below the indium tin oxide layer on the bottom of the top glass sheet. White light flows upward from the bottom, and the polarizers on the top and bottom surface are cross-polarized. Blue light that gets through the blue filter gets stopped by the top polarizer. If an appropriate potential is put on the bottom indium tin oxide electrode by the transistor, the polarization of white light going upwards will be rotated, and the blue component that gets through the blue filter will also get through the top polarizer layer. An observer would see a blue dot. Red, green, and sometimes yellow filters are used in neighboring pixels to generate a full color pixel. This drawing is not to scale.

A modern 4K UHD television or monitor has at least 3,840 x 2,160 pixels, three color subpixels per pixel, and at least one TFT per pixel to control them; 24.9 million transistors deposited on a

glass surface. These TFTs are fairly slow compared to conventional silicon nanoelectronics; the required switching speed for a 120 Hz UHD display is only 400 kHz while transistors manufactured on single crystal silicon substrates can easily exceed 4 GHz. Brane Craft need a minimum transistor switching speed of about 10 MHz.

Table 5 shows basic properties of Intel microprocessors released between 1971 and 1993 that were manufactured using a Complementary Metal Oxide Semiconductor (CMOS) processes on single crystal silicon substrates. The process column shows the minimum feature size in microns, the MIPS column is processor speed in Millions of Instructions per Second, and the right most column shows average single transistor area in terms of Square Process Units (SPUs). This number is derived by dividing the die area in square mm by the transistor count, multiplying by 1 million to covert to square microns per transistor, and finally dividing by the square of the process size in microns. Moore’s Law, the exponential increase in data processing capability over time, is primarily driven by the decrease in minimum feature size over time, and the increasing density of transistors. Smaller transistors are typically faster. Unofficially, there is also Moore’s Second Law, the increase in manufacturing facility cost over time. Current state-of-the-art processors use 0.014 micron processes, can operate at 318,000 MIPS, have 3.4 billion transistors, and are manufactured in \$5 billion foundries. Fortunately, we don’t need this level of performance for most Brane Craft systems, and can use much larger thin film transistors fabricated in cheaper foundries.

*Table 5. Basic properties of Intel microprocessors released between 1971 and 1993.*

Processor	Transistor Count	Year of Intro	Process (microns)	Die Area (sq. mm)	Clock Speed (MHz)	Data Bits	MIPS	Transistor Area (SPUs)
4004	2,300	1971	10	12	0.74	4	0.092	52.17
8008	3,500	1972	10	14	0.5	8	0.05	40.00
8080	4,500	1974	6	20	2	8	0.29	123.46
8085	6,500	1976	3	20	3	8	0.37	341.88
8086	29,000	1978	3	33	5	16	0.33	126.44
8088	29,000	1979	3	33	5	16	0.38	126.44
80186	55,000	1982	3	60	6	16	0.9	121.21
80286	134,000	1982	1.5	49	6	16	0.9	162.52
80386	275,000	1985	1.5	104	12	32	1.56	168.08
80486	1,180,235	1989	1	173	20	32	25	146.58
Pentium	3,100,000	1993	0.8	294	60	32	100	148.19

The AeroCube CubeSats use multiple microcontrollers, currently operating at 10 to 32 MHz clock speeds, with processing speeds of 2.5 to 8 MIPS. The higher speeds are required for attitude determination and control loops that operate at 5 Hz, and for high speed communications at several hundred kilobits/s. A 1 MIPS processing speed would work for 1-Hz attitude control loops and data rates below 50 kilobits/s. A 1 MIPS processing speed was originally provided by early 1980’s silicon-based CMOS microprocessors with 6 MHz to 12 MHz clock rates, 1.5 to 3 micron

minimum feature size, and a few hundred thousand transistors. Can microprocessors with similar processing speed be fabricated using thin film transistors?

The TFTS in current generation flat panel displays are an order-of-magnitude too slow (~400 kHz vs. 6 MHz). They are typically fabricated using hydrogenated amorphous silicon (a-Si:H), and have gate lengths of about 30 microns. Speed can be significantly increased by changing the semiconductor material and by shrinking transistor size. The maximum switching frequency  $f_{max}$  of a thin film transistor is given by:

$$f_{max} = \mu * V / L^2 \quad (5)$$

where  $\mu$  is the carrier mobility,  $V$  is the switching voltage, and  $L$  is the gate length; the distance between the source and drain gates of a field-effect transistor. Carrier mobility of a-Si:H in flat panel displays is about  $0.6 \text{ cm}^2 / \text{V-s}$ ; about 300 times worse than the hole mobility in single crystal silicon. Due to the maximum 10 megarad TID expected for almost unprotected thin film electronics over one month in low Earth orbit, I originally chose ZnO as the semiconductor. Sputtered thin film ZnO layers have shown carrier mobilities in excess of  $50 \text{ cm}^2 / \text{V-s}$ .<sup>19</sup> Thin film carbon nanotube transistors can also provide tens of megarad total dose tolerance with high mobility. Researchers at Lockheed Martin Space Systems Company, and The Aerospace Corporation, demonstrated CNT transistor operation to 21 megarads.<sup>20</sup> Inkjet-printed CNT transistors on flexible substrates have demonstrated carrier mobilities up to  $9.8 \text{ cm}^2 / \text{V-s}$ .<sup>21</sup> Both CNT and ZnO transistors will be required to create p-type and n-type transistors for conventional CMOS circuits. Figure 43 shows calculated cutoff frequencies as a function of gate length for a-Si:H with a  $0.6 \text{ cm}^2 / \text{V-s}$  mobility and the proposed ZnO or CNT transistors with a degraded mobility of  $5 \text{ cm}^2 / \text{V-s}$ .

Figure 43 shows that ZnO and inkjet-printed CNT transistors can operate at frequencies in excess of 30 MHz with a gate length of 10 microns or less. Features of this size (10 microns) can be lithographically patterned using relatively inexpensive photomasks, or direct-printed using high-resolution inkjet technology. They can be fabricated on flexible substrates, or fabricated on a rigid substrate with a flexible layer as the top most layer, and a sacrificial layer between the electronics and rigid substrate that gets dissolved at the last step. ZnO TFTs have been fabricated on 5-micron thick polyimide using this process.<sup>22</sup>

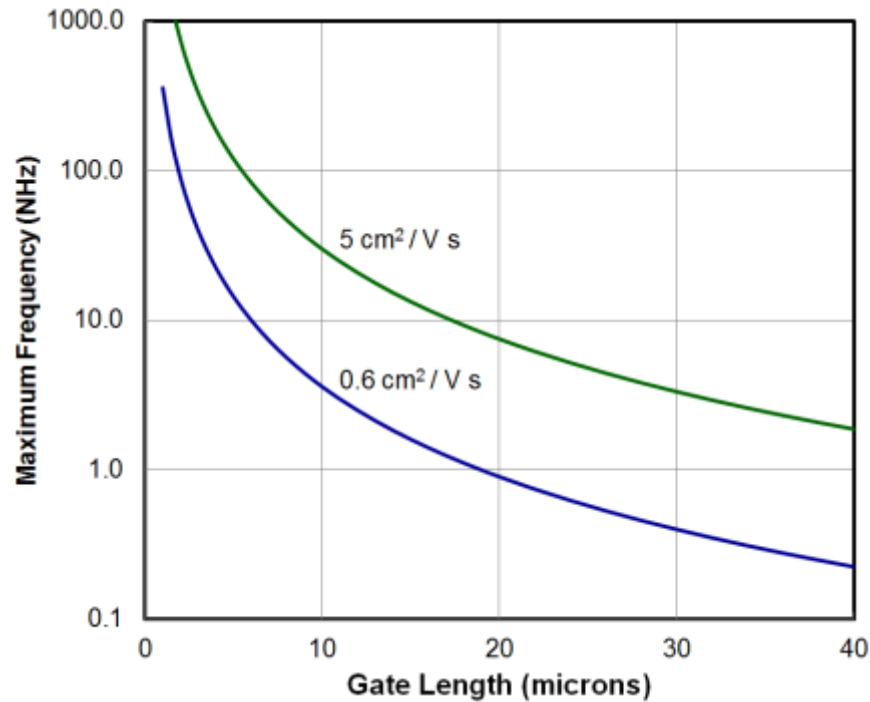


Figure 43. Maximum speed of thin film transistors as a function of gate length for hydrogenated amorphous silicon (lower curve), and ZnO or CNT semiconductors (upper curve) and a 6 V cutoff voltage. The vertical axis is maximum frequency in megahertz, and ranges logarithmically from 0.1 MHz at the bottom to 1000 MHz at the top. The horizontal scale is gate length in microns, ranging linearly from 0 on the left to 40 microns on the right. The curve representative of amorphous silicon, with a mobility of  $0.6 \text{ cm}^2/\text{V}\cdot\text{s}$ , starts a 300 MHz at 1-micron gate length, drops to 0.9 MHz at a 20-micron gate length, and ends at 0.2 MHz at a 40-micron gate length. The curve representative of printed carbon nanotube transistors, with a mobility of  $5 \text{ cm}^2/\text{V}\cdot\text{s}$ , starts a 1000 MHz at 2-micron gate length, drops to 30 MHz at a 10-micron gate length, and ends at 2 MHz at a 40-micron gate length.

How much area will be required for a nominal 500,000 transistor thin film processor fabricated using a 10-micron process? This would be an 8 MIPS processor somewhere between an Intel 80386 and 80486 processor. Based on an averaged transistor area of 150 Square Process Units for 80386 and 80486 processors from Table 5, a 500,000 transistor microprocessor would require an area of  $75 \text{ cm}^2$  if fabricated using a 10-micron process; about 3" by 4". This seems large, but over 130 could be deposited on one side of a 1 square meter Brane Craft. Six processors could be deposited on each side using only 5% of the total  $1 \text{ m}^2$  surface area. Processor dimensions could be cut in half by going to a 5-micron process.

Fabrication of conventional transistors and TFTs is typically done using a subtractive process:

- an individual layer of a dielectric, conductor, or semiconductor is deposited on a substrate using vacuum or liquid deposition,
- the deposited layer is covered by a thin layer of photoresist,
- the photoresist is hardened by heating in a vacuum,

- the entire substrate is exposed to ultraviolet light through a photomask,
- the photoresist is exposed to a liquid developer that removes photoresist over the unwanted regions,
- the exposed regions are removed using selective plasma or liquid etching,
- the remaining photoresist is dissolved and removed, and
- the surface is cleaned for the next layer.

Note that there are eight steps for every layer, and these steps may require liquid or vacuum processing. The advantage of this approach is that it doesn't care how many devices are fabricated on a substrate, as long as the photolithographic resolution and layer thicknesses are suitable for creating functioning devices; fabrication speed is independent of design complexity for a given number of layers. The disadvantages of this approach are that photomasks must be generated, multiple processing stations, e.g., thermal evaporators, sputtering chambers, photo exposure chambers, etc., are required, and the substrate must be transferred to all of these stations in a clean environment. Photomasks come in a variety of sizes, and inexpensive 5-micron resolution photomasks are readily available at sizes up to 10" square.

Additive manufacturing of electronics is relatively new. In this case, an industrial inkjet printer deposits a patterned 2-dimensional layer of conductor, semiconductor, or dielectric on a rigid or flexible substrate in aqueous form that dries into a solid structure.<sup>23</sup> This approach has been used to fabricate CNT transistor circuits using a solution of semiconducting single wall CNTs. These solutions are typically >98% semiconducting, and are fairly expensive at ~\$500/milligram in solution due to the extra processing steps required to remove the 33% of metallic CNTs that result from typical arc-discharge CNT fabrication. Another additive process is screen printing. This has been used to make flexible, active-matrix electrochromic displays with CNT TFTs.<sup>24</sup>

These should be the least inexpensive methods for manufacturing radiation-hard, thin film electronics for Brane Craft in thousand-unit quantities. The majority of industrial inkjet systems have resolutions of less than 1600 dots per inch, resulting in minimum feature sizes of 16 microns and larger. This is borderline for printing 8-MHz processors. However, at least one system has been identified that can produce 5-micron minimum features, on a 30 cm x 30cm substrate.<sup>25</sup> In any case, limiting substrate dimensions to 12 inches or smaller will significantly reduce development and production costs.

### **Findings for 4.3 Electronics:**

- 1. Carbon nanotube, and ZnO thin film transistors can provide enough radiation tolerance for a Brane Craft to last a month or more anywhere in LEO.**
- 2. Carbon nanotube thin film transistors can be used to fabricate an 8 MIPS microprocessor using inexpensive 10-micron minimum feature size using inkjet printing or photolithography techniques.**
- 3. The 8 MIPS processor using 10-micron minimum feature size requires an area of 75 cm<sup>2</sup>.**

4. With ~40 potential penetrating impacts per month for a 1 m<sup>2</sup> Brane Craft, there is a 30% probability of hitting a 10-micron-based microprocessor over a one month mission.
5. Reducing the minimum feature size to 5 microns would quadruple speed and reduce the probability of failure due to particle penetration by 4 X.
6. With ~40 potential penetrating impacts per month for a 1 m<sup>2</sup> Brane Craft, there is a 7.5% probability of hitting a 5-micron-based microprocessor over a one month mission.

#### 4.4 Thruster System

NASA's Space Technology Mission Directorate (STMD) funded development of micro-electrospray thrusters at MIT, NASA-JPL, and Busek Co., Inc. under the Game Changing Development Program.<sup>26</sup> Electrospray thrusters use applied electric fields on the order of 1 V/nm to electrostatically pull a conducting liquid into a "Taylor Cone" with a ~3-nm radius sharp tip at the apex. This sharp tip further amplifies the applied electric field by about an order-of-magnitude, thus generating ~10 V/nm fields that directly field ionize the liquid molecules. This ionization process is extremely efficient and can yield ion currents of 500 nA or more per tip. Thrust is between 6 and 20 nanonewtons per tip for specific impulse ( $I_{sp}$ ) between 2000 and 5000 s. Overall thrust scales as the number of active tips.

It's important to realize that ion current per tip, which is proportional to thrust, is independent of overall Taylor cone size. It should therefore be possible to create nano-electrospray thrusters with smaller Taylor cones and significantly reduced overall dimensions. Recent molecular dynamics simulations of electrospray thrusters performed at Penn State showed Taylor cone formation with 500 nA ion currents using base diameters as small as 12 nm with tip base-to-extractor distances of less than 0.07 microns.<sup>27</sup> These simulations used the ionic liquid EMIM-BF<sub>4</sub> flowing out of platinum capillaries. Nano-electrospray thruster arrays can be thin film structures a few microns thick, and a few millimeters or less in lateral dimension. With a thrust of about 13 nanonewtons per tip at 4000-s  $I_{sp}$ , an 8 mm x 8 mm array with 10-micron lateral spacing between tips could generate 8.2 millinewtons of thrust using 630 thousand emitters. Input power is 180 W.

Micro-electrospray thrusters are still under development, and their current operating lifetime is between 10 and 100 hours. More development is needed, but this is already being funded by NASA. For this study, I focused on the propellant storage issues. The dielectric strength of 25-micron thick Kapton<sup>®</sup> is 303 kV/mm, yielding an estimated breakdown voltage of 2.1 kV and 3.8 kV for 7-micron and 12.5-micron thick Kapton<sup>®</sup> sheets, respectively.<sup>28</sup> Using the thicker Kapton<sup>®</sup> for the main structural sheets would give improved breakdown voltage margin, and further reduce the number of particle penetrations into the propellant chamber. Effective Kapton<sup>®</sup> thickness increases to 49 microns, and wet mass increases to 96 grams.

Particle penetration into the propellant storage layer is not a problem for propellant storage since the vapor pressure of the ionic liquid propellants is essentially zero, and capillary action should

hold the propellant in for 10-micron scale holes. The more serious concern is shorting a grounded spacecraft outer layer with a propellant that can be at +1,200 or -1,200 Volts; propellant potentials when a thruster is operating. Ionic liquids are conductive, and the storage areas should be electrically isolated from the immediate propellant next to a thruster. The spacers in Figure 33 provide this electrical isolation. A Brane Craft still needs a way to transfer propellant between storage regions and thruster regions. Providing propellant transfer capability and kilovolt electrical standoff is an issue that still needs to be addressed. Potential solutions include isolation valves based on localized freezing, since a solid ionic liquid is non-conducting and the isolation is only needed while thrusting, and bubble-based droplet ejectors used in some inkjet printers.

#### **Findings for 4.4 Thruster System:**

- 1. An 8 mm x 8 mm array of nano-electrospray thrusters can provide primary thrusting for a Brane Craft.**
- 2. The square meter structural sheets that form the propellant tank should be 12.5 microns thick, or more, to provide sufficient dielectric breakdown strength for 1,200 V thruster operation.**
- 3. Electrical isolation of propellant storage regions from thruster regions still needs to be addressed.**

#### **4.5 Sensors**

A number of simple sensors can be fabricated as thin film structures. The first is the strain sensor. This device is composed of a thin conductive trace that meanders back and forth to fit a much longer length onto a shorter footprint. Trace length along one direction should be much longer than the trace length perpendicular to that direction. If the substrate is stretched along the long direction, the resistance will change. Figure 44 shows the basic layout and Wheatstone bridge readout circuit used to monitor strain in the horizontal direction. All resistances should be equal in the unstrained state, and the potential difference, or  $V_{measured}$  would be zero. If the substrate is strained,  $V_{measured}$  will be positive or negative, and proportional to the strain. Typically, three sensors with their long axes tilted by  $60^\circ$  to each other are used to determine orthogonal X and Y strains in the plane of the sensor. Commercial strain sensors are small Kapton<sup>®</sup> or plastic sheets with an adhesive layer on one side so that they can be physically bonded to the structure to be monitored. In our case, the Kapton<sup>®</sup> is the structure to be monitored. Twenty or more sensors deposited on the structural sheets can be used to monitor local strain and determine local and overall spacecraft curvature. Due to their simplicity and lack of semiconductors or critical dielectrics, these sensors should be very radiation-hard. The electronics to process the voltages will, however, need to be radiation hard to many megarads.

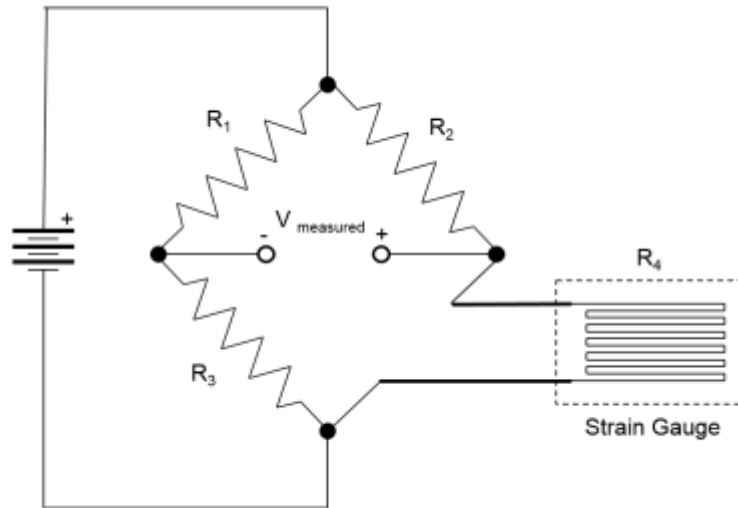


Figure 44. Circuit diagram of a single-axis strain sensor and Wheatstone bridge readout circuit. Three resistors,  $R_1$ ,  $R_2$ , and  $R_3$ , are connected in series along three sides of a square. The fourth side, the strain gauge, is connected across the remaining side. All four resistors form a square loop. The connected resistors in this loop are  $R_1$ ,  $R_2$ ,  $R_4$  (strain gauge), and  $R_3$ , going clockwise. The positive side of a voltage source is connected to the  $R_1$ - $R_2$  junction, and to the  $R_3$ - $R_4$  junction. Voltage,  $V_{measured}$ , is measured across the other two connections; between  $R_1$  and  $R_3$ , and between  $R_2$  and  $R_4$ . The strain gauge consists of a long meandering trace running mostly horizontally. If the strain gauge ( $R_4$ ) is strained in the horizontal direction, its resistance will change and  $V_{measured}$  will be positive or negative, depending whether the strain is tensile or compressive.

Another useful, simple sensor is a giant magnetoresistive sensor for measuring magnetic field magnitude in a particular direction. We fly commercial versions, which typically include three orthogonal axes, amplifiers, and digital output in an integrated circuit, in our CubeSats in LEO. These sensors use two  $\sim 10$ -nm thin layers of ferromagnetic material separated by a  $\sim 5$ -nm thick non-magnetic conducting layer like copper or aluminum.<sup>29</sup> This sandwich is usually deposited as a narrow rectangle as seen from above the substrate. The resistance across the long axis of the stack can be altered by changing whether the moments of the ferromagnetic layers are parallel or antiparallel; antiparallel layers increase resistance. A low current ( $\sim$ a few mA per micron of width), flowing along the long dimension puts the magnetic domains in the ferromagnetic layers in an antiparallel configuration. An external magnetic field can make them parallel, thus changing the resistance. These sensors typically have a range of 0.001 to 10 Oersteds that is well suited to measuring the Earth's magnetic field in LEO. Again, due to their simplicity and lack of semiconductors or critical dielectrics, these sensors should be very radiation-hard.

An important attitude sensor is a sun sensor shown schematically in Figure 45. For this application,  $\sim 10$  microns of Kapton<sup>®</sup> will separate the aperture plate from the quad detector. Thin Kapton<sup>®</sup> sheets look orange, and are at least 80% transmissive across the 700 nm to 1,100 nm wavelength range. Typical quad cell detectors are single crystal silicon photodiodes, but we'll need a carbon nanotube or CIGS equivalent for the high radiation environment. One group has achieved 1%

conversion of sunlight into DC power using C<sub>60</sub> Buckyballs on 5-nm thick single wall carbon nanotube layers, with 45% external quantum efficiency between 1,000 and 1,100 nm wavelengths.<sup>30</sup> This can work in our application, but no radiation tolerance data exists.

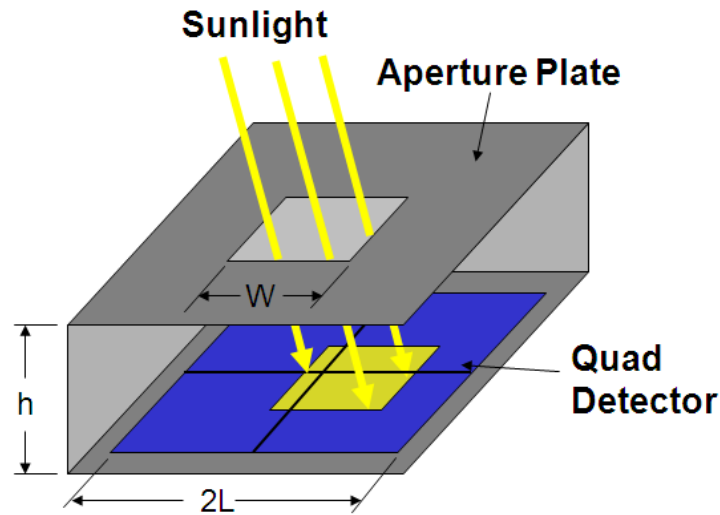


Figure 45. Schematic diagram of a sun sensor. The top of the sun sensor is an opaque sheet with a square hole in the center. The sides of the aperture are of length  $W$ . Four square photodiodes in a  $2 \times 2$  arrangement, called a quad detector, are in a parallel plane a distance  $h$  below the aperture plate. The outer sides of the quad detector are of length  $2L$ , so each detector is  $L \times L$  in size. The normal to the quad detector, starting at the intersection of the four photodiodes, goes through the center of the square hole in the aperture plate. If one were to look down at the detector from above, four equal size detectors squares would be seen. Sunlight is shown coming down from the top at angle to the surface normal of the detector. Sunlight illuminates different size areas of each detector, thus enabling determination of the angle between the incoming sunlight and two orthogonal axes; it enables determination of where the sun is with respect to the detector.

Earth sensors are another useful attitude determination sensor. They typically use thermal infrared detectors; the Earth is a warm ball at roughly 300 K while space is at 3 K. Microbolometers have become the detector of choice since they don't have to be cooled, and can be made in arrays for thermal imaging. Typical devices use a window or focusing lens to transmit thermal radiation between 5 and 14 microns in wavelength. Kapton<sup>®</sup> absorbs at those wavelengths, so an open hole would be the best geometry. Multiple detectors distributed across the surface, combined with surface warping, could locate the direction of the center of the Earth. Microbolometer detectors using single wall carbon nanotube networks have shown responsivities of up to 250 V/W.<sup>31</sup> Typical thermal radiation fluxes in LEO are about 200 W/m<sup>2</sup>, so the thermal radiation getting through a 40-micron diameter hole in a 10-micron thick layer of Kapton<sup>®</sup> is 0.25 mW, and the output response would be ~60  $\mu$ V. This can be amplified to Volt output levels.

## Findings for 4.5 Sensors:

1. **Strain gauges can be readily used in a Brane Craft to determine local and overall curvature.**
2. **Giant magnetostrictive sensors can be used to measure magnetic field strengths within the plane of the Brane Craft.**
3. **Sun sensors can be built, but we need to know the radiation tolerance of carbon nanotube photodiodes.**
4. **Earth sensors can be built, but radiation tolerance data for carbon nanotube microbolometers are needed.**

## 4.6 Actuators

Brane Craft will control their attitude through a combination of distributed thrusters and magnetic torque coils. Reaction wheels won't work in these ultra-thin spacecraft. The moment of inertia of an 81-gram mass, 1-square meter Brane Craft about a rotation axis that goes from the middle of one 1-meter side to the middle of the opposite side is  $6.8 \times 10^{-3} \text{ kg-m}^2$ . A 0.1-mN thruster firing perpendicular to the surface 0.48 meters from the rotation axis will generate a torque of  $4.8 \times 10^{-5} \text{ N-m}$ , and an angular acceleration of  $0.12 \text{ radians/s}^2$  while using 2.2 W of power. This would enable a  $90^\circ$  rotation, stopping at  $90^\circ$ , in only 3.7 s. An unloaded Brane Craft can be extremely agile. Flat magnetic torque coils could be added, but they would consume more power to generate equivalent rotational accelerations, and they can't generate torque about the local magnetic field line.

Shape control is a key feature of Brane Craft, and a number of potential actuator concepts are available. The simplest actuator is a capacitor with a flexible dielectric. Application of a potential difference, typically hundreds to thousands of volts, causes the capacitor plates to attract and compress the dielectric. The dielectric expands in the plane parallel to the electrodes, generating an expansion force that can put an attached structure into tension. The advantage of this approach is that no liquids are involved, the structure does not have to be sealed, and it won't freeze if the Brane Craft gets too cold. The disadvantages are that high voltages are required, and the deformations are small.

Ionic polymer-metal composites are another approach.<sup>32</sup> In this actuator, a sheet of ion exchange polymer such as Nafion is coated with metallic electrodes, and the interior filled with water plus a salt. When a potential is applied between the electrodes, anions head toward one electrode and cations head towards the other. If the cations, e.g.,  $\text{Na}(\text{H}_2\text{O})_4^+$ , are bigger, the region near the negative electrode swells, and the entire sheet bends with the negative electrode convex outward. These devices actuate at a few Volts, but they require liquid containment and can't tolerate high-velocity particle-induced leaks. A filled actuator can also freeze when the Brane Craft enters eclipse (next section). The liquid must be contained or the actuator will not work.

### Findings for 4.6 Actuators:

1. **Distributed thrusters can easily provide attitude control for a Brane Craft.**
2. **Dielectric-based mechanical actuators for shape control are simple and robust, but they require high actuating voltages.**
3. **Electroactive polymers, and ionic polymer-metal composites in particular, generate larger mechanical deformations using a few Volts.**
4. **More work needs to be done on shape-changing actuators.**

### 4.7 Thermal Control

Brane Craft are two-dimensional spacecraft with almost no thermal mass. They will cool down rapidly after entering eclipse, to settle at a temperature primarily determined by the absorptivity/emissivity properties of the solar cells. A simulation of overall Brane Craft temperature was run using a 1350 W solar flux, a 200 W thermal flux from the Earth, a Kapton<sup>®</sup> specific heat of 1.09 J-gram/K, an EMIM-BF<sub>4</sub> (1-Ethyl-3-methylimidazolium tetrafluoroborate, the conventional ionic liquid propellant) specific heat of 1.9 J-gram/K, an absorptivity of 0.8, and an emissivity of 0.8. This simulation used the current Brane Craft structural mass of 54 grams, plus a full load of 27 grams of propellant. The simulation, shown in Figure 46, starts with the Brane Craft normal vector pointing at the sun for maximum power and heating, and then turning towards the Earth as it enters eclipse at  $T = 29$  seconds, again for maximum heating. The equilibrium temperature is 342 K (+69° C) while in sunlight, and drops to 205 K (-67° C) while in eclipse. Most of the cool-down occurs over 2 minutes. The high temperature is acceptable, but the low temperature will freeze EMIM-BF<sub>4</sub> ionic liquid propellant. Its freezing point is 298 K; 15° C. This simulation did not include the heat of fusion of the propellant to show a representative cool-down time constant for a non-freezing propellant.

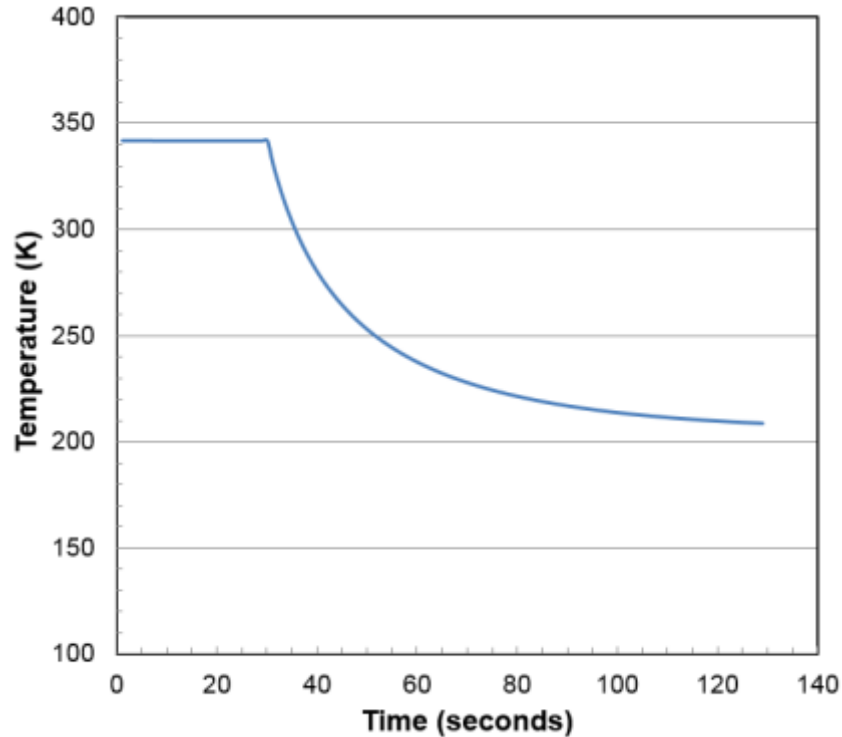


Figure 46. Temperature vs. time for a Brane Craft initially in full sunlight, and flying into eclipse at  $T=29$  seconds. The vertical scale is temperature in degrees Kelvin, and is linear from 100 K at the bottom to 400 K at the top. The horizontal scale is time in seconds, and is linear from 0 seconds on the left to 140 seconds on the right. The temperature starts at 342 K at  $T=0$  seconds and is flat to  $T=29$  seconds. At this point it drops rapidly to 250 K at  $T=51$  seconds, and slowly approaches the eclipse equilibrium value of 205 K after a few minutes. The  $1/e$  time constant is 20 seconds.

Ionic liquid propellants were surveyed to find any that would not freeze at  $-67^{\circ}\text{C}$  and have molecular weights (cation and anion) that were similar to the EMIM-BF<sub>4</sub> values (molecular weight of 198), or lower. Heavier anions or cations would increase the required propellant voltage to achieve a 4000 s specific impulse, thus increasing the likelihood of dielectric breakdown. The ionic liquid 1-butyl-1-methylpyrrolidinium dicyanamide is a potential candidate with a melting point of  $-90^{\circ}\text{C}$ , and a molecular weight of 208. Other approach is to use eutectic mixtures of ionic liquids to induce freezing point depression.

#### Findings for 4.7 Thermal Control:

1. A Brane Craft will cool rapidly upon entering eclipse, reaching temperatures below  $-60^{\circ}\text{C}$  for typical absorptivity/emissivity ratios for solar-cell covered spacecraft.
2. This cooldown has a time constant of  $\sim 20$  seconds.
3. To prevent propellant freezing, a new ionic liquid propellant with a freezing point below  $-70^{\circ}\text{C}$  is needed.

**4. 1-butyl-1-methylpyrrolidinium dicyanamide is a potential non-freezing propellant with a molecular weight similar to the more conventional EMIM-BF4 ionic liquid propellant.**

## **5. Technology Roadmap**

This work first focused on mission analysis, which generated potential debris deorbit mission timelines and maximum masses that can be taken down from higher LEO orbits. It then included significant effort on environmental influences such as radiation, particle impacts, and thermal issues. Finally, it looked at various spacecraft systems to see if they were possible within the physical confines of a membrane spacecraft in a harsh environment.

**This radical spacecraft design looks possible, but still has many remaining issues:**

1. Can high-speed, flexible, thin-film electronics that can handle 10 megarad TID be manufactured at reasonable cost within the next decade?
2. Can sensor materials like photodiodes be made TID-tolerant to 10 megarad levels?
3. Can a “bullet-proof” spacecraft design be created where the bullets are high-speed micro-projectiles that generate ~50 through holes per month?
4. Can electroactive polymers or other “muscle” mechanisms provide required tensions and compressions to curl and control a Brane Craft?
5. Can communications systems be fabricated as thin-film systems? The basic electronics look possible, but some communications-system unique components such as crystal oscillators aren’t amenable to thin-film design.
6. Can the overall design be scaled to arbitrary size (smaller and bigger)?

The next steps should be to fabricate simple digital and analog electronics, solar cell strings, shape and attitude sensors, and shape-change actuators using radiation-tolerant and penetration-tolerant designs and materials. They should be functionally tested, and subjected to increasing levels of radiation exposure up to 10 megarads. In addition, the communications system should be fully analyzed to see if there are any show-stoppers such as lack of stable frequency sources that can be fabricated using thin film processes.

## **References**

- 
1. Thompson, Roger, “A Space Debris Primer,” *Crosslink* (ISSN 1527-5264), The Aerospace Corporation, pp. 4-7, Fall 2015.
  2. National Aeronautics and Space Administration, “Orbital Debris Quarterly News,” **18**, #1, p. 10, January 2014.

- 
3. Hansen, B., Starchville, T., and Hoots, F., "First Responders in Space: The Debris Analysis Response Team," *Crosslink* (ISSN 1527-5264), The Aerospace Corporation, pp. 14-21, Fall 2015.
  4. Ailor, W., Chobotov, V., Peterson, G., and Patera, R., "Small Satellites: Space Debris and Reentry Hazards," Chapter 22 in **Small Satellites: Past, Present, and Future**, pp. 729-769, The Aerospace Press and the AIAA, Reston, Virginia, 2008.
  5. Wikipedia, "2016 in Space Flight," URL: [https://en.wikipedia.org/wiki/2016\\_in\\_spaceflight](https://en.wikipedia.org/wiki/2016_in_spaceflight)
  6. T.N. Edelbaum, "Propulsion Requirements for Controllable Satellites," *ARS Journal*, p.1079-1089, August 1961.
  7. Janson, S.W., "Electric Propulsion for Low Earth Orbit Constellation Morphing," AIAA Paper 2002-3669, 38th AIAA/ASME/SAE/ASEE Joint Propulsion Conference, July 7-10, 2002.
  8. SPENVIS web page, European Space Agency, URL: <https://www.spervis.oma.be/>
  9. NIST ESTAR web page, National Institute of Standards and Technology, URL: <http://physics.nist.gov/PhysRefData/Star/Text/ESTAR.html>
  10. NIST PSTAR web page, National Institute of Standards and Technology, URL: <http://www.physics.nist.gov/PhysRefData/Star/Text/PSTAR.html>
  11. The Grün Interplanetary Flux Model web page, URL: <https://www.spervis.oma.be/help/background/metdeb/metdeb.html#METFLUX>
  12. Divine, N. and Gruen, R., "Modeling the Meteoroid Distributions in Interplanetary Space and Near-Earth," Proceedings of the First European Conference on Space Debris, Darmstadt, Germany, April, 1993.
  13. Neish, Michael J., and Kiebe, Seishiro, "Hypervelocity Impact Damage for Kapton® Multi-Layered Insulation and Teflon Second-Surface Mirrors," Proceedings of the Third European Conference on Space Debris, Darmstadt, Germany. 19 - 21 March 2001.
  14. NASA Preferred Reliability Practices, "Micrometeoroid Protection," practice number PD-EC-1107, May 1996, URL: [http://www.klabs.org/DEI/References/design\\_guidelines/environment\\_series/1107.pdf](http://www.klabs.org/DEI/References/design_guidelines/environment_series/1107.pdf)
  15. Fraunhofer Institute for Solar Energy Systems, "Photovoltaics Report," Freiburg, Germany, November 2016, URL: <https://www.ise.fraunhofer.de/de/downloads/pdf-files/aktuelles/photovoltaics-report-in-englischer-sprache.pdf>
  16. Pakkala, Asha Kiran, Pattabi, Manjunatha, Sanjeev, Ganesh, Fernandez, A.M., and Mathew, X., "A Study on the Radiation Resistance of CIGS/CdS Thin Film Solar Cell Against 8 MeV Electron," *International Journal of Science Research*, **1**, #4, pp.446-451, 2012.

- 
17. TCL, "TCL Corporation to Toss \$7 Billion to Build Gen 11 LCD and OLED Production Line in Shenzhen," Press Release #2016-09-02, TCL Corporation, Huizhou, China, September 2016, URL: [http://www.tcl.eu/en/newsroom/cl-corporation-to-toss-\\$7-billion-to-build-gen-11-lcd-and-oled-production-line](http://www.tcl.eu/en/newsroom/cl-corporation-to-toss-$7-billion-to-build-gen-11-lcd-and-oled-production-line)
  18. Suzuki, Katsuyoshi, and Suzuki, Naoshi, "Large Gantry Table for the 10th Generation LCD Substrates, NTN Technical Review No. 76, NTN Corporation, Osaka, Japan, 2008, URL: [http://www.ntnglobal.com/en/products/review/pdf/NTN\\_TR76\\_en\\_p134\\_137.pdf](http://www.ntnglobal.com/en/products/review/pdf/NTN_TR76_en_p134_137.pdf)
  19. Brox-Nilsen, C., Jin, J., Luo, Y., Bao, P. and Song, A.M., 2013. Sputtered ZnO Thin-Film Transistors With Carrier Mobility Over 50. *IEEE Transactions on Electron Devices*, 60(10), pp.3424-3429.
  20. Ngo, Quoc X., Anderson, Scott A., O'Connor, Michael J., Nichols, Johnathan A., Dunning, James E., Holihan, Eric C., Taylor, Jerry C., Bushmaker, Adam, Walker, Don, and Mann, Colin J., "Scalable Carbon Nanotube Electronic Devices for Space Nanoelectronics Applications,"
  21. Lee, D. *et al.*, "Logic circuits composed of flexible carbon nanotube thin-film transistor and ultra-thin polymer gate dielectric," *Sci. Rep.* **6**, May 2016.
  22. Li, H. Y. U. and Jackson, T. N., "Oxide semiconductor thin film transistors on thin solution-cast flexible substrates," *IEEE Electron Device Letters*, vol. 36, pp. 35-37, Jan 2015.
  23. Lee, D. *et al.*, "Logic circuits composed of flexible carbon nanotube thin-film transistor and ultra-thin polymer gate dielectric," *Sci. Rep.* **6**, May 2016.
  24. Cao, Xuan, Lau, Christian, Liu, Yihang, Wu, Fanqi, Gui, Hui, Liu, Qingzhou, Ma, Yuqiang, Wan, Haochuan, Amer, Moh. R., and Zhou, Chongwu, "Fully Screen-Printed, Large-Area, and Flexible Active-Matrix Electrochromic Displays Using Carbon Nanotube Thin-Film Transistors," *ACS Nano* **2016** 10 (11), pp. 9816-9822, 2016.
  25. Ceradrop Corporation, "X-Series CeraPrinter Data Sheet," Ceradrop Corporation, Limoges, France, 2016. URL: [http://www.ceradrop.com/content/uploads/2016/04/2-X-SERIE\\_datasheet.pdf](http://www.ceradrop.com/content/uploads/2016/04/2-X-SERIE_datasheet.pdf)
  26. NASA Space Technology Mission Directorate, "Micro-Electrospray Thrusters," 2013. URL: [http://gcd.larc.nasa.gov/wp-content/uploads/2014/01/FS-MEP\\_factsheet\\_130124.pdf](http://gcd.larc.nasa.gov/wp-content/uploads/2014/01/FS-MEP_factsheet_130124.pdf)
  27. Borner, Arnaud; Li, Zeng; and Levin, Deborah A., "Prediction of Fundamental Properties of Ionic Electrospray Thrusters Using Molecular Dynamics," *J. of Physical Chemistry*, **8**, #117, p.p. 6768-6781, 2013.
  28. Dupont, "Summary of Properties for Kapton® Polyimide," Dupont, Inc., URL: <http://www.dupont.com/content/dam/dupont/products-and-services/membranes-and-films/polyimide-films/documents/DEC-KaptonTM-summary-of-properties.pdf>

- 
29. Caruso, Michael J., Bratland, Tamara, Smith, Dr. Carl H., and Schneider, Robert, “A New Perspective on Magnetic Field Sensing,” Honeywell Inc, May, 1998, URL: [https://aerocontent.honeywell.com/aero/common/documents/myaerospacecatalog-documents/Defense\\_Brochures-documents/Magnetic\\_Literature\\_Technical\\_Article-documents/A\\_New\\_Perspective\\_on\\_Magnetic\\_Field\\_Sensing.pdf](https://aerocontent.honeywell.com/aero/common/documents/myaerospacecatalog-documents/Defense_Brochures-documents/Magnetic_Literature_Technical_Article-documents/A_New_Perspective_on_Magnetic_Field_Sensing.pdf)
  30. Shea, Matthew J., and Michael, Arnold S., “1% solar cells derived from Ultrathin Carbon Nanotube Photoabsorbing Films,” Applied Physics letters **102**, p. 243101, 2013.
  31. He, Xiaowei, Léonard, François , and Kono, Junichiro, “Uncooled Carbon Nanotube Photodetectors,” Advanced Optical Materials, 3: 989–1011, 2015.
  32. Shahinpoor, Mohsen, and Kim, Kwang J., “Ionic Polymer-Metal Composites: 1, Fundamentals,” Smart Materials and Structures, **10**, pp. 819-833, 2001.